




Summer 8-14-2009

Capillary Force in High Aspect-Ratio Micropillar Arrays

Dinesh Chandra

University of Pennsylvania, chandrad@seas.upenn.edu

Follow this and additional works at: <http://repository.upenn.edu/edissertations>

 Part of the [Condensed Matter Physics Commons](#), and the [Polymer and Organic Materials Commons](#)

Recommended Citation

Chandra, Dinesh, "Capillary Force in High Aspect-Ratio Micropillar Arrays" (2009). *Publicly Accessible Penn Dissertations*. 430.
<http://repository.upenn.edu/edissertations/430>

This paper is posted at ScholarlyCommons. <http://repository.upenn.edu/edissertations/430>
For more information, please contact libraryrepository@pobox.upenn.edu.

Capillary Force in High Aspect-Ratio Micropillar Arrays

Abstract

High aspect-ratio (HAR) micropillar arrays are important for many applications including, mechanical sensors and actuators, tunable wetting surfaces and substrates for living cell studies. However, due to their mechanical compliance and large surface area, the micropillars are susceptible to deformation due to surface forces, such as adhesive force and capillary force. In this thesis we have explored the capillary force driven mechanical instability of HAR micropillar arrays. We have shown that when a liquid is evaporated off the micropillar arrays, the pillars bend and cluster together due to a much smaller capillary meniscus interaction force while still surrounded by a continuous liquid body, rather than due to often reported Laplace pressure difference because of isolated capillary bridges. We have studied both theoretically and experimentally, the capillary force induced clustering behavior of micropillar arrays as a function of their elastic modulus. To this end, we have developed a modified replica molding process to fabricate a wide range of hydrogel micropillar arrays, whose elastic modulus in the wet state could be tuned by simply varying the hydrogel monomer composition. By minimizing the sum of capillary meniscus interaction energy and bending energy of the pillars in a cluster, we have derived a critical micropillar cluster size, which is inversely proportional to elastic modulus of micropillars. The estimated cluster size as a function of elastic modulus agrees well with our experimental observation. We have also explored the utility of the clustered micropillar arrays as ultrathin whitening layers mimicking the structural whitening mechanism found in some insects in nature. Finally, we have theoretically studied the capillary force induced imbibition of a liquid droplet on a model rough surface consisting of micropillar arrays. Our theoretical model suggests that due to shrinking liquid droplet, the imbibition dynamics does not follow the diffusive Washburn dynamics but progressively becomes slower with time.

Degree Type

Dissertation

Degree Name

Doctor of Philosophy (PhD)

Graduate Group

Materials Science & Engineering

First Advisor

Shu Yang

Keywords

Capillary phenomena, Micropillar, Wetting, Surface and Interface

Subject Categories

Condensed Matter Physics | Polymer and Organic Materials

CAPILLARY FORCE IN HIGH ASPECT-RATIO MICROPILLAR ARRAYS

Dinesh Chandra

A DISSERTATION

in

Materials Science and Engineering

Presented to the Faculties of the University of Pennsylvania

in

Partial Fulfillment of the Requirements for the

Degree of Doctor of Philosophy

2009



Professor Shu Yang

Supervisor of Dissertation



Professor Ju Li

Graduate Group Chairperson

Dissertation Committee

Professor Robert W. Carpick

Professor Russell J. Composto

Professor Daeyeon Lee

Acknowledgements

In my past five years as a graduate student, I have been fortunate enough to be associated with several persons without whose valuable help and input this thesis would not have been possible. It is my great pleasure to humbly express my gratitude towards them in my acknowledgement.

Foremost, I express my sincere thanks towards my advisor, Prof. Shu Yang for her valuable guidance, advice and encouragement throughout the course of my research. I have benefited immensely from Prof. Yang's mentorship. Through her I was introduced to scientific research and she has helped me grow as a scientist. For that, I am forever indebted to her.

I gratefully thank Prof. Russell J. Composto, Prof. Robert W. Carpick and Prof. Daeyeon Lee, for taking time to serve on my thesis committee and for their valuable suggestions and comments. Their insightful comments have helped to make this thesis better and their appreciation has encouraged me in course of my research.

I would like to thank Prof. John A. Taylor for kindly providing the silicon micropillar arrays used in my research. I am thankful to Dr. Andre A. Soshinsky and Dr. Robert J. Gambogi for their discussion and help with the optical characterization of the clustered micropillar arrays.

My thanks to the past and present members of Prof. Yang's group – Dr. Pei-Chun Lin, Dr. Tongxin Wang, Yu-Tun Shen, Dr. Jamie Ford, Dr. Ying Zhang, Marla D. McConell, Dr. Krishnacharya Khare, Dr. G. K. Raghuraman, Yongan Xu and Xuelian Zhu – for their discussions and help in the lab on countless occasions.

I would like to thank Dr. Eva M. Campo and Dr. Lolita Rotkina for training me on various instruments at Penn Regional Nanotechnology Facility. My thanks to Irene Clements, Patricia Overend, Raymond Hsiao, Fred Hellmig and Vicky Lee Truei for their eager help on many occasions and for making life at LRSM smooth and pleasant.

I would like to express my heartfelt gratitude towards my wife, Poonam for her endless love and support. I profoundly appreciate her patience during my long graduate years and her encouragement in my lowest moments.

Finally, I am deeply grateful to my family and my parents for their unwavering love and for providing me the best educational opportunities. I thank my father, to whom I dedicate this thesis, for developing my curiosity towards science early on and for encouraging me to pursue a career in science. I also dedicate this thesis to the sweet memories of my late grandaunt, Mrs. Somwari Devi.

ABSTRACT

CAPILLARY FORCE IN HIGH ASPECT-RATIO MICROPILLAR ARRAYS

Dinesh Chandra

Shu Yang

High aspect-ratio (HAR) micropillar arrays are important for many applications including, mechanical sensors and actuators, tunable wetting surfaces and substrates for living cell studies. However, due to their mechanical compliance and large surface area, the micropillars are susceptible to deformation due to surface forces, such as adhesive force and capillary force. In this thesis we have explored the capillary force driven mechanical instability of HAR micropillar arrays. We have shown that when a liquid is evaporated off the micropillar arrays, the pillars bend and cluster together due to a much smaller capillary meniscus interaction force while still surrounded by a continuous liquid body, rather than due to often reported Laplace pressure difference because of isolated capillary bridges. We have studied both theoretically and experimentally, the capillary force induced clustering behavior of micropillar arrays as a function of their elastic modulus. To this end, we have developed a modified replica molding process to fabricate a wide range of hydrogel micropillar arrays, whose elastic modulus in the wet state could be tuned by simply varying the hydrogel monomer composition. By minimizing the sum of capillary meniscus interaction energy and bending energy of the pillars in a cluster, we have derived a critical micropillar cluster size, which is inversely proportional to elastic modulus of micropillars. The estimated cluster size as a function of elastic modulus

agrees well with our experimental observation. We have also explored the utility of the clustered micropillar arrays as ultrathin whitening layers mimicking the structural whitening mechanism found in some insects in nature. Finally, we have theoretically studied the capillary force induced imbibition of a liquid droplet on a model rough surface consisting of micropillar arrays. Our theoretical model suggests that due to shrinking liquid droplet, the imbibition dynamics does not follow the diffusive Washburn dynamics but progressively becomes slower with time.

Table of Contents

Acknowledgements.....	ii
Abstract.....	iv
List of Tables.....	x
List of Figures.....	xi
Chapter 1. Introduction to High Aspect-Ratio Micropillar Arrays.....	1
1.1 Introduction.....	1
1.2 Applications of HAR micropillar arrays.....	2
1.2.1 Force sensors and actuators	2
1.2.2 Liquid repelling surfaces and their dynamic tuning	3
1.2.3 Biomimetic dry adhesives.....	6
1.3 Fabrication of tall micropillar arrays	7
1.3.1 Top-down fabrication.....	10
1.3.2 Fabrication by self-assembly	12
1.3.3 Replica molding.....	13
1.4 Stability of HAR micropillar arrays.....	15
1.4.1 Collapse due to gravity	15
1.4.2 Collapse due to adhesive forces.....	15
1.4.3 Collapse due to liquid capillary force	17
1.5 Thesis outline and scope of the present work	19
1.6 References.....	22
Chapter 2. Capillary Force	27

2.1 Origin of capillary force.....	27
2.2 Surface tension force.....	28
2.3 Laplace pressure.....	30
2.4 Lateral capillary meniscus interaction force	32
2.5 Capillary driven liquid imbibition in rough surface	34
2.6 References.....	36
Chapter 3. Experimental Methods	37
3.1 Materials	37
3.1.1 Micropillar arrays.....	37
3.1.2 Molds	38
3.1.3 Wetting liquids.....	38
3.2 Fabrication	39
3.3 Characterization	41
3.3.1 Structural characterization	41
3.3.2 Mechanical characterization	41
3.3.3 Surface energy and wetting characterization	44
3.3.4 Optical characterization	46
3.4 References.....	46
Chapter 4. Replica Molding of High Aspect-Ratio Hydrogel Micropillar Arrays ...	48
4.1 Introduction.....	48
4.2 Experimental methods	50
4.2.1 Materials	50
4.2.2 Replica molding of hydrogel pillars	51

4.2.3 Characterization	52
4.3 Results and discussion	53
4.3.1 Fabrication	53
4.3.2 Stability of micropillar arrays in dry state	56
4.3.3 Stability of micropillar arrays in wet state	57
4.4 Conclusions	63
4.5 References	64
Chapter 5. Nature of Capillary Force in 2D Arrays of Micropillars: Isolated Capillary Bridges or Lateral Capillary Meniscus Interaction Force?	67
5.1 Introduction	67
5.2 Experimental methods	69
5.3 Results and discussion	70
5.4 Conclusions	77
5.5 References	78
5.6 Appendix	80
Chapter 6. Capillary Force Induced Clustering Behavior of HAR Micropillar Arrays	83
6.1 Introduction	83
6.2 Experimental methods	85
6.2.1 Materials	85
6.2.2 Fabrication of micropillar arrays	85
6.2.3 Average cluster size determination	86
6.2.4 Water contact angle measurement	86

6.2.5 Elastic modulus measurement.....	86
6.2.6 Whiteness characterization	89
6.3 Results and discussion	89
6.3.1 Micropillar clustering by capillary force	89
6.3.2 Calculation of cluster size.....	93
6.3.3 Critical elastic modulus for stability	99
6.3.4 Whiteness of clustered micropillars.....	100
6.4 Conclusions.....	102
6.5 References.....	102
Chapter 7. Dynamics of Droplet Imbibition on a Rough Surface	105
7.1 Introduction.....	105
7.2 Model description	107
7.3 Results and discussion	109
7.4 Conclusions.....	114
7.5 References.....	114
Chapter 8. Summary and Future Outlook	115
8.1 Summary	115
8.2 Future work.....	118
8.3 References.....	121
Appendix A.....	122
Appendix B.....	133

List of Tables

Table 1.1 Fabrication methods for HAR micropillar arrays.....	9
Table 4.1 Surface energy, Young's modulus and critical modulus of ground and lateral collapse for different hydrogel pillar arrays.....	57

List of Figures

Figure 1.1 Illustration of high aspect-ratio micropillar array.....	2
Figure 1.2 Schematic of fabrication processes for micropillar arrays.....	8
Figure 1.3 Capillary bridge between two parallel plates.....	19
Figure 2.1 A liquid droplet on a solid surface.....	28
Figure 2.2 (a) A liquid film spanning a wire loop, (b) surface tension force on a cylinder.....	29
Figure 2.3 Laplace pressure force due to capillary bridge between two parallel plates...	31
Figure 2.4 Lateral capillary between two cylinders partially immersed in a liquid.....	33
Figure 2.5 Liquid imbibition on a rough surface.....	35
Figure 3.1 Monomers used for fabrication of micropillar arrays.....	38
Figure 3.2 Schematic illustration of AFM nanoindentation and a typical tip deflection vs. piezo displacement curve.....	43
Figure 4.1 Schematic illustration of the fabrication process of hydrogel micropillar arrays.....	52
Figure 4.2 Typical viscosity values vs. UV ($\sim 8 \text{ mW/cm}^2$) exposure time for 2.5 mL HEMA mixed with 0.5 g NIPA and 3 wt% photoinitiator.....	54
Figure 4.3 SEM images of different hydrogel pillar arrays. (a-c) PHEMA, (d-f) PHEMA- <i>co</i> -PNIPA, and (g-i) PEGDMA. (a, d, g) Square pillars: 9 μm tall, 1 μm wide, and adjacent pillar spacing of 1 μm . (b, e, h) Circular pillars: 9 μm tall, 750 nm in diameter, and adjacent pillar spacing of 750 nm. (c, f, i) Conical pillars: 7 μm tall, tip diameter of	

350 nm, base diameter of 750 nm, and adjacent pillar spacing of 1.25 μm at base. Scale bar in (a) applies to all the images.....	55
Figure 4.4 Stability and wettability of PHEMA- <i>co</i> -PNIPA conical pillar array when exposed to water. (a-b) Optical images of water droplet on PHEMA- <i>co</i> -PNIPA conical pillar array. (a) Initial film with water contact angle of 140°. (b) Film after soaking in water for 15 minutes and blown-dry, water contact angle of 83°. (c) SEM image of the ground collapsed hydrogel pillar arrays after air dried corresponding to (b).....	58
Figure 4.5 Stability and wettability of PEGDMA conical pillar array when exposed to water. (a) Optical image of water droplet on PEGDMA conical pillar array before and after soaking in water for 30 minutes and blow-dried, water contact angle of 159°. (b) Optical microscope image of the PEGDMA conical pillar array corresponding to (a) after soaking in water and blow-dried.....	59
Figure 4.6 Comparison of measured water contact angles on the hydrogel pillar arrays vs. those predicted by Cassie and Wenzel models.....	60
Figure 4.7 Images of different PEGDMA micropillar arrays after soaking in ethanol for 15 minutes followed by blow-drying. (a) Optical microscope image of conical pillar array ($d_{tip} = 350\text{ nm}$, $d_{base} = 750\text{ nm}$, $h = 7\text{ }\mu\text{m}$, and $w_{base} = 1.25\text{ }\mu\text{m}$) and (b) SEM image of circular pillar array ($d = 750\text{ nm}$, $h = 9\text{ }\mu\text{m}$, $w = 750\text{ nm}$).....	62
Figure 5.1 SEM images of epoxy micropillar arrays. (a) As fabricated and (b) collapsed by polystyrene melt.....	70
Figure 5.2 AFM scan of polystyrene wetting morphology in epoxy micropillar arrays. The mean curvature at two representative points, A and B is the same.....	71

Figure 5.3 Schematic illustrations of two micropillars (a) partially immersed in a liquid and (b) with an isolated capillary bridge between them.....	73
Figure 5.4 (a) A typical plot of capillary interaction force, F_C , (solid line) and elastic restoring force acting on the deflected pillar, F_E , (dashed lines). δ_1 and δ_2 represent stable equilibrium and unstable equilibrium, respectively. Inset: schematic illustration of interaction between a group of four pillars. Increasing slope of F_E corresponds to increasing elastic modulus E . (b) Function $f(r)$ as a function of $r = p/d$. The dashed line indicates the value of the function at $r = 2$	76
Figure 6.1 (a) An indentation force curve for 60 wt% MMA sample and (b) the corresponding $(z-d)$ vs. $(d-d_0)^{1/2}$ plot.....	88
Figure 6.2 SEM images of 9 μm tall PHEMA- <i>co</i> -PMMA micropillar arrays clustered by water capillary force.....	90
Figure 6.3 Elastic modulus in wet state (a) and the water contact angle (b) of flat PHEMA- <i>co</i> -PMMA films as a function of MMA content.....	91
Figure 6.4 (a) Schematic illustration of micropillar clustering process due to capillary meniscus interaction force. (b) Schematic illustration of micropillar array clustering in a square lattice. (c) SEM image of micropillars clustered in a square lattice.....	93
Figure 6.5 Numerical solution to equation 6.10 and linear fit to the solution points.....	97
Figure 6.6 Micropillar cluster size as a function of the elastic modulus of micropillars in wet state for (a) geometry A and (b) geometry B. Dashed lines are linear fit ($r^2 = 0.99$ and 0.98 in (a) and (b) respectively) to experimental data.....	98

Figure 6.7 Whiteness caused by random clustering of micropillar arrays and the corresponding CIE lightness index. (a) SEM (left) and optical images (right) of micropillar arrays before and after clustering. Two different colors in (a) (top right) result from Bragg diffraction of micropillar arrays with different periodicity. (b) CIE lightness index of clustered micropillar arrays as a function of MMA content.....	101
Figure 7.1 A droplet sitting in Wenzel state (a) and imbibing into the grooves in hemi-wicking state (b).....	106
Figure 7.2 Schematic showing parameters for a droplet imbibing in a rough surface...	109
Figure 7.3 Calculated dynamics of droplet imbibition (Eq. 7.10) and 1-D imbibition from a reservoir (Eq. 7.11).....	111
Figure 7.4 Slope of a typical $\ln(l)$ vs. $\ln(t)$ plot of a droplet imbibing in a rough surface as a function of time.....	112
Figure 7.5 Slope of a typical $\ln(l)$ vs. $\ln(t)$ plot of a non-shrinking droplet imbibing in a rough surface as a function of time.....	113
Figure A.1 Schematic illustration of the fabrication procedure of concave microlens array (a-f). (f) Inset: SEM image of a concave microlens array.....	124
Figure A.2 AFM images of (a) concave and (c) convex microlens array. Optical images of (b) concave and (d) convex microlens arrays, corresponding to those from (a) and (c). Insets: the optical images of letter ‘N’ imaged through the respective microlens arrays. (e) Optical setup for measuring the microlens focal length.....	126
Figure A.3 Focal length variation and corresponding stretching mechanism of the concave (a,c) and convex (b,d) microlens array, respectively.....	129

Chapter 1

Introduction to High Aspect-Ratio Micropillar Arrays

1.1 Introduction

Arrays of high-aspect-ratio (HAR) microstructures (Fig. 1.1, aspect-ratio - ratio of height to lateral feature size) present many unique features, including large surface area, spatially distinct surface topography that is well separated from the underlying substrate, and large mechanical compliance. In Nature, these advantages have resulted in interesting evolutionary functions ranging from formidable, reversible, dry adhesion of a gecko foot due to hierarchical arrays of nano- and micropillars¹, to the superhydrophobic nature of lotus leaves because of array of microscopic protrusions on their surface². Taking cues from Nature, many researchers have created arrays of HAR microstructures and investigated their potential applications in many technologically important systems, such as reversible dry adhesives³⁻⁷, superhydrophobic⁸ and superoleophobic⁹ surface, and tunable wetting,^{10,11} as well as micromechanical sensors¹²⁻¹⁵ and actuators¹⁶⁻²⁰. However, because of their small dimensions and large aspect ratio, these structures possess high surface area to volume ratio. Therefore, they are susceptible to surface forces, such as adhesive force between the microstructures and liquid capillary forces when immersed and dried from the liquid²¹⁻²³, leading to pattern collapse. Recently, these forces, for example, capillary force, have been utilized to self-assemble hierarchical superstructures²⁴. Systematic understanding of the effect of capillary forces on the stability of HAR micropillar arrays is critical to both the fabrication of high fidelity HAR

microarrays and their manipulation for a wide range of applications. First, we illustrate a few exemplary applications of HAR pillar arrays.

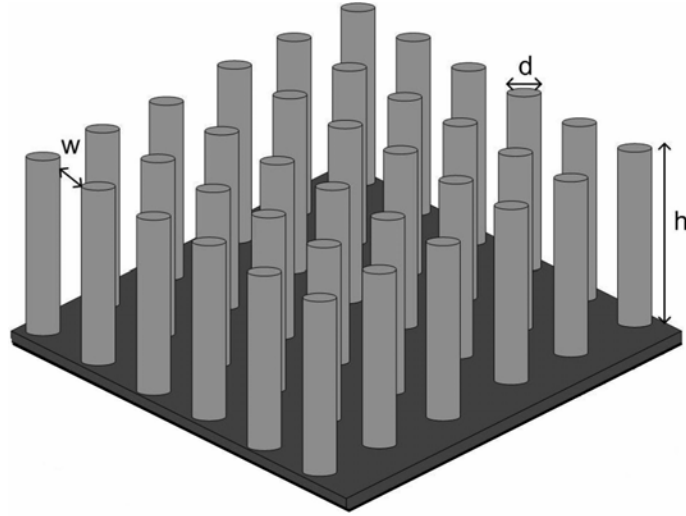


Figure 1.1 Illustration of high aspect-ratio micropillar array.

1.2 Applications of HAR micropillar arrays

1.2.1 Force sensors and actuators

One of the important features offered by the tall micropillar arrays is their small bending stiffness. This has led to applications such as force sensors and actuators at the micro-scale. As force sensors, they have been widely used to study the mechanical response of living biological cells¹²⁻¹⁴. A living cell lying on top of micropillar arrays exerts traction forces, which can be measured by measuring the deflection of the tips of the underlying micropillars. The sensitivity and spatial resolution of the force measurement depends on the geometry of the micropillar arrays¹⁵. Large aspect ratio will result in smaller bending stiffness and thus larger tip deflection and greater sensitivity whereas smaller inter-pillar separation results in better spatial resolution. For example, du

Roure¹³ et al. studied the traction force generated by epithelial cells lying on high density array of elastomeric [poly(dimethylsiloxane), PDMS] micropillars by observing the deflection of the micropillars. By this method they could achieve a spatial resolution of cell mechanics down to 2 microns. Using a similar approach, Tan¹⁴ et al. studied the effect of cell morphology on the traction forces generated by the cells on PDMS micropillar arrays. In addition to their application as force sensors, micropillar arrays have been used as actuators in response to an external force. Evans¹⁶ et al. demonstrated the actuation of PDMS-ferrofluid composite micropillar arrays by applying external magnetic field. Sniadecki¹⁸ et al. studied cell response to external forces by putting the cells on PDMS-cobalt nanowire composite micropillar arrays and actuating the pillars by applying magnetic field. In turn, force generated by living cells can be used to actuate micropillars, and thus realizing biomicroactuators^{17,20}. For example, Tanaka²⁰ and co-workers successfully generated forces over 1 μN by chemically stimulated muscle cells attached to micropillars. By coating hydrogels on HAR silicon nanopillar arrays, Sidorenko et al. demonstrated reversible actuation of Si pillars through swelling and drying of the hydrogel coating²⁵. While many nano- and micropillars have isotropic cross-sections (e.g. spherical and square), micropillar arrays with elliptical cross-section have been created.²⁶ The latter shows anisotropic rigidity (more rigid in the direction of major axis of the ellipses), resulting in anisotropic cell migration on such substrates.

1.2.2 Liquid repelling surfaces and their dynamic tuning

Because of their well-defined surface topography, which is well-separated from the underlying substrate, and large actual surface area, HAR structures are of great interest in systematic study of surface roughness effect on superhydrophobic⁸ and tunable

wetting^{10,11}. In Nature, lotus leaf is a well known example of superhydrophobic, self-cleaning surface, which consists of micro- and nano-protrusions on the leaf surface, thus water droplets can easily roll off the surface.²

There have been two simple wetting models to explain the surface roughness effect on wettability, that is Wenzel model where a liquid droplet penetrates and wets in-between the grooves of the roughness²⁷, and Cassie-Baxter model where the droplet sits on the tips of the roughness²⁸. In the Wenzel state the liquid contact angle θ_w on the rough surface is given by

$$\cos \theta_w = r \cos \theta_0 \quad (1.1)$$

where r is the ratio of actual surface area of the rough surface to the projected surface area, and θ_0 is the liquid contact angle on a flat surface of identical chemical nature, so called Young's contact angle given by the Young's equation,

$$\cos \theta_0 = (\gamma_{sv} - \gamma_{sl}) / \gamma_{lv} \quad (1.2)$$

where, γ_{lv} is the liquid surface tension and γ_{sv} and γ_{sl} are solid-vapor and solid-liquid surface energies, respectively. In Cassie-Baxter state, the liquid contact angle on rough surface, θ_c , is given by

$$\cos \theta_c = \phi(\cos \theta_0 + 1) - 1 \quad (1.3)$$

where ϕ is the solid fraction at the top of the roughness. Thus, in the Cassie-Baxter model, roughness always increases the contact angle, that is, the surface becomes more liquid repellant, whereas in Wenzel model, depending on the Young's contact angle, roughness can decrease the apparent contact angle on a hydrophilic surface ($\theta_0 < 90^\circ$) or increase it on a hydrophobic surface ($\theta_0 > 90^\circ$). In non-wettable state, the liquid droplet

is pinned to the substrate in Wenzel model as it penetrates the grooves of the roughness, whereas in Cassie-Baxter model, the droplet is mobile and can easily roll off the surface since it sits only on tips of the roughness⁸. Thus for applications such as self-cleaning and non-wettable surfaces, Cassie hydrophobic state is more desirable. For the Cassie state to be thermodynamically favored, θ_0 should be greater than a critical angle θ_C given by²⁹

$$\cos \theta_C = -(1 - \phi)/(r - \phi) \quad (1.4)$$

When $\theta_0 < \theta_C$, Wenzel state is favored. The preceding criterion for a stable Cassie state is easily satisfied for large r , i.e. very rough surfaces, even for slightly hydrophobic θ_0 . High aspect ratio micropillar arrays provide such rough surfaces. However, droplets can also be in a metastable Cassie state even when Wenzel state is favored by the above criterion^{29,30}. The metastable state can remain as long as the droplet does not initiate a contact with the underlying bottom surface, which can be induced by an external force or the Laplace pressure of the drop²⁹. On HAR structures, the metastable Cassie state is readily achieved as it is more difficult to initiate the droplet contact with the bottom. Guided by the above mentioned principles, there has been extensive research in designing superhydrophobic surface and their dynamical tuning of their wetting behaviors. For example, Krupenkin et al. have fabricated silicon nanopillar arrays and achieved dynamic switching from superhydrophobic Cassie state to completely wetting Wenzel state by means of electrowetting¹¹. Stable superoleophobic surfaces have been demonstrated by Tuteja et al. in arrays of ‘micro-hoodoos’ with reentrant curvature geometry⁹. Stable omniphobic (repelling both water and oil) surfaces with tunable wetting¹⁰ have also been designed by utilizing arrays of micropillar arrays. Further, it has been shown that

micropillar arrays also affect the dynamics of wetting and a liquid droplet on micropillar arrays spreads faster than that on a chemically identical flat surface³¹.

1.2.3 Biomimetic dry adhesives

Inspired by strong, reversible and dry adhesion of gecko foot hairs, there has been extensive interest in fabrication of arrays of tall microstructures to mimic the biological design. Each gecko foot¹ is covered with an array of half a million keratin hair called setae, which are about 130 μm long and 15 μm in diameter. At the tip, each setae branches into hundreds of long filaments called spatulae. Each of the spatulae generates a tiny van der Waals force of about 10^{-7} N, resulting in a formidable adhesion force, 10 N/cm² in each gecko foot, where the high aspect-ratio nature of the setae and spatulae plays a critical role. Because of their small bending stiffness, the setae can conformally contact the microscopic roughness of any surface, enabling almost all the spatulae to make physical contact with the surface, resulting in a large cumulative adhesive force. At the same time, by positioning the mechanically compliant setae at a critical angle with the surface facilitates easy detachment of the gecko toe¹. Thus, to design gecko inspired, synthetic, reversible dry adhesive, it is critical to create the stable tall structures with optimum aspect ratio and Young's modulus^{3,4}. Greiner⁴ et al. fabricated periodic array of PDMS micropillars and demonstrated increasing adhesion with increase in the pillar aspect-ratio. Based on the same principles, Qu⁷ et al. designed dry adhesive tape consisting of carbon nanotube arrays, which produced large adhesion in the shear direction and small adhesion in the normal lift-off direction similar to the behaviors observed in gecko foot. Hierarchical design of nanopillar arrays has also been reported to achieve gecko-inspired reversible dry adhesion⁶. Further, Mahdavi⁵ et al. designed a

biocompatible and biodegradable tissue adhesive from micropillars of poly(glycerol-co-sebacate acrylate) elastomer, demonstrating the microstructure could improve the *wet* adhesion.

Besides the above mentioned applications, micropillar arrays have also been used in bio-microfluidics³², designing efficient batteries³³ and enhanced heat transfer³⁴.

1.3 Fabrication of tall micropillar arrays

Because of their technological importance, there has been much research in developing fabrication methods to realize arrays of HAR microstructures. HAR micropillar arrays have been fabricated in both inorganic materials such as silicon^{11,35,36}, quartz³² and metals³⁷, and in polymers such as, PDMS^{13,14,38}, epoxy³⁹, photoresists⁴⁰ and polyimide³. The fabrication strategies can be broadly divided into three categories – top-down, self-assembly and molding. Top-down fabrication involves selective removal of materials after defining the desired pattern either by photolithography or by scanning lithography (for example, electron beam writing). On the other hand, self-assembly methods take advantage of thermodynamic driving force to spontaneously pattern materials (e.g. block copolymers, colloidal particles) in a periodic order. Molding involves replicating an existing topographic pattern, in a suitable material by means of a mold.

Fabrication of HAR micropillar arrays presents some unique challenges because of their tall structures. First of all, to achieve vertical side-walls it requires highly anisotropic material etching to large depths in the top-down process. In molding methods, the molding materials have to infiltrate the deep channels of the mold completely.

Further, as mentioned before, HAR micropillar arrays are susceptible to deformation due to adhesive and capillary forces. In many fabrication methods (e.g. photolithography) and applications (e.g. wetting, cell mechanics) tall micropillars are exposed to liquid environment where they can deform due to capillary forces. Thus, a high mechanical strength is often required to ensure high fidelity of HAR structures during both fabrication and post-fabrication applications. Here we compare recent advances in fabrication techniques (Fig. 1.2), which are summarized in Table 1.1.

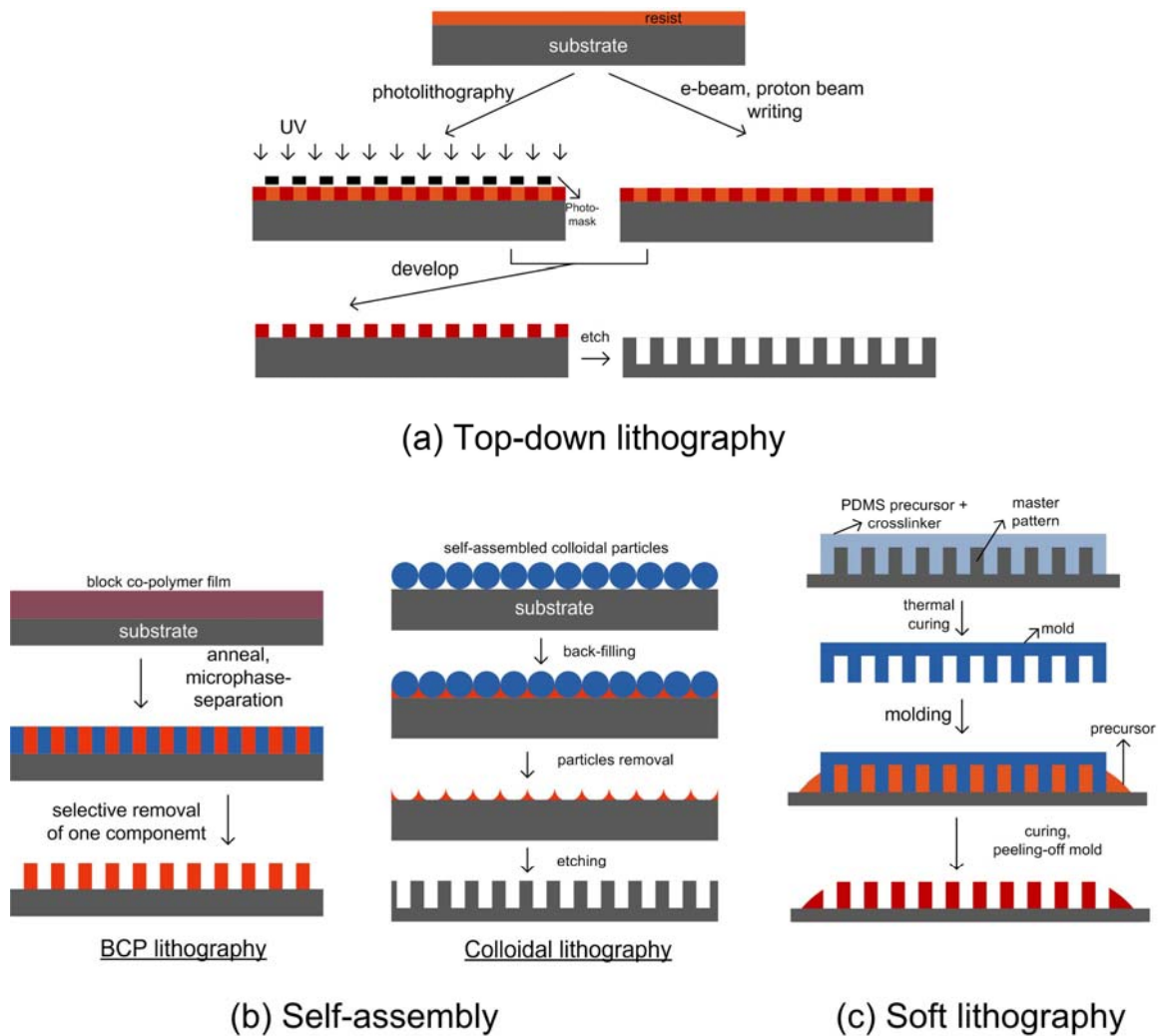


Figure 1.2 Schematic of fabrication processes for micropillar arrays.

Table 1.1 Fabrication methods for HAR micropillar arrays.

Method	Minimum feature-size	Aspect-ratio	Materials directly patternable	Process	Ref.
Photolithography	~50 nm dependent on optical tool	~50	photoresists	parallel, large-area, multi-step, defect-free	40, 42
Scanning beam lithography (e- beam, proton- beam)	<10 nm	~5 (e- beam) ~150 (proton beam)	PMMA (most widely used) SU-8	serial, small- area, multi- step, defect- free	42
Block co- polymer lithography	<10 nm determined by chain length	~10	block co- polymers	parallel, large-area, multi-step, random defects exists	42, 44
Colloidal lithography	~40 nm limited by particle size	dependent on etching method		parallel, large-area, multi-step, random defects exists	35, 45
Anodized alumina template	~10 nm	~10, 000	metals, polymers, carbon	parallel, large-area	42, 46- 48
Soft lithography (e.g. replica molding)	a few nm dependent on master and molecular size of molding material	>20	photoresists, polymers, polymer precursors, bio-molecules	parallel, large-area, both flat and curved substrates	39, 49

1.3.1 Top-down fabrication

HAR micropillar arrays are fabricated by photolithography or scanning lithography (e.g. electron beam writing, proton beam writing) followed by selective etching or removal of material.

Photolithography: The geometry of the micropillars can be defined on a photoresist film through a photomask, followed by anisotropic etching of the underlying substrate (e.g. Si) using the patterned resist as an etch mask (Fig. 1.2a). When selective areas of the photoresist film are exposed to UV light with desired wavelength through a photomask, the exposed areas of the photoresist either become cross-linked and insoluble (negative-tone resist) or become soluble in a suitable solvent (positive-tone resist). After dissolving the selective regions of the resist film, the patterned photoresist film acts as an etch mask for the subsequent etching of the underlying substrate. HAR Si micropillar arrays with vertical profile have been fabricated by highly anisotropic etching of silicon using a high-density inductively coupled plasma etching⁴¹. The aspect ratio can be tuned by the etching time and intensity. Alternatively, HAR structures can be directly fabricated in a thick photoresist film, and the aspect ratio can be varied by spin coating of the resist film at different concentrations and spin speeds. A suitable resist should have high contrast and resolution to obtain straight pillar sidewalls during development. In addition, the resist should have high mechanical strength to prevent structural collapse due to capillary force during the development and drying process. One such photoresist for fabricating HAR microstructures is SU-8, a chemically amplified negative-tone photoresist. The crosslinked SU-8 has a Young's modulus of more than 4 GPa⁴⁰. Fabrication of SU-8 photoresist for HAR microfabrication has been reviewed by del Campo and Greiner⁴⁰.

Aspect-ratio of up to 40 has been achieved⁴² in SU-8 by UV-lithography. In photolithography, the resolution is dependent on the optical tool (e.g. wavelength of the photon source, and numerical aperture of the optical lens) and feature sizes less than 100 nm have been achieved.

Scanning lithography by electron beam or proton beam writing: Higher resolutions can be achieved by exposing a resist material to electron beam (e-beam) or proton beam, which has much lower wavelength than UV-irradiation. In e-beam lithography, a resist material, e.g. poly(methyl methacrylate) (PMMA), is exposed to e-beam in a serial writing fashion. The incident electrons generate secondary electrons which cause chain scission in the resist film, making the exposed areas soluble. Due to scattering of electrons in the resist material the resolution and depth are limited to ~10 nm and ~100 nm respectively⁴². By this method, feature sizes of 50 nm and aspect ratios of up to 5 have been achieved⁴². Similar to photolithography process, the structures patterned in e-beam resist can be transferred to underlying substrates. For example, quartz³² and polyimide³ micropillar arrays have been fabricated by this method. In contrast to e-beam, proton beam offers much heavier mass and thus very little scattering resulting in much higher penetration depth and aspect-ratio. Line width of 60 nm with an aspect-ratio of ~160 has been achieved by this method⁴² in SU-8. Structures defined by proton beam lithography can be transferred to other materials. Ansari³⁷ et al. fabricated HAR nickel stamps by electroplating PMMA patterns defined by proton beam lithography. Since both e-beam and proton beam scanning lithography are serial writing processes, the throughput is low and they are most suitable for small area patterning.

1.3.2 Fabrication by self-assembly

In this approach, thermodynamic driving force is utilized to spontaneously pattern materials (e.g. block copolymers (BCPs) and colloidal particles) in a periodic array and feature sizes as low as a few nanometers can be obtained over a large area.

Block copolymer lithography: Block copolymers consist of two or more chemically different polymer chains connected at the chain-end by covalent bond. Because of their different chemical nature, the BCPs phase separate in nanometer sized periodic domains, where the morphology and domain size are dependent on the composition of the BCP, f , the interaction parameter, χ , between blocks, and the chain length of each block. In BCP-lithography, topographic pattern is obtained by selectively removing one of the phases (Fig. 1.2b). For example, in polystyrene(PS)-*b*-poly(methyl methacrylate)(PMMA), by selective removal of PMMA domains, hexagonally close-packed holes with 18 nm in diameter and an aspect ratio of 2 have been obtained⁴². The resulting nanoporous film can then be used as either template or etch mask to form topographic patterns in metals, semiconductors and dielectrics⁴³. By using BCP film as template, fabrication of silica nanorods with diameter ~ 20 nm and height ~ 200 nm has been reported⁴⁴.

Colloidal lithography: Self-assembly of colloidal particles can also be used to template micropillar arrays. Compared to BCP lithography, the colloidal assembly does not require long annealing step. However, the feature sizes are larger than that obtained by BCP lithography. To obtain micropillar arrays by colloidal lithography, in a typical process, a monolayer of close-packed colloidal particles is deposited on a substrate, followed by back filling with metal and removal of the colloidal particles. The substrate is then etched, where the backfilled metal acts as etch mask, to obtain pillar arrays⁴⁵ (Fig. 1.2b).

Kuo³⁵ et al. fabricated silicon nanopillar arrays of lateral dimension down to 40 nm and aspect ratio up to 7 by this method. They used polystyrene particles of diameter 330 nm and 440 nm for colloidal assembly. In colloidal lithography, the feature size is determined by the void size between the close-packed colloidal particles.

Porous anodic aluminum oxide (AAO): Compared to BCP and colloidal lithography, a much higher aspect-ratio can be achieved by using nanoporous AAO templates to fabricate pillar arrays. Nanoporous AAO membranes are self-ordered arrays of nanopores formed by anodization of aluminum in acidic electrolyte. The pores are straight, parallel and highly uniform. Their diameter can range from ~10 nm to 400 nm and they can be hundreds of micron deep. Because AAO templates are compatible with many backfilling process and can be easily removed by aqueous NaOH or KOH solution, they have been widely used to template dense arrays of very high aspect-ratio nanopillar arrays in polymers⁴⁶, metals⁴⁷ and carbon⁴⁸.

1.3.3 Replica molding

Most of the fabrication approaches described above are applicable to either special class of materials (e.g. photoresists) or require multi-step harsh processing conditions which are not suitable for patterning a vast majority of soft materials like hydrogels and biological materials. Over the past two decades, soft lithographic methods⁴⁹, including micromolding, stamping, imprinting, and replica molding have been developed for processing of soft materials, such as polymers. In a typical replica molding process a soft elastomeric mold (e.g. PDMS) is used to define topographic patterns in a desired material, followed by curing (Fig. 1.2c). The PDMS molds are themselves created by thermal curing of a mixture of PDMS and a crosslinking agent poured over a master

micropillar array (silicon, metal etc.), followed by removal of the solid PDMS mold off the master.

The soft elastomeric nature and low surface energy of the PDMS facilitates easy removal of the mold from both the master and the replicated structures for subsequent use even in case of high aspect-ratio structures. Since the structures are defined physically by a mold, it is not required to have specific chemical functionality in the molding material and a large variety of soft material can be molded as long as they do not damage the mold. Using replica molding method, micropillar arrays have been fabricated in a variety of materials including, PDMS¹⁴, epoxy, and polyurethane³⁹. In principle, the resolution achievable by this method is limited only by the master pattern and molecular size of the molded material⁵⁰ and ~3 nm wide features have been replicated by using highly cross-linked PDMS molds⁵⁰. Stable micropillar arrays with pillar diameter 400 nm and aspect ratio more than 22 have been fabricated using replica molding from PDMS molds³⁹.

Although, PDMS molds have been used to mold a wide range of materials, they are not suitable for direct molding of hydrogel monomers. The monomers easily diffuse into the molds and swell the mold, while the oxygen dissolved in the porous mold diffuses in the molding material and inhibits the free-radical polymerization⁵¹ and crosslinking during UV-curing. In this thesis, we have used a modified two-step replica molding process to pattern HAR hydrogel micropillar arrays (Chapter 4). In the first step, the monomers or monomer mixtures were partially UV-polymerized to obtain a viscous molding precursor. In the second step, this precursor was molded and UV-cured after adding crosslinker and additional photoinitiator. The increased viscosity of the precursor

in the first step effectively prevented both the monomer diffusion in the mold and the oxygen diffusion in the molding precursor resulting in successful fabrication.

1.4 Stability of HAR micropillar arrays

As mentioned before, low bending modulus and large surface area to volume ratio results in many interesting applications of HAR micropillar arrays. At the same time, however, these properties lead to increased susceptibility to deformation due to external forces, including surface forces such as adhesion and capillary forces. Here we discuss some common mechanical instability encountered in HAR microstructures.

1.4.1 Collapse due to gravity

Hui⁵² et al. suggested that soft, HAR microstructures, such as from PDMS, can buckle under their own weight. The critical height, h_c of the microstructures above which they are unstable against the gravity induced buckling is given as,

$$h_c = \left(\frac{0.49Ed^2}{\rho g} \right)^{1/3} \quad (1.5)$$

where, d is the diameter of the micropillar, E and ρ are the elastic modulus and density of the micropillar material respectively and g is the gravitational acceleration.

1.4.2 Collapse due to adhesive forces

As the aspect ratio increases and the dimensions decrease, the surface area to volume ratio of the microstructures decreases and surface adhesive forces become dominant. As pointed out by Roca-Cusachs⁵³ and co-workers, in the gravitational model of ground collapse (Eq. 1.5) the critical aspect ratio for stability scales as $d^{1/3}$, indicating that as the diameter decreases, the pillars would be stable for higher aspect ratio. In

particular, as the pillar diameter tends to zero, the stable aspect ratio tends to infinity which is clearly not true. At smaller dimensions, adhesion between the pillars and between a pillar and the substrate dominate over the gravitational force and become the main cause for ground collapse and lateral collapse of the micropillars. By balancing the bending energy of the ground collapsed micropillar with the energy of pillar adhesion to the substrate, Roca-Cusachs⁵³ and co-workers derived an expression (Eq. 1.6) for the critical aspect ratio, $(h/d)_c$ below which the micropillars are stable.

$$\left(\frac{h}{d}\right)_c = \frac{\pi^{5/3}}{2^{11/3}3^{1/2}}(1-\nu^2)^{-1/6}\left(\frac{E}{2\gamma_{sv}}\right)^{2/3}d^{2/3} \quad (1.6)$$

Here, ν is the Poisson's ratio for the pillar material and γ_{sv} is the surface energy of the pillar material. In addition to ground collapse, the micropillars can also bend laterally and adhere to the neighboring pillars. This lateral collapse is more dominant in high density micropillar arrays where, due to small interpillar distances, only a small amount of bending is required for the pillars to adhere together. By balancing the bending energy and the energy of deformation (to make adhesion over a finite area) of laterally adhered pillars with their energy of adhesion, Glassmaker³⁸ and co-workers derived an expression (Eq. 1.7) for the critical aspect ratio, $(h/d)_c$ below which the micropillars are stable against lateral collapse.

$$\left(\frac{h}{d}\right)_c = \left(\frac{3^{3/4}\pi E w^{3/2}}{2^{1/4} \cdot 32\gamma_{sv}(1-\nu^2)^{1/4}d^{1/2}}\right)^{1/3} \quad (1.7)$$

where w is the lateral separation between adjacent micropillars (Fig. 1.1).

1.4.3 Collapse due to liquid capillary force

Many applications of micropillar arrays, such as cell mechanics studies and microfluidics require them to be used in liquid environment. In addition, in photolithography based fabrication process, the micropillar arrays are exposed to solvent during development process, followed by drying, which causes the tall structures to collapse due to capillary forces associated with the liquid. In general, capillary force is proportional to the liquid surface tension, γ and arises because of the tendency of a system to minimize the sum of its three interfacial energies – liquid-vapor (γ_{lv}), solid-vapor (γ_{sv}) and solid-liquid (γ_{sl}). The phenomenon of capillary force is responsible for a wide range of macroscopic and microscopic observations, ranging from the rise of liquid in a capillary tube and clumping of hair after shower to self-assembly of microparticles⁵⁴. In context of HAR microstructures, it is responsible for mechanical failure of tall line patterns during liquid evaporation off their surface^{23,55} and clustering together of micropillar arrays when a liquid is evaporated off their surface^{22,56}. Capillary force has also been utilized to self-assemble HAR micropillars into ordered hierarchical structures^{22,24}. The capillary force induced collapsing of one dimensional (1D) arrays of tall microstructures has been explained by Laplace pressure difference due to curved interface of isolated capillary bridges formed between the microstructures²³. For example in the configuration shown in Fig. 1.3, because of the curvature of the liquid between the two plates separated by distance d , the pressure inside the liquid is lower than that outside. Due to this pressure difference, the plates experience net force and bend towards each other. The pressure difference $\Delta P = P_l - P_g$ is given as²³,

$$\Delta P = \left(\frac{2\gamma \cos \theta}{d} \right) \quad (1.8)$$

where γ is the liquid surface tension and θ is the contact angle of the liquid on the plate material. By balancing the Laplace pressure force with the elastic restoring force of the bent plates, Tanaka and co-workers have derived stability criteria of tall line patterns against capillary force.

The argument of Laplace pressure difference due to isolated capillary bridges is often extended to 2D arrays of micropillars to explain their clustering^{40,56-58}. However, as we show in detail in the later chapters, the collapsing of the latter is due to capillary meniscus interaction force⁵⁹ while the pillars are still surrounded by a continuous liquid body (i.e. no isolated capillary bridges). This approach has rarely⁶⁰ been used to describe the capillary clustering of micropillar arrays and in the few studies reported, sometimes no distinction is made between the two approaches²¹ or no justification is provided for using the capillary meniscus interaction approach⁶⁰. The capillary meniscus interaction force originates due to interaction between the liquid menisci surrounding the individual micropillars⁵⁹ and its magnitude is much lower than the force due to Laplace pressure difference due to isolated capillary bridges between the pillars. Here, we emphasize though that as mentioned above and as discussed in detail in Chapter 2, the origin of all kinds of capillary forces is due to the minimization of the total interfacial energy of the system and the different kinds of capillary forces originate due to different geometries of the systems.

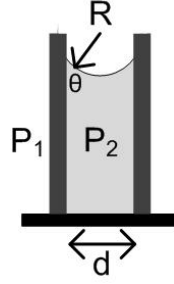


Figure 1.3 Capillary bridge between two parallel plates.

1.5 Thesis outline and scope of the present work

This thesis focuses on the study of the nature of the liquid capillary forces in high aspect-ratio micropillar arrays and their capillary force induced clustering behavior as a function of their elastic modulus.

As we discussed earlier, 2D arrays of HAR micropillar arrays are both important for various applications and also susceptible to deformation due to various surface forces including liquid capillary force which can also be potentially harnessed for self-assembly of these tall microstructures. However, the collapsing behavior of 2D arrays of tall micropillar arrays due to liquid capillary force is not well studied and often Laplace pressure argument due to isolated capillary bridges is simply extended to explain the observed collapsing of 2D micropillar arrays in literature. Further, to experimentally study the effect of mechanical properties of the micropillar material on their clustering behavior, it is desirable to prepare micropillars whose mechanical properties can be tuned continuously over a wide range.

To address the above issues, the thesis is outlined as the following: in Chapter 2, we present theoretical background on the origin of different types of capillary force. In

Chapter 3 we describe the fabrication and characterization techniques used in the present work. The results of our research are discussed in Chapters 4 through 7 as outlined below. Chapter 8 summarizes the thesis work and provides insights for future research and outlook related to our current work.

In Chapter 4 we present a novel method to fabricate HAR hydrogel micropillar arrays by replica molding. Hydrogels are an important class of materials whose chemical and physical properties can be easily tailored and many of them are sensitive to external stimuli. In particular, by simply varying the composition of the monomers as the molding material, mechanical properties of the resulting micropillars can be tuned. However, direct molding of hydrogel monomers by using a PDMS mold followed by UV initiated free-radical polymerization is not possible as the monomers diffuse into the mold and the oxygen dissolved in the mold inhibits free radical polymerization. In our approach, we fabricate tall micropillars by first partially polymerizing the hydrogel monomers or monomer mixture and molding the partially polymerized viscous precursor followed by UV-initiated further polymerization and cross-linking. The increased viscosity in the partial polymerization step prevents both the monomer diffusion in the PDMS mold and oxygen diffusion from the mold, resulting in successful fabrication of HAR micropillar arrays. We demonstrate successful fabrication in three different geometries and three different hydrogel systems. By our modified replica molding process we have extended the soft lithography method to the fabrication of tall hydrogel microstructures. We also study the stability of the fabricated pillar arrays against adhesive and capillary forces.

In Chapter 5, we investigate the nature of capillary force acting on 2D micropillar arrays during liquid evaporation off their surface. Our experiments, using low molecular

weight polystyrene as the wetting liquid on epoxy micropillar arrays, show that the micropillars collapse during liquid evaporation while they all are still surrounded by a continuous liquid body and that there are no isolated capillary bridges present. Thus, we experimentally show for the first time that the capillary force induced clustering of 2D micropillar arrays should be attributed to lateral forces resulting from the interaction between capillary menisci around individual pillars rather than to often reported Laplace pressure difference due to isolated capillary bridges. We present theoretical evidence to show that in a typical case, Laplace pressure force can be more than an order of magnitude larger than that estimated by capillary meniscus interaction force. This difference is reflected in large difference in the elastic modulus for stability calculated from the two approaches.

In Chapter 6, we study the capillary force induced clustering of poly(2-hydroxyethylmethacrylate-*co*-methyl methacrylate) (PHEMA-*co*-PMMA) micropillar arrays fabricated by the process described in Chapter 4. By varying the composition of water swellable PHEMA versus the glassy, non-swellable PMMA in the micropillar molding material we modulate the elastic modulus of the micropillars in the wet state over three orders of magnitude. By minimizing the sum of elastic bending energy and the capillary meniscus interaction energy of the pillars in a cluster, we derive an expression for the micropillar cluster size which is inversely proportional to the elastic modulus of the pillars. The derived relation agrees well with the experimental observation. The critical elastic modulus for stability as calculated from the expression derived in Chapter 5 is also in agreement with the experimental observation whereas the critical modulus calculated by the Laplace pressure approach is found to be much larger than the values

suggested by experiment. These experimental and theoretical studies further demonstrate that in case of 2D micropillar arrays, capillary meniscus interaction rather than the Laplace pressure difference is the relevant capillary force. Further, we demonstrate the utility of the randomly clustered micropillar arrays as biomimetic ultrathin whitening layers.

While in Chapters 5 and 6 we focus on the effect of capillary force on the stability of the micropillars, surface roughness, here, the topography of micropillar arrays, can also affect the capillary driven wetting dynamics of a liquid on the rough surface³¹. In particular, it has been known that capillary driven liquid imbibition in rough or porous medium follows $l \sim t^{0.5}$ dynamics^{61,62} where t is the time and l is the distance traveled by the liquid front. In Chapter 7, we theoretically calculate the imbibition dynamics of a droplet on a rough surface such as a micropillar array. We show that because of the shrinking droplet and radial flow geometry, the imbibition dynamics does not follow a simple power law dynamics. The imbibition dynamics starts as $\sim t^{0.5}$ but continues to slow down with time.

1.6 References

- (1) Autumn, K.; Liang, Y. A.; Hsieh, S. T.; Zesch, W.; Chan, W. P.; Kenny, T. W.; Fearing, R.; Full, R. J. *Nature* **2000**, *405*, 681.
- (2) Barthlott, W.; Neinhuis, C. *Planta* **1997**, *202*, 1.
- (3) Geim, A. K.; Dubonos, S. V.; Grigorieva, I. V.; Novoselov, K. S.; Zhukov, A. A.; Shapoval, S. Y. *Nat. Mater.* **2003**, *2*, 461.
- (4) Greiner, C.; del Campo, A.; Arzt, E. *Langmuir* **2007**, *23*, 3495.

- (5) Mahdavi, A.; Ferreira, L.; Sundback, C.; Nichol, J. W.; Chan, E. P.; Carter, D. J. D.; Bettinger, C. J.; Patanavanich, S.; Chignozha, L.; Ben-Joseph, E.; Galakatos, A.; Pryor, H.; Pomerantseva, I.; Masiakos, P. T.; Faquin, W.; Zumbuehl, A.; Hong, S.; Borenstein, J.; Vacanti, J.; Langer, R.; Karp, J. M. *Proc. Natl. Acad. Sci. U.S.A.* **2008**, *105*, 2307.
- (6) Northen, M. T.; Greiner, C.; Arzt, E.; Turner, K. L. *Adv. Mater.* **2008**, *20*, 3905.
- (7) Qu, L.; Dai, L. M.; Stone, M.; Xia, Z. H.; Wang, Z. L. *Science* **2008**, *322*, 238.
- (8) Li, X. M.; Reinhoudt, D.; Crego-Calama, M. *Chem. Soc. Rev.* **2007**, *36*, 1350.
- (9) Tuteja, A.; Choi, W.; Ma, M.; Mabry, J. M.; Mazzella, S. A.; Rutledge, G. C.; McKinley, G. H.; Cohen, R. E. *Science* **2007**, *318*, 1618.
- (10) Ahuja, A.; Taylor, J. A.; Lifton, V.; Sidorenko, A.; Salamon, T. R.; Lobaton, E. J.; Kolodner, P.; Krupenkin, T. N. *Langmuir* **2008**, *24*, 10.
- (11) Krupenkin, T. N.; Taylor, J. A.; Schneider, T. M.; Yang, S. *Langmuir* **2004**, *20*, 3824.
- (12) Cesa, C. M.; Krichgebner, N.; Mayer, D.; Schwarz, U. S.; Hoffman, B.; Merkel, R. *Rev. Sci. Instrum.* **2007**, *78*, 034301.
- (13) du Roure, O.; Saez, A.; Buguin, A.; Austin, R. H.; Chavrier, P.; Siberzan, P.; Ladoux, B. *Proc. Natl. Acad. Sci. U. S. A.* **2005**, *102*, 2390.
- (14) Tan, J. L.; Tien, J.; Pirone, D. M.; Gray, D. S.; Bhadriraju, K.; Chen, C. S. *Proc. Natl. Acad. Sci. U. S. A.* **2003**, *100*, 1484.
- (15) Yang, M. T.; Sniadecki, N. J.; Chen, C. S. *Adv. Mater.* **2007**, *19*, 3119.
- (16) Evans, B. A.; Shields, A. R.; Carroll, R. L.; Washburn, S.; Falvo, M. R.; Superfine, R. *Nano Lett.* **2007**, *7*, 1428.

- (17) Morishima, K.; Tanaka, Y.; Ebara, M.; Shimizu, T.; Kikuchi, A.; Yamato, M.; Okano, T.; Kitamori, T. *Sens. Actuators, B* **2006**, *119*, 345.
- (18) Sniadecki, N. J.; Anguelouch, A.; Yang, M. T.; Lamb, C. M.; Liu, Z.; Kirschner, S. B.; Liu, Y.; Reich, D. H.; Chen, C. S. *Proc. Natl. Acad. Sci. U. S. A.* **2007**, *104*, 14553.
- (19) Sniadecki, N. J.; Lamb, C. M.; Liu, Y.; Chen, C. S.; Reich, D. H. *Rev. Sci. Instrum.* **2008**, *79*, 044302.
- (20) Tanaka, Y.; Sato, K.; Shimizu, T.; Yamato, M.; Okano, T.; Manabe, I.; Nagai, R.; Kitamori, T. *Lab Chip* **2008**, *8*, 58.
- (21) Fan, J. G.; Dyer, D.; Zhang, G.; Zhao, Y. P. *Nano Lett.* **2004**, *4*, 2133.
- (22) Kotera, M.; Ochiai, N. *Microelectron. Eng.* **2005**, *78-79*, 515-520.
- (23) Tanaka, T.; Morigami, M.; Atoda, N. *Jpn. J. Appl. Phys.* **1993**, *32*, 6059-6064.
- (24) Pokroy, B.; Kang, S. H.; Mahadevan, L.; Aizenberg, J. *Science* **2009**, *323*, 237.
- (25) Sidorenko, A.; Krupenkin, T.; Taylor, A.; Fratzl, P.; Aizenberg, J. *Science* **2007**, *315*, 487.
- (26) Saez, A.; Ghibaudo, M.; Buguin, A.; Silberzan, P.; Ladoux, B. *Proc. Natl. Acad. Sci. U. S. A.* **2007**, *104*, 8281.
- (27) Wenzel, R. N. *Ind. Eng. Chem.* **1936**, *28*, 988-994.
- (28) Cassie, A. B. D.; Baxter, S. *Trans. Far. Soc.* **1944**, *40*, 546-551.
- (29) Quere, D. *Annu. Rev. Mater. Res.* **2008**, *38*, 71.
- (30) Lafuma, A.; Quere, D. *Nat. Mater.* **2003**, *2*, 457.
- (31) McHale, G.; Shirtcliffe, N. J.; Aqil, S.; Perry, C. C.; Newton, M. I. *Phys. Rev. Lett.* **2004**, *93*, 036102.

- (32) Kaji, N.; Tezuka, Y.; Takamura, Y.; Ueda, M.; Nishimoto, T.; Nakanishi, H.; Horiike, Y.; Baba, Y. *Anal. Chem.* **2004**, *76*, 15.
- (33) Kim, M. G.; Cho, J. *Adv. Funct. Mater.* **2009**, *19*, 1497.
- (34) Chen, R.; Lu, M. C.; Srinivasan, V.; Wang, Z.; Cho, H. H.; Majumdar, A. *Nano Lett.* **2009**, *9*, 548.
- (35) Kuo, C. W.; Shiu, J. Y.; Chen, P. L. *Chem. Mater.* **2003**, *15*, 2917.
- (36) Tada, T.; Kanayama, T. *J. Vac. Sci. Technol. B* **1998**, *16*, 3934.
- (37) Ansari, K.; van Kan, J. A.; Bettiol, A. A.; Watt, F. *Appl. Phys. Lett.* **2004**, *85*, 476.
- (38) Glassmaker, N. J.; Jagota, A.; Hui, C.-Y.; Kim, J. *J. R. Soc. Interface* **2004**, *1*, 23.
- (39) Zhang, Y.; Lo, C. W.; Taylor, J. A.; Yang, S. *Langmuir* **2006**, *22*, 8595.
- (40) del Campo, A.; Greiner, C. *J. Micromech. Microeng.* **2007**, *17*, R81.
- (41) McAuley, S. A.; Ashraf, H.; Atabo, L.; Chambers, A.; Hall, S.; Hopkins, J. *J. Phys. D: Appl. Phys.* **2001**, *34*, 2769.
- (42) del Campo, A.; Arzt, E. *Chem. Rev.* **2008**, *108*, 911.
- (43) Nie, Z.; Kumacheva, E. *Nat. Mater.* **2008**, *7*, 277.
- (44) Chen, A.; Komura, M.; Kamata, K.; Iyoda, T. *Adv. Mater.* **2008**, *20*, 763.
- (45) Li, Y.; Cai, W.; Duan, G. *Chem. Mater.* **2008**, *20*, 615.
- (46) Lee, P. S.; Lee, O. J.; Hwang, S. K.; Jung, S. H.; Jee, S. E.; Lee, K. H. *Chem. Mater.* **2005**, *17*.
- (47) Rahman, S.; Yang, H. *Nano Lett.* **2003**, *3*, 439.
- (48) Wolfrum, B.; Mourzina, Y.; Mayer, D.; Schwaab, D.; Offenhausser, A. *Small* **2006**, *2*, 1256.
- (49) Xia, Y. N.; Whitesides, G. M. *Annu. Rev. Mater. Sci.* **1998**, *28*, 153.

- (50) Hua, F.; Sun, Y.; Gaur, A.; Meitl, M. A.; Bilhaut, L.; Rotkina, L.; Wang, J.; Geil, P.; Shim, M.; Rogers, J. A. *Nano, Lett.* **2004**, *4*, 2467.
- (51) Decker, C.; Jenkins, A. D. *Macromolecules* **1985**, *18*, 1241.
- (52) Hui, C. Y.; Jagota, A.; Lin, Y. Y.; Kramer, E. J. *Langmuir* **2002**, *18*, 1394.
- (53) Roca-Cusachs, P.; Rico, F.; Martinez, E.; Toset, J.; Farre, R.; Navajas, D. *Langmuir* **2005**, *21*, 5542.
- (54) Denkov, N. D.; Velev, O. D.; Kralchevsky, P. A.; Ivanov, I. B.; Yoshimura, H.; Nagayama, K. *Langmuir* **1992**, *8*, 3183-3190.
- (55) Stoykovich, M. P.; Cao, H. B.; Yoshimoto, K.; Ocola, L. E.; Nealey, P. F. *Adv. Mater.* **2003**, *15*, 1180-1184.
- (56) Segawa, H.; Yamaguchi, S.; Yamazaki, Y.; Yano, T.; Shibata, S.; Misawa, H. *Appl. Phys. A* **2006**, *83*, 447.
- (57) Chakrapani, N.; Wei, B.; Carrillo, A.; Ajayan, P. M.; Kane, R. S. *Proc. Natl. Acad. Sci. U. S. A.* **2004**, *101*, 4009.
- (58) Lee, T. W.; Mitrofanov, O.; Hsu, J. W. R. *Advanced Functional Materials* **2005**, *15*, 1683-1688.
- (59) Kralchevsky, P. A.; Paunov, V. N.; Ivanov, I. B.; Nagayama, K. *J. Colloid Interface Sci.* **1992**, *151*, 79.
- (60) Zhao, Y. P.; Fan, J. G. *Appl. Phys. Lett.* **2006**, *88*, 103123.
- (61) Bico, J.; Tordeux, C.; Quere, D. *Europhys. Lett.* **2001**, *55*, 214.
- (62) Washburn, E. W. *Phys. Rev.* **1921**, *17*, 273.

Chapter 2

Capillary Force

In this Chapter, we present theoretical background relevant to the capillary force induced clustering of micropillar arrays and capillary driven wetting dynamics in micropillar arrays presented in later chapters.

2.1 Origin of capillary force

Capillary forces are ubiquitous in nature and are responsible for a wide range of macroscopic and microscopic phenomenon ranging from rise of liquid in a capillary tube and clumping together of wet fibers^{1,2} to self-assembly of microparticles³. The origin of these forces is fundamentally the surface or interfacial energy. In a finite volume of condensed matter (liquid or solid), the molecules in the bulk experience attractive interaction from other molecules in all directions. However, molecules or atoms at an interface – liquid-vapor, solid-vapor, or solid-liquid – are in an environment different than that in bulk. This result in excess energy associated with the formation of a unit surface or interfacial area, denoted as interfacial energy, γ (unit, J/m²). Interfacial energy can also be viewed as surface tension force per unit length (unit, N/m). In a system of solid bodies and a liquid volume, it is the tendency of the system to minimize the sum of its three interfacial energies, which is the fundamental reason behind the capillary forces. The three interfacial energies are related to each other by the Young's equation⁴,

$$\gamma_{lv} \cos \theta = \gamma_{sv} - \gamma_{sl} \quad (2.1)$$

where l , v and s denote liquid, vapor and solid respectively and θ is the contact angle that liquid l makes with solid s (Fig. 2.1). The Young's equation itself can be derived by minimizing the sum of the interfacial energies for a fixed droplet volume of liquid l and surface of solid s .

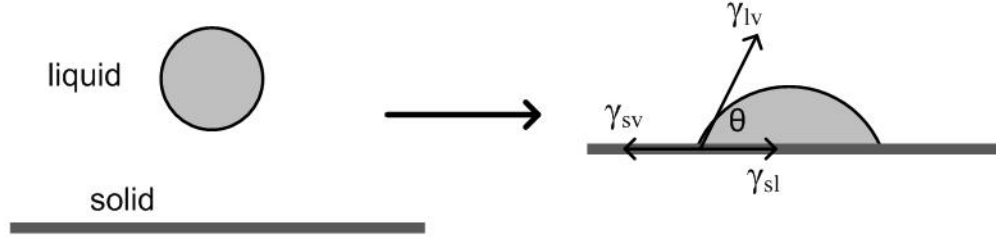


Figure 2.1 A liquid droplet on a solid surface.

Although the origin of all the capillary forces is minimization of total interfacial energy, their manifestation can be different depending on the system geometry. In the following sections we discuss surface tension force, Laplace pressure, and lateral capillary meniscus interaction forces, which are relevant to deformation in high aspect-ratio microstructures.

2.2 Surface tension force

As mentioned above, interfacial energy can also be viewed as force per unit length. For example, consider a liquid film of surface energy γ_{lv} on a wire loop whose one side is free to move (Fig. 2.2a). Displacement of the free side by an amount dx increases the surface energy by $dW = 2l\gamma_{lv}dx$. Thus, the force per unit length is

$F = (1/l)dW/dx = 2\gamma_{lv}$. Here, the factor of 2 is because of the two sides of the liquid film.

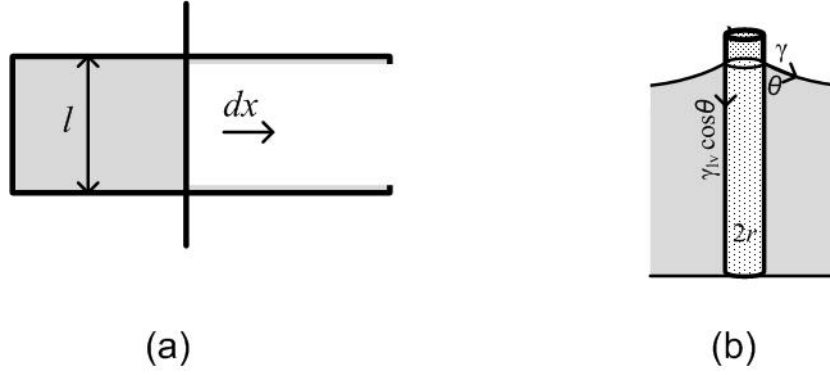


Figure 2.2 (a) A liquid film spanning a wire loop, (b) surface tension force on a cylinder.

As shown schematically in Fig. 2.2b, liquid surface tension can exert a compressive force, $2\pi r\gamma_{lv} \cos \theta$ on a rod of radius r and is responsible for buckling of microfilaments such as carbon nanotube bundles and biological filaments⁵. Balancing this compressive force with the Euler buckling load yields a critical aspect ratio⁵, $(l/2r)_c$, above which the microfilaments bend.

$$\left(\frac{l}{2r}\right)_c = \left(\frac{\pi^2 Er}{32\gamma_{lv} \cos \theta}\right)^{1/2} \quad (2.2)$$

From the above equation, for a 1 μm diameter filament with an aspect-ratio of 10, an elastic modulus of more than 50 MPa is necessary to avoid buckling by water, assuming a water contact angle of 0° .

2.3 Laplace pressure

Surface energy also results in a pressure difference across a curved liquid surface⁴. This pressure difference is called Laplace pressure after Pierre-Simone Laplace who first studied it in the beginning of 19th century. Thus, a liquid droplet has an excess pressure inside it because of its curved surface. In the simple case of spherical surface, the origin of Laplace pressure can be understood as follows. Consider a spherical liquid droplet of radius R . Let the pressure inside the droplet is P_i and the pressure outside is P_o . Increasing the droplet radius by amount dR will result in a work done dW given as,

$$dW = (P_o - P_i)dV + \gamma_{lv}dA \quad (2.3)$$

where $dV = 4\pi R^2 dR$ is the increase in droplet volume, $dA = 8\pi R dR$ is the increase in droplet surface area, and γ_{lv} is the surface energy. In equilibrium, $dW = 0$, yielding the Laplace pressure difference,

$$\Delta P = P_i - P_o = \frac{2\gamma_{lv}}{R} \quad (2.4)$$

In the case of liquid surfaces with arbitrary shape, the Laplace pressure is given as⁴,

$$\Delta P = \gamma_{lv} \left(\frac{1}{R_1} + \frac{1}{R_2} \right) \quad (2.5)$$

The above equation is called the Laplace equation of capillarity, and R_1 and R_2 are the principal radii of curvature of the liquid surface.

The Laplace pressure is responsible for distortion of photoresist patterns while drying off the rinse liquid^{6,7}. During drying a liquid off their surface, isolated capillary bridges, with curved surface form between the microstructures (for example between two

plates in Fig. 2.3). The two radii of curvature of the curved liquid surface in Fig. 2.3 are $x/2\cos\theta$ and ∞ . Thus, by Eq. 2.5, the Laplace pressure difference is,

$$\Delta P = P_1 - P_2 = \left(\frac{2\gamma_{lv}\cos\theta}{x} \right) \quad (2.6)$$

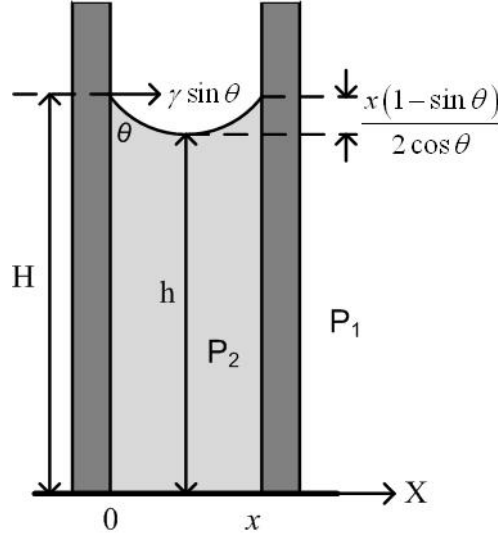


Figure 2.3 Laplace pressure force due to capillary bridge between two parallel plates.

To emphasize that the capillary forces are fundamentally due to the tendency of a system to minimize its interfacial energies, we re-derive Eq. 2.6 by minimizing the sum of interfacial energies for the system of two plates and a liquid capillary bridge of fixed volume V in Fig. 2.3. Let the width of the plates (inside the plane of the paper) as L and the total surface area of the plates as A_0 . The volume V of the liquid between the plates is given as,

$$V = xhL + \frac{x^2L}{4\cos^2\theta} \left(2\cos\theta - \sin\theta\cos\theta + \theta - \frac{\pi}{2} \right) \quad (2.7)$$

The solid-liquid surface area, A_{sl} and liquid-vapor surface area, A_{lv} are given as,

$$A_{sl} = \left(2h + x \left[\frac{1 - \sin \theta}{\cos \theta} \right] \right) L \quad (2.8)$$

$$A_{lv} = \frac{xL}{\cos \theta} \left(\frac{\pi}{2} - \theta \right) \quad (2.9)$$

and the solid-vapor surface area is, $A_{sv} = A_0 - A_{sl}$.

Thus, the total interfacial energy, $U = A_{sl}\gamma_{sl} + A_{lv}\gamma_{lv} + A_{sv}\gamma_{sv}$ can be written as,

$$U = A_0\gamma_{sv} + \left(2h + x \left[\frac{1 - \sin \theta}{\cos \theta} \right] \right) L(\gamma_{sl} - \gamma_{sv}) + \frac{xL}{\cos \theta} \left(\frac{\pi}{2} - \theta \right) \gamma_{lv} \quad (2.10)$$

By using Eq. 2.1 and 2.7 into Eq. 2.10, followed by differentiation, we obtain the force F on a plate in Fig. 2.3,

$$F = -\frac{dU}{dx} = -\left(\frac{2\gamma_{lv} \cos \theta}{x} \right) LH - (\gamma_{lv} \sin \theta) L \quad (2.11)$$

where $H = h + (x/2 \cos \theta)(1 - \sin \theta)$ (see Fig. 2.3).

In Eq. 2.11, the first term can be immediately recognized as the product of the wetted plate area LH and the Laplace pressure difference as given by Eq. 2.6. The second term is the force in x-direction due to liquid surface tension (see Section 2.2) on the solid-liquid contact line of length L (Fig. 2.3). Negative signs indicate attractive forces.

The above analysis in a simple geometry demonstrates that the origin of different capillary forces is the minimization of the total interfacial energy of the system.

2.4 Lateral capillary meniscus interaction force

When two solid bodies are partially immersed in a liquid, they experience a long-range lateral force (attractive or repulsive, depending on their wetting properties) even in

absence of isolated capillary bridges (section 2.3) and net surface tension force (section 2.2). As shown later in Chapters 5 and 6, this lateral capillary force is responsible for the clustering of micropillar arrays when a liquid is dried off their surface rather than the often reported Laplace pressure force due to isolated capillary bridges.

The origin of the lateral capillary force between partially immersed bodies is the deformation of the liquid surface which is flat in absence of the immersed bodies⁸. Fig. 2.4 shows two vertical cylinders partially immersed in a liquid. Since the liquid wets the cylinders and makes a contact angle θ with their surface, the liquid surface becomes curved. Kralchevsky et al. determined the shape of the meniscus profile around the two cylinders by solving a linearized Laplace equation of capillarity (Eq. 2.5) and obtained an expression for the total energy W of the two cylinders partially immersed in a liquid as⁹

$$W = 2\pi\gamma r^2 \cos^2 \theta \ln \left(\frac{x + \sqrt{x^2 - 4r^2}}{q} \right) \quad (2.12)$$

Thus, the force between the two cylinders is,

$$F = -\frac{dW}{dx} = -\frac{2\pi\gamma r^2 \cos^2 \theta}{\sqrt{x^2 - 4r^2}} \quad (2.13)$$

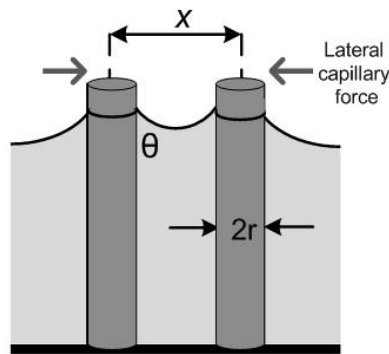


Figure 2.4 Lateral capillary between two cylinders partially immersed in a liquid.

In the limit of large separation ($x \gg r$), $F \sim 1/x$, which is analogous to Coulomb's law of electrostatics in 2-dimensions (2D). Further, the force F is attractive even in case of non-wetting liquid ($\theta > 90^\circ$) in contrast to Laplace pressure force, which is repulsive for non-wetting liquids. If the two bodies have different contact angles θ_1 and θ_2 , the $\cos^2 \theta$ in Eq. 2.13 is replaced by $\cos \theta_1 \cos \theta_2$. Thus, in case of two dissimilar bodies (one hydrophobic and one hydrophilic) the lateral capillary force is repulsive⁸.

Similar expressions with $F \sim 1/x$ dependence have been derived for both partially immersed and floating bodies of different shapes. In case of floating particles, the deformation of liquid surface is attributed to the weight of the particles⁸. The lateral capillary meniscus interaction forces are large enough to cause 2-dimensional close-pack ordering of colloidal particles³. However, as shown in Chapter 5, in a typical case, these forces are much smaller as compared to forces due to Laplace pressure difference in isolated capillary bridges.

2.5 Capillary driven liquid imbibition in rough surface

In addition to mechanical deformation of solids, capillary force also leads to spontaneous liquid flow on a rough surface to minimize the total interfacial energy. By balancing the capillary force to the viscous dissipation in a flowing liquid, in 1921 Washburn derived the classical capillary dynamics, $l \sim t^{0.5}$, where l is the distance traveled by the liquid front and t is time.¹⁰ More recently, Bico et al.¹¹ studied the capillary driven liquid imbibition in rough surfaces and established the condition for imbibition, and obtained the same Washburn dynamics for imbibition in rough surface.

Condition for imbibition: Consider a rough surface in contact with a wetting liquid (Young's contact angle, $\theta_0 < 90^\circ$) (Fig. 2.5). The width of the surface is L (in the plane of paper), the ratio of actual to projected area is r and the solid fraction at top is ϕ . If the liquid imbibes further by an amount dl , the change in energy dE is,

$$dE = (\gamma_{sl} - \gamma_{sv})(r - \phi)Ldl + \gamma_{lv}(1 - \phi)Ldl \quad (2.14)$$

The liquid should imbibe spontaneously within the grooves if $dE < 0$. Using Eq. 2.1, this gives the imbibition condition as $\theta_o < \theta_c$, where,

$$\cos \theta_c = \frac{1 - \phi}{r - \phi} \quad (2.15)$$

Dynamics of imbibition: Let the velocity of the liquid front is V (Fig. 2.5). Then the rate of viscous energy dissipation is,

$$\eta L l \int_0^\delta \left(\frac{dV}{dy} \right)^2 dy \sim \eta L l \frac{V^2}{\delta} = \frac{\eta L l}{\delta} \left(\frac{dl}{dt} \right)^2 \quad (2.16)$$

and the rate of change of capillary energy is $\sim L \gamma_{lv} (dl/dt)$. Equating the two energies and integrating yields the classical Washburn dynamics, $l \sim t^{0.5}$.

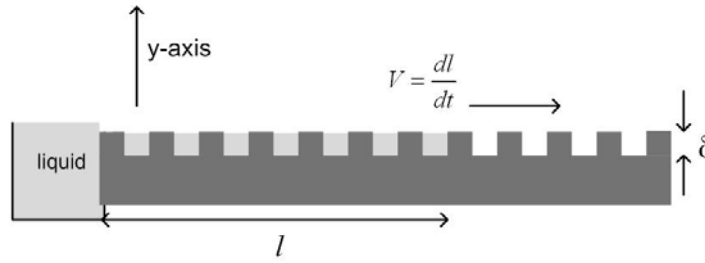


Figure 2.5 Liquid imbibition on a rough surface.

The above analysis is for one-dimensional (1D) flow with an unlimited liquid reservoir. However, as we will show in Chapter 7, that in case of a droplet imbibing on a

rough surface, because of the shrinking droplet and radial flow geometry, the imbibition dynamics does not follow a simple power law dynamics. In particular, the dynamics starts as $\sim t^{0.5}$ and progressively becomes slower than $\sim t^{0.5}$ with time.

2.6 References

- (1) Bico, J.; Roman, B.; Moulin, L.; Boudaoud, A. *Nature* **2004**, *432*, 690.
- (2) Py, C.; Bastien, R.; Bico, J.; Roman, B.; Boudaoud, A. *Europhys. Lett.* **2007**, *77*, 44005.
- (3) Denkov, N. D.; Veleev, O. D.; Kralchevsky, P. A.; Ivanov, I. B.; Yoshimura, H.; Nagayama, K. *Langmuir* **1992**, *8*, 3183-3190.
- (4) de Gennes, P. G.; Brochard-Wayrt, F.; Quere, D. *Capillarity and Wetting Phenomena*; Springer 2004.
- (5) Cohen, A. E.; Mahadevan, L. *Proc. Natl. Acad. Sci. U. S. A.* **2003**, *100*, 12141.
- (6) Stoykovich, M. P.; Cao, H. B.; Yoshimoto, K.; Ocola, L. E.; Nealey, P. F. *Adv. Mater.* **2003**, *15*, 1180-1184.
- (7) Tanaka, T.; Morigami, M.; Atoda, N. *Jpn. J. Appl. Phys.* **1993**, *32*, 6059-6064.
- (8) Kralchevsky, P. A.; Nagayama, K. *Particles at fluid interfaces and membranes*; Elsevier Science, 2001.
- (9) Kralchevsky, P. A.; Paunov, V. N.; Ivanov, I. B.; Nagayama, K. *J. Colloid Interface Sci.* **1992**, *151*, 79.
- (10) Washburn, E. W. *Phys. Rev.* **1921**, *17*, 273.
- (11) Bico, J.; Tordeux, C.; Quere, D. *Europhys. Lett.* **2001**, *55*, 214.

Chapter 3

Experimental Methods

In this Chapter, we describe the materials and methods used in fabrication and characterization of the micropillar arrays. The polymeric micropillar arrays were fabricated by replica molding of the corresponding Si masters. A range of characterization techniques were used to characterize the structural, mechanical, wetting and surface properties of the micropillar arrays.

3.1 Materials

All the materials were used as received without any further purification.

3.1.1 Micropillar arrays

We fabricated hydrogel micropillar arrays by using a variety of monomers or monomer mixtures. The monomers used were 2-hydroxyethyl methacrylate (HEMA) (98%, Aldrich), methyl methacrylate (MMA) (99%, Acros Organics), N-isopropyl acrylamide (NIPA) (99%, Aldrich) and ethylene glycol dimethacrylate (EGDMA) (98%, Alfa Aesar). EGDMA was also used as cross-linker. The structures of the monomers used are shown in Fig. 3.1. 2-hydroxy-2-methyl-1-phenyl-1-propanone (Darocur 1173, Ciba Speciality Chemicals Inc.) was used as photoinitiator for the hydrogel micropillar arrays. Epoxy micropillar arrays in Chapter 5 were fabricated by molding a mixture of epoxy resin (DER 354, Dow Chemicals) and 3wt% photoinitiator (Cycracure UVI 6976, Dow Chemicals).

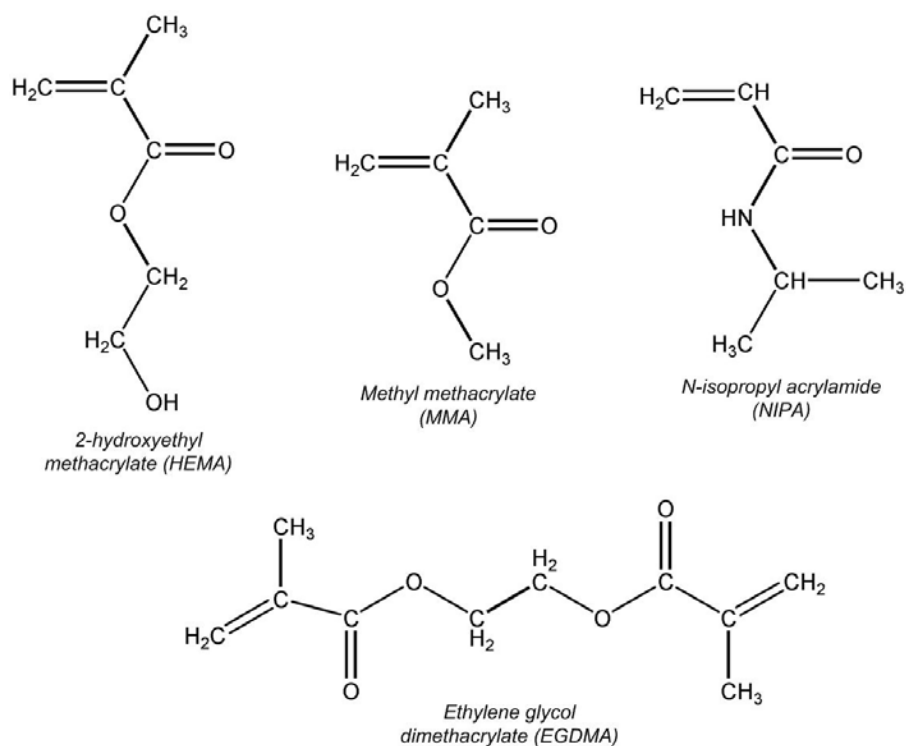


Figure 3.1 Monomers used for fabrication of micropillar arrays.

3.1.2 Molds

The elastomeric molds used in this work were fabricated by thermal curing of a mixture of poly(dimethyl siloxane) (PDMS) precursor and its curing agent (RTV 615 from GE Silicones or Sylgard 184 from Dow Corning). Fluoro-silane, (tridecafluoro-1,1,2,2-tetrahydrooctyl) trichlorosilane (Gelest), was used as a release agent for easy removal of PDMS molds from the master.

3.1.3 Wetting liquids

For clustering the micropillar arrays, water was used as the wetting liquid. To visualize the liquid wetting profile in the micropillar arrays in Chapter 5, low molecular weight, monodisperse, molten polystyrene ($M_n = 1.79$ kg/mol, PDI = 1.06, PSS - Polymer

Standards Service-USA Inc.) was used as the wetting liquid to facilitate imaging after solidification.

3.2 Fabrication

The micropillar arrays in this thesis were fabricated by replica molding method. Replica molding¹ is one of the soft lithographic techniques developed in the 1990s to facilitate patterning of soft materials such as polymers and biomaterials at the micro and nanoscale.

The most widely used microfabrication technique, photolithography, is limited by its very nature to a very narrow class of photosensitive materials, photoresists. Using the patterned photoresist film as an etch mask to define structures in other materials is a multi-step and expensive process. Moreover, the resolution achieved is limited by the diffraction limit of the photon source used. Other techniques such as e-beam and ion beam writing can generate very small (down to a few nanometers) features but are very expensive, difficult and non-scalable to large areas limiting them to mask fabrication and laboratory applications.

Replica molding technique is an inexpensive, single-step, fast and easy processes in which structures are defined by a mold having predefined topography followed by suitable curing (e.g. UV, thermal). The molds themselves, which can be used many times, are replicated from a master pattern, which is often fabricated by top-down lithographic methods. Since the structures are defined physically by a mold, it is not required to have specific chemical functionality in the molding materials; therefore, replica molding technique can be used to mold a large variety of soft materials as long as they do not

damage the mold. Here, we have employed a widely used material, PDMS, to fabricate molds. The master silicon micropillars were fabricated by inductively coupled deep plasma etching² of silicon after defining the structures in a photoresist.

Crosslinked PDMS possesses many unique properties, which makes it ideal as a mold material¹. PDMS is a soft elastomer with a low surface energy (~ 21.6 mN/m) which facilitates its easy release from both the master pattern and the molded pattern even in the case of high aspect ratio microstructures. To further avoid any damage to the original silicon micropillars, we treated the silicon micropillars with a fluorosilane layer before making PDMS molds. PDMS is optically transparent up to UV, allowing molding of UV-curable materials. In addition, PDMS is permeable to gases, allowing easy release of trapped air in the mold channels as the molding material fills the channels.

Although PDMS molds have been used to replicate structures in a variety of materials, they cannot be used for directly molding hydrogel monomers. The monomers easily diffuse into the molds and the oxygen dissolved in the porous mold diffuses in the molding material and inhibits the free-radical polymerization³ and crosslinking of the gels during UV-curing. To avoid this problem, as explained in Chapter 4, we have used a modified two-step molding process. In the first step, the monomers or monomer mixtures were partially UV-polymerized to obtain a viscous molding precursor. In the second step, this precursor was molded and UV-cured after adding crosslinker and additional photoinitiator. The increased viscosity in the first step effectively prevented both the monomer diffusion in the mold and the oxygen diffusion in the molding precursor.

3.3 Characterization

The hydrogel micropillar arrays were characterized for their structural, mechanical, surface and wetting properties as described below.

3.3.1 Structural characterization

The structure of the micropillars in both the pristine state and after collapsing by capillary force was characterized by scanning electron microscope (SEM). In SEM, a focused beam of electrons is incident on the sample and scanned in x-y direction over the desired sample area⁴. The electrons are emitted from either a thermionic or a field-emission electron gun and can be accelerated up to 30 keV. The electron beam is focused by condenser lenses and passed through scanning coils. After the electron beam hits the sample it interact with the sample to produce backscattered electrons, secondary electrons and radiation which can be detected for imaging or other sample analysis purposes. The secondary electrons scattered from each incident point on the sample surface are detected to form an entire image from a full scan.

In this work, we used FIB Strata DB 235, field-emission scanning electron microscope to image our samples by secondary electron detector. An acceleration voltage of 5kV was used for the electron beam with a spot size 3. To prevent static charge accumulation due to electron beam on our non-conducting samples, we sputter coated a thin layer of platinum on the samples before imaging.

3.3.2 Mechanical characterization

The elastic moduli of the micropillar materials were characterized by indentation technique. In this technique, the sample surface is indented by an indenter of known geometry and the indentation depth is recorded as a function of applied load. Depending

on the indenter geometry, the elastic modulus of the sample can be determined from the indentation-load curve. In case of a spherical indenter whose elastic modulus is much larger than that of the probed sample and neglecting adhesion, Hertz theory gives the following relation⁵ between the applied force, F and indentation depth, δ .

$$F = \frac{4r^{1/2}E}{3(1-\nu^2)}\delta^{3/2} \quad (3.1)$$

where r is the indenter radius, and E and ν are the elastic modulus and Poisson's ratio of the sample, respectively. In case of conical indenter⁶, under similar assumptions the load-indentation relation is given as

$$F = \frac{2E \tan \alpha}{\pi(1-\nu^2)}\delta^2 \quad (3.2)$$

where α is the half opening angle of the conical indenter.

In Chapter 4, we have used a commercial indentation instrument (MTS Nanoindenter XP) with a built-in analysis software to determine the elastic modulus of dry hydrogel samples. The indenter was a spherical diamond indenter with a radius of 13.5 μm .

In Chapter 6, we used an atomic force microscope (AFM) (Multimode AFM, Digital Instruments) nanoindentation^{5,7,8} in a fluid cell to measure the elastic modulus of our hydrogel samples in hydrated state. We used rectangular silicon cantilever with a conical tip at the end as nanoindenter.

In AFM nanoindentation, the cantilever tip is brought in contact and indented in the sample of interest⁹. The relative motion between the cantilever and the tip is controlled on nanometer scale by means of piezoelectric tube. Either the sample or the

cantilever can be mounted on the piezo tube keeping the other one fixed. Once the tip comes in contact of the sample, upon further piezo movement, the cantilever deflects and also the tip indents the sample (Fig. 3.2). The cantilever deflection is measured by reflecting a laser off the

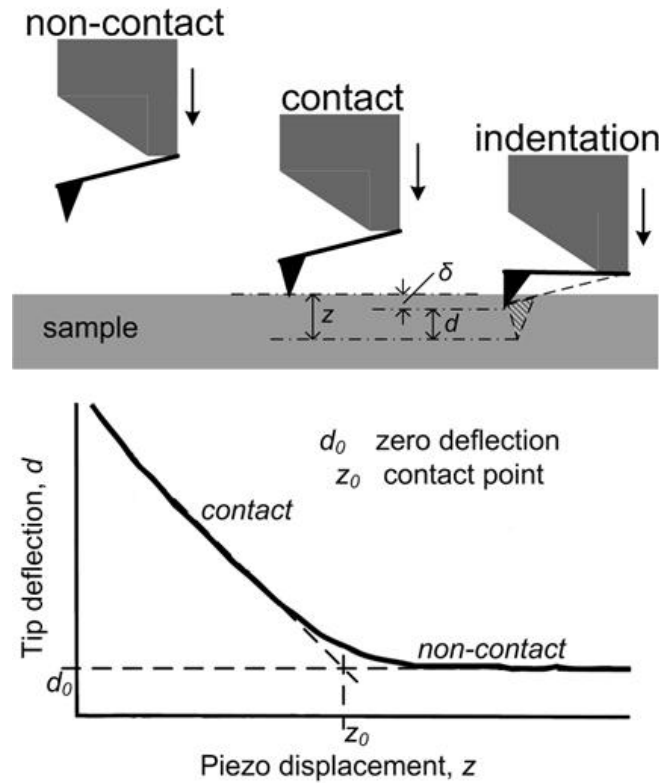


Figure 3.2 Schematic illustration of AFM nanoindentation and a typical tip deflection vs. piezo displacement curve.

cantilever back and detecting the reflected laser on a position sensitive photodiode. By this method, a plot is obtained between cantilever deflection d and piezo displacement z (Fig. 3.2) which is analyzed to get elastic modulus of the sample. In case of infinitely stiff sample, after contact there will be no indentation and the cantilever deflection d is equal to the piezo deflection z . On the other hypothetical extreme, in case of zero sample

stiffness, there will be no tip deflection ($d = 0$) regardless of piezo displacement z . In all other cases, indentation δ is given as,

$$\delta = z - d \quad (3.3)$$

The force applied by a cantilever tip deflected by amount d , on the sample is

$$F = kd \quad (3.4)$$

where k is the spring constant of the cantilever. The spring constant of the cantilever was determined by the resonant frequency method as outlined by Sader and co-workers¹⁰. In this method, only the length and width of the cantilever and its resonant frequency and quality factor is required to determine its resonant frequency. The resonant frequency and quality factor is readily determined by the AFM in tapping mode and the cantilever dimensions can be obtained by an optical microscope. By this method, the spring constant is given as,

$$k = 0.1906 \rho_f b^2 L Q_f \Gamma_i \omega_f^2 \quad (3.5)$$

where L and b are the length and width of the rectangular cantilever, respectively, ω_f and Q_f are the resonant frequency and the quality factor of the cantilever in fluid (air), respectively, ρ_f is the fluid (air) density and Γ_i is the imaginary part of the hydrodynamic function (available from literature^{10,11}), which is function of Reynold's number, $Re = \rho_f \omega_f b^2 / 4\eta$, where η is the fluid viscosity. Once k is known, the modulus can be determined from the d vs. z plot by means of Eqs. 3.2 -3.4.

3.3.3 Surface energy and wetting characterization

We used Ramé-Hart goniometer with DROPimage Standard software to determine liquid contact angles on our samples. In this method, a small (\sim few micro liters) liquid droplet placed on a substrate is imaged by a camera. A circle is fit to the

drop profile to determine the contact angle. In Chapter 4, we measured the contact angles of a polar (water) and a non-polar (methylene iodide) liquid on our samples to determine the sample surface energy from the contact angle data by harmonic mean method provided by the DROPImage Standard software. In the harmonic mean method¹², it is assumed that the work of adhesion between two surfaces is twice the harmonic mean of their surface energies. Further, the surface energies are sum of polar and non-polar (dispersive) components. Work of adhesion between two components, liquid 1 and solid S is defined as $W_{1S} = \gamma_1 + \gamma_S - \gamma_{1S}$. According to Young's equation, $W_{1S} = \gamma_1 (1 + \cos \theta_1)$, where θ_1 is the contact angle of liquid 1 on solid S . Further, writing the surface energy as sum of the polar and dispersive components, for pair of liquid 1 and solid S we get,

$$\gamma_1 (1 + \cos \theta_1) = \frac{4\gamma_1^d \gamma_S^d}{\gamma_1^d + \gamma_S^d} + \frac{4\gamma_1^p \gamma_S^p}{\gamma_1^p + \gamma_S^p} \quad (3.6)$$

where superscripts d and s denote dispersive and polar components, respectively. Similar equation can be obtained for a pair of liquid 2 and solid S .

$$\gamma_2 (1 + \cos \theta_2) = \frac{4\gamma_2^d \gamma_S^d}{\gamma_2^d + \gamma_S^d} + \frac{4\gamma_2^p \gamma_S^p}{\gamma_2^p + \gamma_S^p} \quad (3.7)$$

In these two Eqs. 3.6 and 3.7, θ_1 and θ_2 are measured by goniometer. Thus, if the surface energy components of the two liquids are known, the two components of the surface energy of solid S can be obtained by solving the Eq. 3.6 and Eq. 3.7 together.

In Chapter 5, we characterized the wetting profile in micropillar arrays by using low molecular weight molten polystyrene as wetting liquid and after solidification, imaged by AFM.

3.3.4 Optical characterization

In Chapter 6, we discussed utilizing the randomly clustered micropillar array for ultrathin whiteness. The whiteness was measured by CIE lightness index¹³, L , using a photospectrometer (MHT Spectro Shade Micro). White light is incident on the sample at an angle of 45^0 from the surface normal and diffuse reflectance is measured by measuring the reflectance in the direction normal to the sample. L represents diffuse reflectance of a surface on a scale from 0 to 100, 0 being black and 100 being perfect white.

3.4 References

- (1) Xia, Y. N.; Whitesides, G. M. *Annu. Rev. Mater. Sci.* **1998**, 28, 153.
- (2) McAuley, S. A.; Ashraf, H.; Atabo, L.; Chambers, A.; Hall, S.; Hopkins, J. J. *Phys. D: Appl. Phys.* **2001**, 34, 2769.
- (3) Decker, C.; Jenkins, A. D. *Macromolecules* **1985**, 18, 1241.
- (4) Goldstein, J. I.; Newbury, D. E.; Echlin, P.; Joy, D. C.; Lyman, C. E.; Lifshin, E.; Sawyer, L.; Michael, J. R. *Scanning Electron Microscopy and X-Ray Microanalysis*; Kluwer Academic Publishers, 2003.
- (5) Cappella, B.; Kaliappan, S. K.; Sturm, H. *Macromolecules* **2005**, 38, 1874.
- (6) Sneddon, I. N. *Int. J. Eng. Sci.* **1965**, 3, 47.
- (7) Domke, J.; Radmacher, M. *Langmuir* **1998**, 14, 3320.
- (8) Dong, R.; Jensen, T. W.; Engberg, K.; Nuzzo, R. G.; Leckband, D. E. *Langmuir* **2007**, 23, 1483.
- (9) Bhushan, B. *Springer Handbook of Nanotechnology*; Springer-Verlag, 2004.
- (10) Sader, J. E.; Chon, J. W. M.; Mulvaney, M. *Rev. Sci. Instrum.* **1999**, 70, 3967.

- (11) Sader, J. E. *J. Appl. Phys.* **1998**, 84, 64.
- (12) Wu, S. *Polymer Interface and Adhesion*; Marcel Dekker, 1982.
- (13) Wyszecki, G.; Stiles, W. S. *Color Science Concepts and Methods, Quantitative Data and Formulae*; Second ed.; John Wiley and Sons, Inc., 2000.

Chapter 4

Replica Molding of High Aspect-Ratio Hydrogel Micropillar Arrays

High aspect-ratio hydrogel micropillar arrays are attractive in many applications, such as tissue engineering, actuation, and sensing. Their chemical and physical properties can be tailored for specific applications. For example, by simply varying the composition of the hydrogel materials, mechanical properties of the resulting micropillars can be tuned. In this Chapter using a two-step replica molding method we fabricated hydrogel micropillar arrays in different materials and geometries, and investigated their stability against adhesive and capillary forces.

4.1 Introduction

Owing to their many potential applications, HAR micropillar arrays have been fabricated in a variety of both inorganic¹⁻⁵ and organic⁶⁻¹¹ materials by employing top-down^{1,2,7,10}, self-assembly⁴ and replica molding^{6,8,11} approaches (Section 1.3). However, it remains a challenge to fabricate high-aspect-ratio hydrogel micropillar arrays.

Because of their biocompatibility, softness, and porous nature, hydrogels are of interest in living cell studies and tissue engineering¹². Their chemical and physical properties can be easily tailored, and many of them are sensitive to external stimuli, such as solvent, pH, temperature and electric field, therefore, attractive for applications of sensors and actuators.¹² Most reported hydrogels, however, have been patterned by

photolithography directly from the respective liquid monomer solutions,¹³⁻¹⁶ where poor control over free-radical diffusion during polymerization has limited the feature resolution. In addition, large volume shrinkage often occurs during polymerization,^{17,18} leading to dimensional distortion for complex structures. Replica molding¹⁹ from PDMS has been applied to pattern hydrogels from both monomers²⁰ and polymers.²¹⁻²³ However, the aspect-ratio of the patterned structures is often less than 5 with feature sizes on the order of tens of microns. It is found difficult to directly mold hydrogels from their monomers because the oxygen dissolved in the PDMS mold could diffuse out and inhibit the free-radical polymerization²⁴ beyond the skin around the PDMS channels. This problem is further aggravated when the surface area to volume ratio increases with the aspect ratio and the feature size of PDMS channels is decreased to sub-micron scale.

Here, we describe a modified replica molding approach through a two-stage process to fabricate dense (up to 4.4×10^7 pillars/cm²), high-aspect-ratio (up to 12) hydrogel pillar arrays with feature size ranging from 350 nm to 1 μ m. First, the monomers were partially photopolymerized. The precursor solution was then mixed with a crosslinker and additional photoinitiators for molding. We found that the partial polymerization step was critical to the success of replica molding of the high-aspect-ratio hydrogel pillars. It minimized the problems caused by oxygen inhibition and by diffusion of monomers into the mold. To demonstrate the versatility of our fabrication method, we studied three different polymer systems, including poly(hydroxyethyl methacrylate) (PHEMA), poly(hydroxyethyl methacrylate-*co*-*N*-isopropylacrylamide) (PHEMA-*co*-PNIPA) and poly(ethylene glycol dimethacrylate) (PEGDMA), which were photocrosslinked by EGDMA. PHEMA based hydrogels are commonly used in

biomedical applications,¹² such as contact lenses. PNIPA is temperature responsive and its hydrogels have been studied for drug delivery, tissue engineering, and responsive optics.¹² PEGDMA based materials have been used in dental fillings²⁵. For various applications, it will be important to investigate the stability of these hydrogel pillars in both the dry and wet states. We found that in the dry state, because of the high elastic moduli, all the structures remained stable. When exposed to water, PHEMA-*co*-PNIPA micropillars were swollen by water, which effectively reduced the hydrogel mechanical strength. After drying, the pillars were found collapsed to the substrate (i.e. ground collapsed), which was attributed to the decreased stiffness of the pillars. Similar behavior was observed when PHEMA micropillars were treated with water and subsequently dried. In contrast, the surface of highly crosslinked PEGDMA micropillar array was found superhydrophobic, and the pillars remained stable after drying from water. When exposed to a lower surface energy solvent, ethanol, the PEGDMA pillars were wetted and collapsed by the capillary force. Depending on the pillar array geometry, we found that PEGDMA pillars collapsed either randomly (from less dense, smaller diameter micropillar arrays) or in an ordered fashion (from more dense larger diameter ones), forming complex hierarchical micropatterns.

4.2 Experimental methods

4.2.1 Materials

HEMA (98%) and NIPA (99%) monomers were obtained from Aldrich. EGDMA (98%) was obtained from Alfa Aesar. Photoinitiator, Darocur 1173, was obtained from Ciba Specialty Chemicals Inc. All the chemicals were used without further purification.

4.2.2 Replica molding of hydrogel pillars

The fabrication process is outlined in Figure 4.1. In a typical process, 2.5 mL HEMA was mixed with 75 μ L Darocur 1173 in a 20 mL glass vial and exposed to UV light (UVP Blak-Ray, ~ 8 mW/cm²) for 2 minutes to obtain a viscous, partially polymerized PHEMA precursor solution. Before molding, additional 50 μ L Darocur 1173 and 25 μ L EGDMA (crosslinker) were added to this solution to prepare the molding precursor. To obtain partially polymerized PHEMA-*co*-PNIPA solution, 0.5 g NIPA was dissolved in 2.5 mL HEMA mixed with 75 μ L Darocur 1173 in a 20 mL glass vial, followed by UV exposure for 2 minutes. Additional 50 μ L Darocur 1173 and 25 μ L EGDMA was added to this solution for molding. To prepare partially polymerized PEGDMA solution, 2.5 mL EGDMA was mixed with 75 μ L Darocur 1173 in a 20 mL glass vial and exposed to UV light for 30 seconds. Since EGDMA itself is a crosslinker, only 50 μ L Darocur 1173 was added to the viscous solution for the later molding.

PDMS molds were fabricated by mixing PDMS prepolymer and curing agent (RTV 615, GE Silicones) in 8:1 ratio (by weight), which was then cast onto the silicon master, followed by thermal curing at 65°C for 4 hours. The PDMS replica mold was carefully peeled off from the silicon master and used without any further surface treatment. To fabricate the hydrogel pillar array, the molding solution was cast on a pre-cleaned glass slide, and the PDMS mold was pressed over it, followed by UV exposure for 10 minutes before peeling off the PDMS mold.

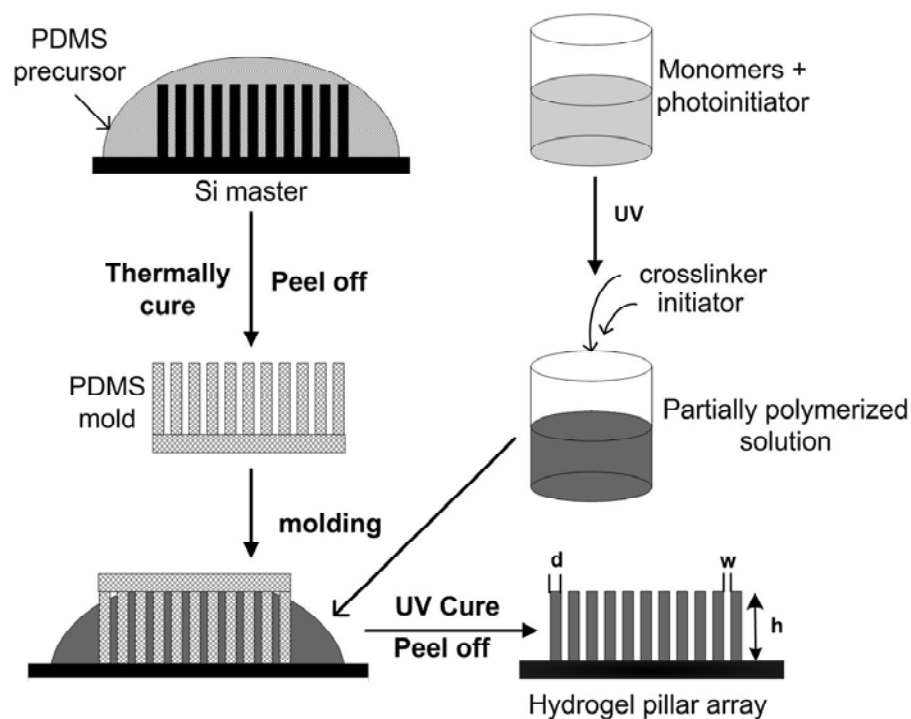


Figure 4.1 Schematic illustration of the fabrication process of hydrogel micropillar arrays.

4.2.3 Characterization

Viscosity of the molding precursors was measured using a Bohlin Gemini Rheometer. Scanning electron microscopy (SEM) images were obtained on FEI Strata DB235 Focused Ion Beam at acceleration voltage of 5 kV and spot size of 3. Contact angles were measured using ramé-hart goniometer with DROPImage Standard software and averaged over at least 3 fresh spots. The surface energies were determined from the contact angles of water and methylene iodide on the hydrogel films using the harmonic mean method provided by the DROPImage Standard software. The Young's modulus of the hydrogel in the dry state was measured by nanoindentation (MTS Nanoindenter XP

instrument) over at least 4 spots using a 13.5 μm radius spherical diamond indenter with a maximum load of 50 mN.

4.3 Results and discussion

4.3.1 Fabrication

The geometry of micropillar arrays fabricated by the method described above is defined in Fig. 4.1, where h is the pillar height, d is pillar width or diameter, and w is the spacing between two adjacent pillars. Three sets of pillars were studied, including 1) square pillars, $d = 1\ \mu\text{m}$, $h = 9\ \mu\text{m}$ (aspect ratio of 9), $w = 1\ \mu\text{m}$, and area density of 2.5×10^7 pillars/ cm^2 , 2) circular pillars, $d = 750\ \text{nm}$, $h = 9\ \mu\text{m}$ (aspect ratio of 12), $w = 750\ \text{nm}$, and area density of 4.4×10^7 pillars/ cm^2 , and 3) conical pillars, $d_{\text{tip}} = 350\ \text{nm}$, $d_{\text{base}} = 750\ \text{nm}$, $h = 7\ \mu\text{m}$, $w_{\text{base}} = 1.25\ \mu\text{m}$, and area density of 2.5×10^7 pillars/ cm^2 .

Our initial attempts to mold the pillar arrays from the respective monomers were unproductive. We suspect that oxygen dissolved in the PDMS mold could inhibit the free-radical polymerization²⁴ of the monomers within the mold channels, especially for sub-micron, high-aspect-ratio structures, which have large surface area to volume ratio. No hydrogel pillars were obtained even when the molding was carried out under nitrogen. Furthermore, we found that the monomers could readily diffuse into the PDMS mold, resulting in swelling and deformation of the mold.

When the monomers are partially polymerized, however, the viscosity of molding liquid increases dramatically, therefore, effectively minimizing the problems due to oxygen diffusion to the molding liquid and the swelling of the PDMS mold. The typical viscosity values vs. the UV exposure time for the mixture of HEMA and NIPA is shown

in Fig. 4.2. Some deviations were observed in different cycles due to the fluctuations of the UV lamp power. For precursors with viscosity ranging from ~500 cps to ~1500 cps, we were able to repeatedly replicate the high density, high-aspect-ratio hydrogel pillar arrays nearly perfectly from the PDMS molds (Fig. 4.3).

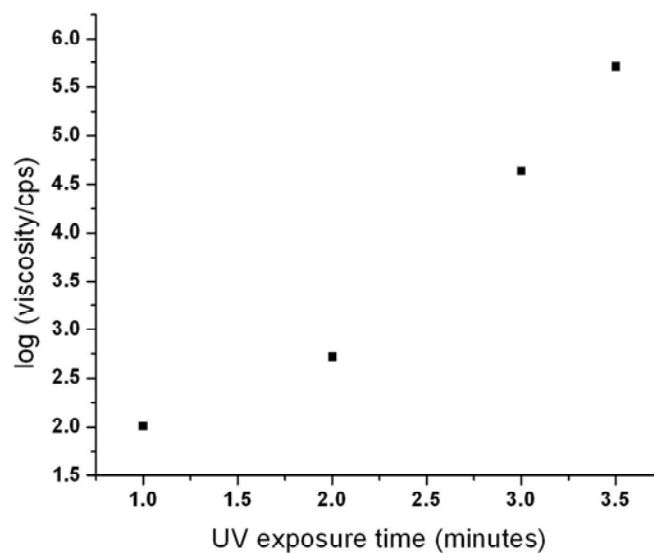


Figure 4.2 Typical viscosity values vs. UV ($\sim 8 \text{ mW/cm}^2$) exposure time for 2.5 mL HEMA mixed with 0.5 g NIPA and 3 wt% photoinitiator.

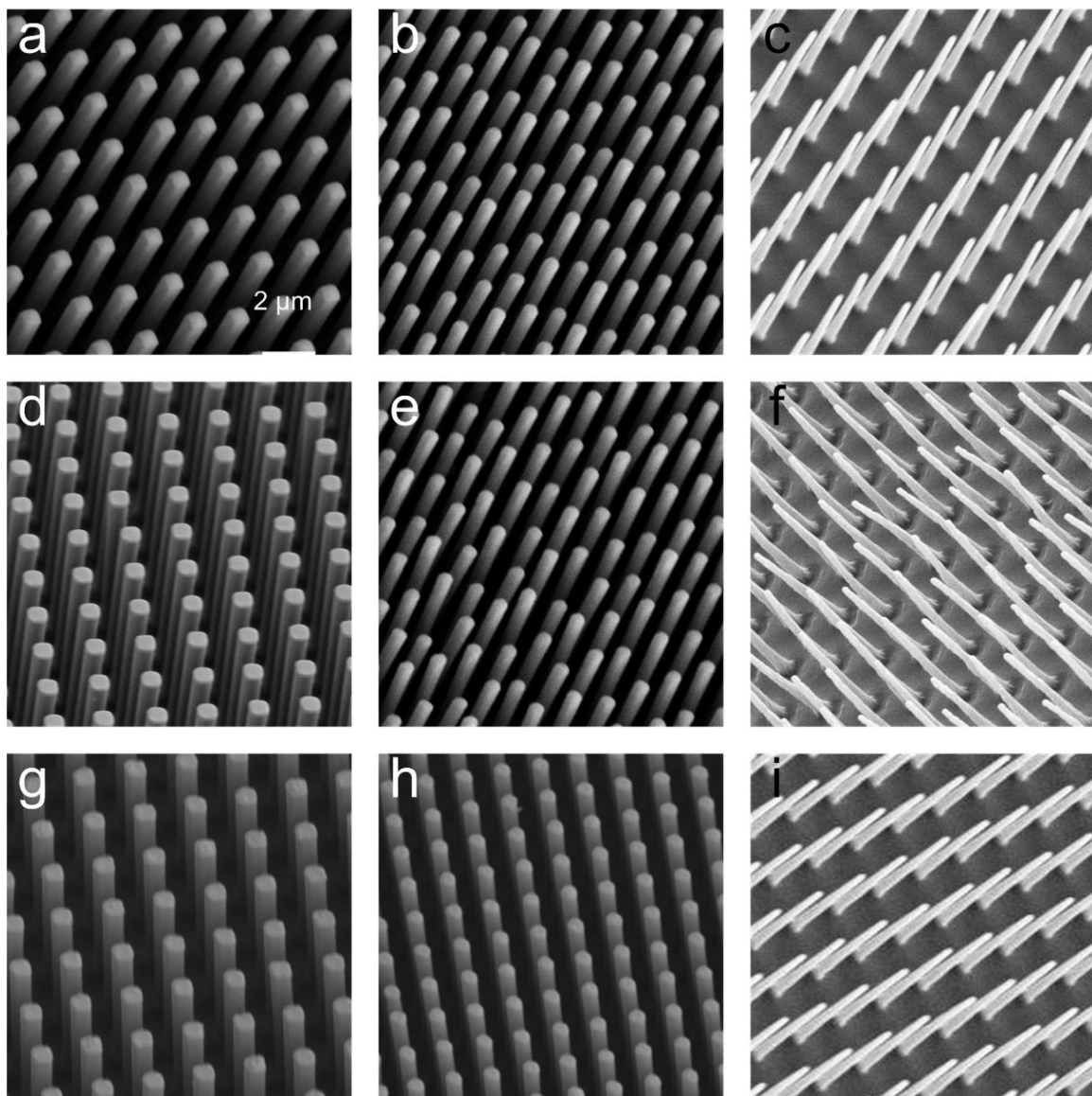


Figure 4.3 SEM images of different hydrogel pillar arrays. (a-c) PHEMA, (d-f) PHEMA-*co*-PNIPA, and (g-i) PEGDMA. (a, d, g) Square pillars: 9 μm tall, 1 μm wide, and adjacent pillar spacing of 1 μm . (b, e, h) Circular pillars: 9 μm tall, 750 nm in diameter, and adjacent pillar spacing of 750 nm. (c, f, i) Conical pillars: 7 μm tall, tip diameter of 350 nm, base diameter of 750 nm, and adjacent pillar spacing of 1.25 μm at base. Scale bar in (a) applies to all the images.

4.3.2 Stability of micropillar arrays in dry state

As shown in an earlier study¹¹, the stability of high-aspect-ratio polymer pillars against adhesive forces depends on the elastic bending energy of the micropillars in collapsed or bent configuration, which competes with the adhesive force between pillars. As the stiffness of the pillars decreases, adhesion force begins to dominate, leading to either ground collapse or lateral collapse (i.e. pillars touching each other). The critical elastic modulus of ground collapse is described as,²⁶

$$E_g^* = \frac{2^{\frac{11}{2}} 3^{\frac{3}{4}} (1-\nu^2)^{\frac{1}{4}} h^{\frac{3}{2}} W}{(\pi d)^{\frac{5}{2}}} \quad (4.1)$$

where, W is work of adhesion and ν is the Poisson ratio. The critical elastic modulus for lateral collapse, E_L^* , can be estimated as,⁸

$$E_L^* = \frac{8h^4 \gamma_s}{3w^2 d^3} \quad (\text{square pillars}) \quad (4.2)$$

$$E_L^* = \frac{2^{1/4} \cdot 32h^3 \gamma_s (1-\nu^2)^{1/4}}{3^{3/4} \pi d^{5/2} w^{3/2}} \quad (\text{circular pillars}) \quad (4.3)$$

where γ_s is the surface energy of the pillar material, which was determined by harmonic mean method²⁷ from the contact angles of water and methylene iodide on the polymer film (see Table 1). E_g^* and E_L^* for conical pillars were estimated using the base diameter and spacing. The elastic modulus, E , of UV cured hydrogels was measured by nanoindentation.²⁸ As shown in Table 4.1, the elastic moduli of the three investigated hydrogel systems are much higher than the required E_g^* and E_L^* for the three pillar array geometries. Therefore, stable, high-aspect-ratio hydrogel pillar arrays were obtained as predicted.

Table 4.1 Surface energy, Young's modulus and critical modulus of ground and lateral collapse for different hydrogel pillar arrays.

	Surface energy, γ (mN/m)	Critical modulus for collapse, (MPa)						Young's modulus, E (MPa)
		Square		Circular		Conical		
		E_L^*	E_g^*	E_L^*	E_g^*	E_L^*	E_g^*	
PHEMA	33.4±0.1	584	8	380	16	83	11	1790±12
PHEMA- <i>co</i> -PNIPA	32.7±0.3	572	8	373	16	82	11	1825±8
PEGDMA	37.6±0.2	658	9	429	18	94	13	1582±26

4.3.3 Stability of micropillar arrays in wet state

When the pillars were immersed in water and subsequently dried, however, they behaved quite differently. Both the PHEMA and PHEMA-co-PNIPA conical pillar arrays ($d_{tip} = 350$ nm, $d_{base} = 750$ nm, $h = 7$ μ m, and $w_{base} = 1.25$ μ m) appeared ground collapsed (Fig. 4.4c) after immersed in water for 15 minutes and blown-dried in air. In contrast, PEGDMA conical pillars remained stable in water even after immersed in water for 30 minutes, followed by blow-drying in air (Fig. 4.5b).

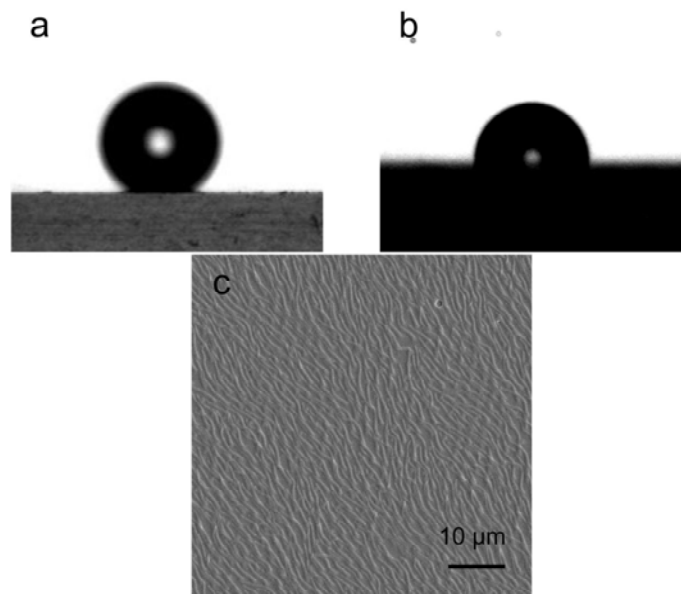


Figure 4.4 Stability and wettability of PHEMA-*co*-PNIPA conical pillar array when exposed to water. (a-b) Optical images of water droplet on PHEMA-*co*-PNIPA conical pillar array. (a) Initial film with water contact angle of 140°. (b) Film after soaking in water for 15 minutes and blown-dry, water contact angle of 83°. (c) SEM image of the ground collapsed hydrogel pillar arrays after air dried corresponding to (b).

Since these hydrogel pillar arrays have the same geometry and size, we believe the very different collapsing behavior could be attributed to their wettability/swellability and capillary force generated during the solvent drying process.²⁹ The stiffness of hydrogels could be drastically decreased when the hydrogel film is swollen by water. For example, the Young's modulus of PHEMA based hydrogels changes from ~1.8 GPa in air to less than 5 MPa in water.^{30,31} Since the behaviors of PHEMA based hydrogels and PHEMA-*co*-PNIPA hydrogels are very similar, we have focused on the comparison between PHEMA-*co*-PNIPA and PEGDMA pillars.

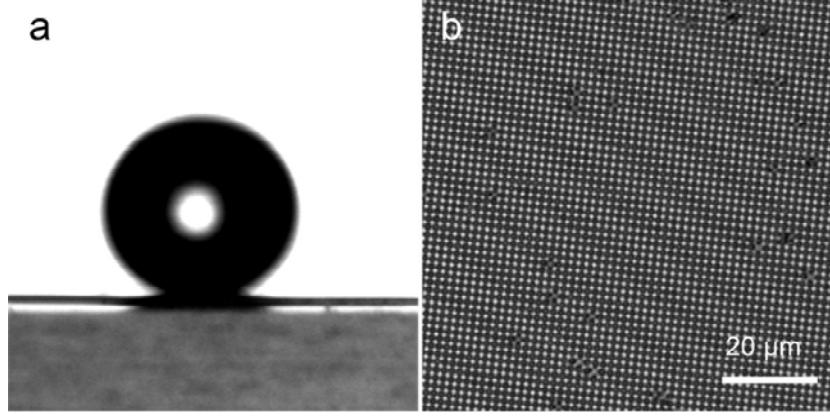


Figure 4.5 Stability and wettability of PEGDMA conical pillar array when exposed to water. (a) Optical image of water droplet on PEGDMA conical pillar array before and after soaking in water for 30 minutes and blow-dried, water contact angle of 159° . (b) Optical microscope image of the PEGDMA conical pillar array corresponding to (a) after soaking in water and blow-dried.

The wettability of structured polymers is dependent on both the surface topography and Young's contact angle on a flat substrate, θ_0 , as described by Cassie³² and Wenzel³³ models. The Cassie model assumes that the water droplet sits on the air-solid composite surface, and the Cassie contact angle is defined as

$$\cos \theta_c = f(\cos \theta_0 + 1) - 1 \quad (4.4)$$

where f is the fraction of solid area on the solid-air surface. The Wenzel model assumes that the liquid droplet wets completely between the grooves without trapped air. The Wenzel contact angle is defined as

$$\cos \theta_w = r \cos \theta_0 \quad (4.5)$$

where r is the surface roughness, i.e. the ratio of actual surface area to the geometrically projected surface area.

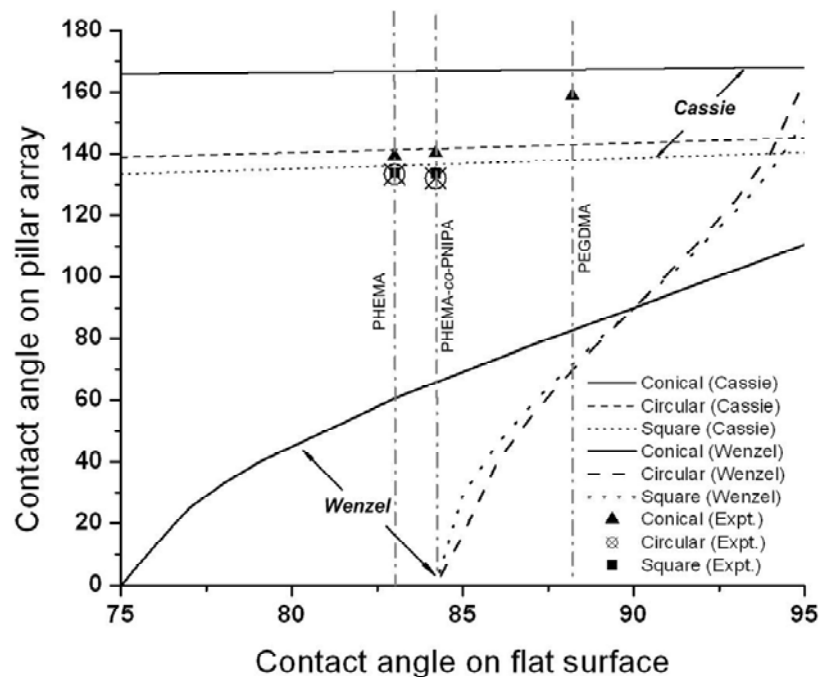


Figure 4.6 Comparison of measured water contact angles on the hydrogel pillar arrays vs. those predicted by Cassie and Wenzel models.

As seen in Fig. 4.6, the initial water contact angles on all hydrogel pillar arrays are close to the Cassie state, implying that the water droplet sits on the tips of pillars. However, we observed gradual decrease of the water contact angle from 140° (Fig. 4.4a) to 125° within 30 seconds of placing a water droplet on PHEMA-co-PNIPAA conical pillar array. It further decreased to less than 90° in approximately 10 min. The decrease in contact angle suggests gradual wetting and absorption of water by the pillars over time resulting in drastically reduced elastic modulus. When the PHEMA-co-PNIPAA conical pillar array was immersed in water for 15 min., followed by blow-drying, its water contact angle was significantly lowered to 83° (Fig. 4.4b), close to that on a flat PHEMA-

co-PNIPA surface, 84°. Given the observation that the pillars were all ground collapsed, it is reasonable that the contact angle on collapsed pillars is close to that on the flat surface. Thus, the ground collapse of PHEMA-*co*-PNIPA conical pillars can be attributed to drastically decreased Young's modulus (~5MPa) of the hydrogel in water which makes them susceptible to ground collapse due to adhesive forces (Table 4.1).

The surface of PEGDMA conical pillar array, on the other hand, was found superhydrophobic with a water contact angle of 159° (Fig. 4.5a). The water droplet readily rolled off the pillar array surface, and the water contact angle did not decrease even after the PEGDMA conical pillar array was immersed in water for 30 minutes. Since the water contact angle on a flat PEGDMA film, 88°, is not very different from that on a flat PHEMA-*co*-PNIPA film, 84°, the non-wettability and surface stability could be attributed to the high crosslinking density of PEGDMA, where EGDMA itself serves as both monomer and crosslinker. It has been shown that crosslinking could effectively increase the polymer film's mechanical robustness, thus, limiting water diffusion into the films and preventing surface reconstruction.³⁴ Thus, the stability of PEGDMA conical pillars in water can be explained by their non-wettability in water.

To further investigate the importance of wettability to pillar stability, we immersed the PEGDMA conical pillar array in ethanol, which has a lower surface energy, $\gamma_{ethanol} = 22.3$ mN/m, than water, $\gamma_{ethanol} = 72.0$ mN/m. Ethanol readily wets the PEGDMA surface with a Young's contact angle, $\theta_0 = 42^\circ$, however, it does not appear to swell the highly crosslinked PEGDMA to an appreciable extent. Ethanol was completely wetted on the PEGDMA conical pillar array, which agreed with the Wenzel model that surface roughness enhances wetting if the Young's contact angle is below 90° (Fig. 4.6).

After blow-dried in air, the PEGDMA conical pillar array was found randomly collapsed (Fig. 4.7a) and appeared white, whereas the micropillar array immersed in ethanol before drying showed multiple diffraction colors, suggesting the highly ordered, stable structure. Since, the micropillar arrays were stable while still immersed in ethanol, the collapsed structure after blow-drying should be attributed to capillary force exerted by the ethanol evaporation off the micropillar arrays during drying.

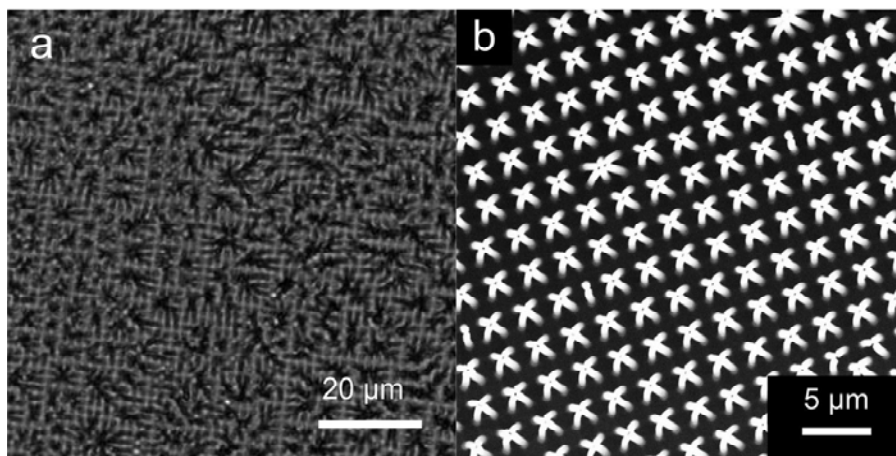


Figure 4.7 Images of different PEGDMA micropillar arrays after soaking in ethanol for 15 minutes followed by blow-drying. (a) Optical microscope image of conical pillar array ($d_{tip} = 350$ nm, $d_{base} = 750$ nm, $h = 7$ μm, and $w_{base} = 1.25$ μm) and (b) SEM image of circular pillar array ($d = 750$ nm, $h = 9$ μm, $w = 750$ nm).

Further, we demonstrated the effect of pillar array geometry on the capillary force induced collapsing behavior. When more densely packed, larger diameter PEGDMA circular pillars ($d = 750$ nm, $h = 9$ μm, $w = 750$ nm, pillar density of 4.4×10^7 pillars/cm²) were treated with ethanol, an interesting superstructure was observed: i.e. most of the pillars collapsed together in a group of four (Fig. 4.7b). The result is similar

to the observation reported by Segawa³⁵ et al. where the authors attributed the micropillar collapse to Laplace pressure difference due to curved liquid surface formed during drying of the liquid.

However, as we will show in the following Chapters, in case of 2-dimensional arrays of HAR micropillars, the collapsing is due to capillary meniscus interaction force³⁶ while the pillars are still surrounded by a continuous liquid body (i.e. no isolated capillary bridges) rather than due to often reported Laplace pressure difference.

4.4 Conclusions

Using replica molding, we successfully fabricated high density ($>10^7$ pillars/cm²), high-aspect-ratio (up to 12) hydrogel micropillar arrays from partially polymerized precursor solutions. The partial polymerization step was found critical to minimize the problems, including inhibition of polymerization by oxygen and permeation of monomer into the PDMS mold. Because of their high Young's modulus in the dry state, all hydrogel pillar arrays were highly stable in air. Exposure of the PHEMA-*co*-PNIPA conical pillar array to water caused gradual wetting and swelling of the pillars, which drastically decreased their Young's modulus. The drastic reduction in hydrogel stiffness led to ground collapse of these micropillars. In comparison, PEGDMA conical nanopillars maintained their stability without wetting or swelling by water. However, when immersed in ethanol, a much lower surface energy solvent than water, wetting occurred and the PEGDMA pillars collapsed after drying due to capillary force. Depending on the pillar array geometry and size, PEGDMA nanopillars collapsed either randomly in the case of conical pillars or form complex hierarchical structures in the case

of more densely packed circular pillars. We believe that our fabrication technique can be readily extended to other hydrogel systems, and the hydrogel composition and mechanical properties can be tailored for a wide range of applications, including ultrathin whitening³⁷, photonics, sensors, microfluidics, and tissue engineering.

Detailed study of the nature of the capillary force in micropillar arrays when immersed in a liquid, followed by evaporation of liquid, and the effect of micropillar elastic modulus on the clustering behavior will be presented in Chapters 5 and 6, respectively.

4.5 References

- (1) Ansari, K.; van Kan, J. A.; Bettiol, A. A.; Watt, F. *Appl. Phys. Lett.* **2004**, *85*, 476.
- (2) Kaji, N.; Tezuka, Y.; Takamura, Y.; Ueda, M.; Nishimoto, T.; Nakanishi, H.; Horiike, Y.; Baba, Y. *Anal. Chem.* **2004**, *76*, 15.
- (3) Krupenkin, T. N.; Taylor, J. A.; Schneider, T. M.; Yang, S. *Langmuir* **2004**, *20*, 3824.
- (4) Kuo, C. W.; Shiu, J. Y.; Chen, P. L. *Chem. Mater.* **2003**, *15*, 2917.
- (5) Tada, T.; Kanayama, T. *J. Vac. Sci. Technol. B* **1998**, *16*, 3934.
- (6) du Roure, O.; Saez, A.; Buguin, A.; Austin, R. H.; Chavrier, P.; Siberzan, P.; Ladoux, B. *Proc. Natl. Acad. Sci. U. S. A.* **2005**, *102*, 2390.
- (7) Geim, A. K.; Dubonos, S. V.; Grigorieva, I. V.; Novoselov, K. S.; Zhukov, A. A.; Shapoval, S. Y. *Nat. Mater.* **2003**, *2*, 461.
- (8) Glassmaker, N. J.; Jagota, A.; Hui, C.-Y.; Kim, J. *J. R. Soc. Interface* **2004**, *1*, 23.

- (9) Tan, J. L.; Tien, J.; Pirone, D. M.; Gray, D. S.; Bhadriraju, K.; Chen, C. S. *Proc. Natl. Acad. Sci. U. S. A.* **2003**, *100*, 1484.
- (10) van Kan, J. A.; Bettiol, A. A.; Watt, F. *Appl. Phys. Lett.* **2003**, *83*, 1629.
- (11) Zhang, Y.; Lo, C. W.; Taylor, J. A.; Yang, S. *Langmuir* **2006**, *22*, 8595.
- (12) Peppas, N. A.; Hilt, J. Z.; Khademhosseini, A.; Langer, R. *Adv. Mater.* **2006**, *18*, 1345.
- (13) Beebe, D. J.; Moore, J. S.; Bauer, J. M.; Yu, Q.; Liu, R. H.; Devadoss, C.; Jo, B. H. *Nature* **2000**, *404*, 588.
- (14) Bryant, S. J.; Hauch, K. D.; Ratner, B. D. *Macromolecules* **2006**, *39*, 4395.
- (15) Hahn, M. S.; Taite, L. J.; Moon, J. J.; Rowland, M. C.; Ruffino, K. A.; West, J. L. *Biomaterials* **2006**, *27*, 2519.
- (16) Revzin, A.; Tompkins, R. G.; Toner, M. *Langmuir* **2003**, *19*, 9855.
- (17) Fréchet, J. M. J. e. a.; Bergbreiter, D. E., Martin, C. R., Eds.; Plenum: New York, 1989, p 193.
- (18) Zhou, W. H.; Kuebler, S. M.; Braun, K. L.; Yu, T. Y.; Cammack, J. K.; Ober, C. K.; Perry, J. W.; Marder, S. R. *Science* **2002**, *296*, 1106.
- (19) Xia, Y. N.; Whitesides, G. M. *Annu. Rev. Mater. Sci.* **1998**, *28*, 153.
- (20) Yu, T. Y.; Ober, C. K. *Biomacromolecules* **2003**, *4*, 1126.
- (21) Di Benedetto, F.; Biasco, A.; Pisignano, D.; Cingolani, R. *Nanotechnology* **2005**, *16*, S165.
- (22) Koh, W. G.; Itle, L. J.; Pishko, M. V. *Anal. Chem.* **2003**, *75*, 5783.
- (23) Suh, K. Y.; Choi, S. J.; Baek, S. J.; Kim, T. W.; Langer, R. *Adv. Mater.* **2005**, *17*, 560.

- (24) Decker, C.; Jenkins, A. D. *Macromolecules* **1985**, *18*, 1241.
- (25) Hansel, C.; Leyhausen, G.; Mai, U. E. H.; Geurtsen, W. *J. Dent. Res.* **1998**, *77*, 60.
- (26) Roca-Cusachs, P.; Rico, F.; Martinez, E.; Toset, J.; Farre, R.; Navajas, D. *Langmuir* **2005**, *21*, 5542.
- (27) Abbasian, A.; Ghaffarian, S. R.; Mohammadi, M.; Fallahi, D. *J. Appl. Polym. Sci.* **2004**, *93*, 1972.
- (28) Barsoum, M. W.; Murugaiah, A.; Kalidindi, S. R.; Zhen, T.; Gogotsi, Y. *Carbon* **2004**, *42*, 1435.
- (29) Stoykovich, M. P.; Cao, H. B.; Yoshimoto, K.; Ocola, L. E.; Nealey, P. F. *Adv. Mater.* **2003**, *15*, 1180.
- (30) Davis, T. P.; Huglin, M. B. *Angew. Makromol. Chem.* **1991**, *189*, 195.
- (31) Wilder, E. A.; Guo, S.; Lin-Gibson, S.; Fasolka, M. J.; Stafford, C. M. *Macromolecules* **2006**, *39*, 4138.
- (32) Cassie, A. B. D.; Baxter, S. *Trans. Far. Soc.* **1944**, *40*, 546.
- (33) Wenzel, R. N. *Ind. Eng. Chem.* **1936**, *28*, 988.
- (34) Yang, S.; Wang, J.; Ogino, K.; Valiyaveetil, S.; Ober, C. K. *Chem. Mater.* **2000**, *12*, 33.
- (35) Segawa, H.; Yamaguchi, S.; Yamazaki, Y.; Yano, T.; Shibata, S.; Misawa, H. *Appl. Phys. A* **2006**, *83*, 447.
- (36) Kralchevsky, P. A.; Paunov, V. N.; Ivanov, I. B.; Nagayama, K. *J. Colloid Interface Sci.* **1992**, *151*, 79.
- (37) Vukusic, P.; Hallam, B.; Noyes, J. *Science* **2007**, *315*, 348.

Chapter 5

Nature of Capillary Force in 2D Arrays of Micropillars: Isolated Capillary Bridges or Lateral Capillary Meniscus Interaction Force?

As we have observed in the previous Chapter, when a wetting liquid is evaporated off a micropillar array surface, the pillars collapse (in some cases in an ordered fashion) due to the capillary force exerted by the evaporating liquid. However, as discussed in Chapter 2, the nature of the capillary force depends on the geometry of the system. In order to understand the clustering behavior of the micropillars due to capillary force, in this chapter we present experimental results and theoretical analysis to investigate the nature of the capillary force in 2-dimensional arrays of micropillars when a liquid is evaporated off their surface.

5.1 Introduction

With decreasing feature size and increasing aspect-ratio, the surface area to volume ratio of the HAR micropillars increases, resulting in dominant effect of surface forces, such as adhesion, friction, and capillary forces, which adversely impacts their mechanical stability. While the large surface area and increased mechanical compliance have lead to many key advantages of micropillar arrays for a wide range of applications, such as sensors¹, mechanical actuators², bio-mimetic dry adhesives^{3,4} and tunable wetting⁵, these properties also result in their increased susceptibility to deformation due

to adhesion^{6,7} and capillary forces.⁸⁻¹⁰ Recently, capillary force has also been harnessed to self-assemble hierarchical microstructures.^{8,11,12}

The phenomenon of capillary force is responsible for a wide range of macroscopic and microscopic observations, ranging from the rise of liquid in a capillary tube and clumping together of hair after shower to self-assembly of microparticles.¹³ In general, the capillary force is proportional to the liquid-vapor interfacial energy γ and results from the tendency of a system to minimize the sum of the three interfacial energies – liquid-vapor (γ), solid-vapor (γ_{sv}) and solid-liquid (γ_{sl}) – which are related to each other through Young's equation,

$$\gamma_{sv} - \gamma_{sl} - \gamma \cos \theta = 0 \quad (5.1)$$

where, θ is the equilibrium contact angle. However, the exact expression for the capillary force depends on the actual geometry of the system and gives rise to a range of phenomenon, such as distortion of photoresist patterns due to negative Laplace pressure of the capillary bridge^{14,15}, buckling of microfilaments due to liquid surface tension along the three phase contact line,¹⁶ coalescence of fibers driven by reduction in liquid-vapor surface area,^{17,18} and aggregation of particles partially immersed in or floating on a liquid surface due to lateral forces arising from capillary menisci interaction.¹³

Distortion of one-dimensional (1D) array of tall microstructures, when a liquid is evaporated off their surface, has been previously explained in terms of Laplace pressure difference due to isolated capillary bridges formed between the structures,^{14,15} and the same argument is often extended to explain the instability of two-dimensional (2D) arrays of high aspect-ratio structures^{9,12,19,20}. Occasionally, the collapsing behavior of 2D micropillar arrays has been attributed to lateral forces arising from interaction between

capillary menisci formed around the microstructures,²¹ and sometimes no distinction is made between these two approaches.²² Furthermore, justification for employing either of the two approaches has not been provided in the literature.

In this Chapter, we present experimental evidence to show that in case of 2D arrays of micropillars, when a liquid is evaporated off their surface, the clustering of the micropillars should be attributed to the lateral forces resulting from capillary menisci interaction rather than to Laplace pressure difference due to isolated capillary bridges. Simple theoretical arguments show that the capillary meniscus interaction force can be more than an order of magnitude smaller than that obtained by assuming Laplace pressure difference due to isolated capillary bridges. Consequently, the critical elastic modulus necessary for the stability of the micropillars is much smaller than that estimated by capillary bridge approach.

5.2 Experimental methods

We used short chain, monodisperse polystyrene (PS) melt ($M_n = 1.79$ kg/mol and PDI = 1.06, PSS Germany) as the wetting liquid on epoxy micropillar arrays (2D square lattice) to study their capillary induced collapsing behavior and to visualize the liquid morphology between the micropillars. The epoxy micropillar arrays were prepared by using poly(dimethyl siloxane) (PDMS) molds to replica mold a mixture of commercially available epoxy resin (DER 354, Dow Chemical) and 3 wt% cationic photoinitiator (Cycracure UVI 6976, Dow Chemical), followed by UV curing (~ 8.5 mW/cm²) for ~ 30 minutes. Two types of epoxy micropillar arrays were fabricated. Mechanically stable low aspect-ratio micropillar arrays (diameter 10 μ m, height 10 μ m and pitch 20 μ m) were used

to obtain wetting profile of the molten PS between the micropillars, and high aspect-ratio micropillar arrays (diameter $0.6\ \mu\text{m}$, height $4.8\ \mu\text{m}$ and pitch $1.5\ \mu\text{m}$) (Fig. 5.1a) were used to observe their collapsing behavior due to capillary force of the PS melt. The micropillar array was placed on a hot plate at 180°C with a few particles of PS powder sprinkled on the top. The PS quickly melted on the micropillar array and was left at 180°C for an hour for evaporation. The micropillar array was then cooled to room temperature to freeze the polystyrene for subsequent imaging by scanning electron microscope (SEM) (FEI Strata DB235) and atomic force microscope (Digital Instruments, Dimension 3000). Previous studies have shown that the morphology of PS remains identical before and after freezing.^{23,24}

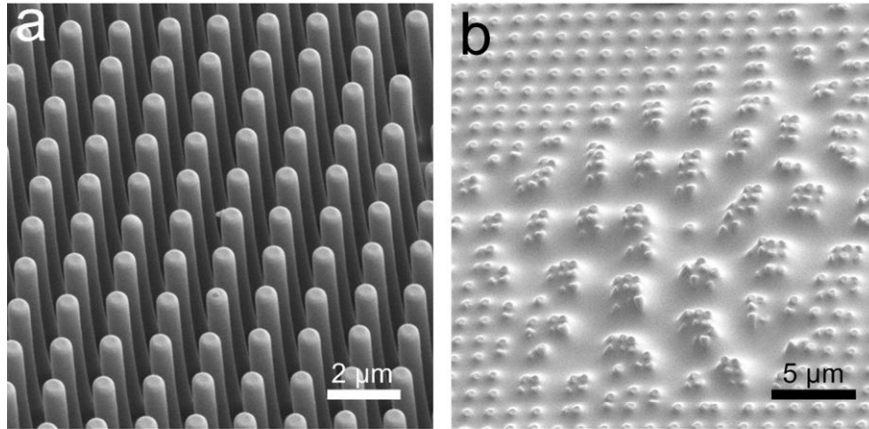


Figure 5.1 SEM images of epoxy micropillar arrays. (a) As fabricated and (b) collapsed by polystyrene melt.

5.3 Results and discussion

As seen in the SEM image in Fig. 5.1b, the micropillars collapsed while still completely surrounded by PS liquid. The absence of isolated capillary bridges between

the micropillars, and the fact that a continuous liquid body in mechanical equilibrium has a constant Laplace pressure everywhere,²⁵ indicate that Laplace pressure difference cannot explain the observed collapse of micropillars. It should be noted, however, that for 1D array of line patterns, Laplace pressure argument is applicable because in that geometry isolated liquid between the lines could exist, resulting in different Laplace pressures.

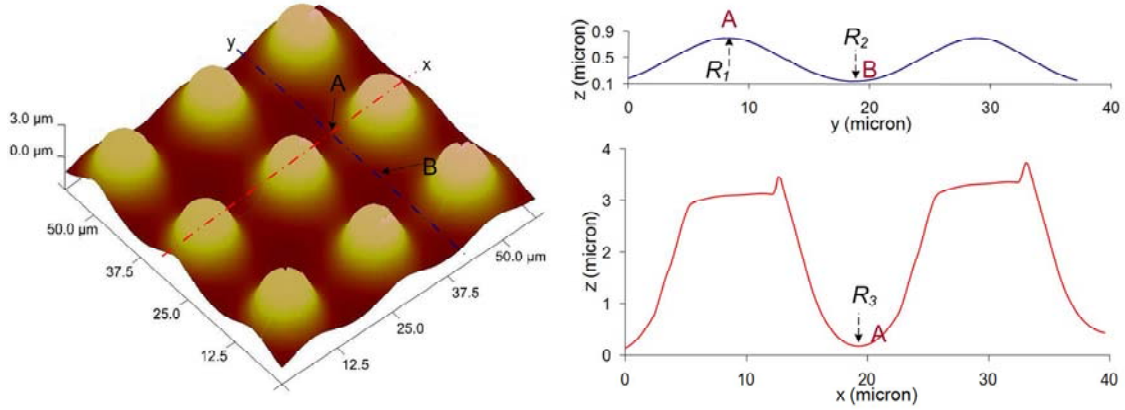


Figure 5.2 AFM scan of polystyrene wetting morphology in epoxy micropillar arrays.

The mean curvature at two representative points, A and B is the same.

Atomic force microscopy (AFM) imaging of polystyrene frozen in a mechanically stable, low-aspect-ratio micropillar array (Fig. 5.2) further confirms that the mean curvature, and thus the Laplace pressure in the liquid surrounding the micropillars, is constant everywhere. For example, in Fig. 5.2, mean curvature at point A between adjacent pillars, $(R_1^{-1} - R_3^{-1})/2$ is equal to $-R_2^{-1}$, the mean curvature at point B between diagonally opposite pillars. However, even in absence of Laplace pressure variation, when two particles are partially immersed in a liquid or float on a liquid interface they experience a lateral capillary meniscus interaction force,²⁶ which can be either attractive

(when the particles are both hydrophobic or both hydrophilic) or repulsive (when the particles have opposite wettabilities). This lateral force arises because of the deformation of the otherwise flat liquid surface due to presence of the particles. Based on the equations given by Kralchevsky et al.²⁷, an expression (see section 5.6 for derivation) for the capillary interaction energy, W_c of two cylinders (Fig. 5.3a) when partially immersed in a liquid of surface tension γ with a contact angle θ ,

$$W_c = 2\pi\gamma R^2 \cos^2 \theta \ln \left(\frac{x + \sqrt{x^2 - 4R^2}}{l_c} \right) \quad (5.2)$$

Here, l_c is the capillary length of the liquid and R and x are as defined in Figure 5.3a.

Thus, the capillary force between the cylinders is,

$$F_c = -\frac{\partial W_c}{\partial x} = -\frac{\pi\gamma R^2 \cos^2 \theta}{\sqrt{(x/2)^2 - R^2}} \quad (5.3)$$

In case of micropillars, where one end is fixed on the substrate, the torque τ_c on the micropillars due to the F_c is,

$$\tau_c = \frac{\pi\gamma R^2 h \cos^2 \theta}{\sqrt{(x/2)^2 - R^2}} \quad (5.4)$$

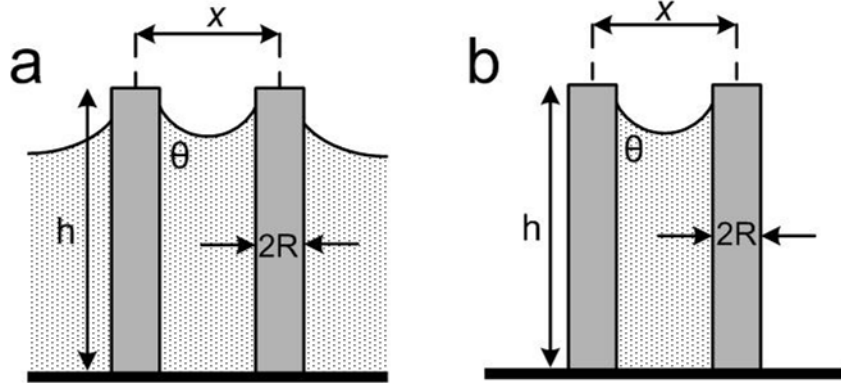


Figure 5.3 Schematic illustrations of two micropillars (a) partially immersed in a liquid and (b) with an isolated capillary bridge between them.

For the same geometry, in case of isolated capillary bridge between the micropillars (Fig.

5.3b), the Laplace pressure difference is approximately $P_l \approx \frac{\gamma \cos \theta}{\frac{x}{2} - R}$, and thus the torque

on the micropillars is,

$$\tau_l \approx \frac{2R\gamma \cos \theta}{\frac{x}{2} - R} \int (h) dh = \frac{\gamma R h^2 \cos \theta}{\frac{x}{2} - R} \quad (5.5)$$

The ratio of the torques calculated by two approaches is,

$$\frac{\tau_l}{\tau_c} \approx \frac{h}{\pi R \cos \theta} \sqrt{\frac{\frac{x}{2} + R}{\frac{x}{2} - R}} \quad (5.6)$$

Thus, according to Eq. 5.6, for a typical case of $\theta = 60^\circ$ and aspect ratio of 10, the torque in case of isolated capillary bridge is at least 12 times greater than that from lateral capillary meniscus interaction.

The large difference in the torques calculated from the two approaches is reflected in a large difference in the critical elastic modulus for the stability of micropillar arrays when estimated from the two approaches. The critical modulus calculated from the

capillary meniscus interaction approach is significantly smaller than that calculated from isolated capillary bridge approach. It has been observed by us (see Chapter 6) and others that in case of micropillars arranged in a square lattice, the collapsing due to evaporation of a liquid initiates by groups of 4 neighboring pillars clustering together.^{11,21,28} Thus, in a simple model we consider 4 pillars on the corners of a square as shown in Fig. 5.4a-inset. Let the pillars come together by deflection δ in both directions. In this configuration, assuming superposition of pairwise interaction between micropillars, the capillary meniscus interaction force F_C acting on a micropillar is given by

$$F_C = \frac{\pi\gamma d^2 \cos^2 \theta}{2} \left(\sqrt{\frac{2}{(p-2\delta)^2 - d^2}} + \sqrt{\frac{1}{2(p-2\delta)^2 - d^2}} \right) \quad (5.7)$$

The elastic restoring force acting on the deflected pillar is given as,²⁹

$$F_E = \frac{3\sqrt{2}\pi E d^4 \delta}{64h^3} \quad (5.8)$$

The critical modulus for stability, E_{crit} , can be obtained when $F_E \geq F_C$. A typical plot of F_C and F_E (Fig. 5.4a) shows that this condition is satisfied for some critical deflection δ_c , when the curve for F_E is at least tangential to the curve for F_C . Thus, the value of δ_c is obtained by solving $\frac{dF_C}{d\delta} = \frac{F_C}{\delta}$ in terms of δ . Putting the value of δ_c back into Eqs. 5.7

and 5.8 and then solving $F_E = F_C$ in terms of E gives E_{crit} as,

$$E_{crit} = \frac{32\sqrt{2}\gamma \cos^2 \theta h^3}{3d^4} f(r) \quad (5.9)$$

where, $f(r)$ is a function of $r = p/d$ and plotted in Fig. 5.4b:

$$f(r) = \frac{1}{r-k} \left(\sqrt{\frac{2}{k^2-1}} + \sqrt{\frac{1}{2k^2-1}} \right) \quad (5.10a)$$

$$r = 1/k \left(\frac{\sqrt{2}(k^2 - 1)^{-1/2} + (2k^2 - 1)^{-1/2}}{\sqrt{2}(k^2 - 1)^{-3/2} + 2(2k^2 - 1)^{-3/2}} \right) + k \quad (5.10b)$$

It should be noted that E_{crit} is the minimum modulus below which micropillars will always be unstable ($F_C > F_E$) for all deflection values δ . For stable pillars, the elastic modulus E should be considerably greater than E_{crit} such that $F_E > F_C$ is maintained over a reasonable range of deflection δ_1 (stable equilibrium) to δ_2 (unstable equilibrium) (Fig. 5.4a). Since the capillary force between the micropillars (Eqs. 5.3 and 5.7) diverges as the micropillar separation tends to zero, the model predicts that regardless of the value of elastic modulus E , for deflection values more than δ_2 , $F_C > F_E$. In practical situations though, in absence of other external forces which may cause the micropillars to deflect beyond δ_2 to start with, stability can be ensured if $F_E > F_C$ is maintained over a reasonable range of deflection, δ_1 to δ_2 .

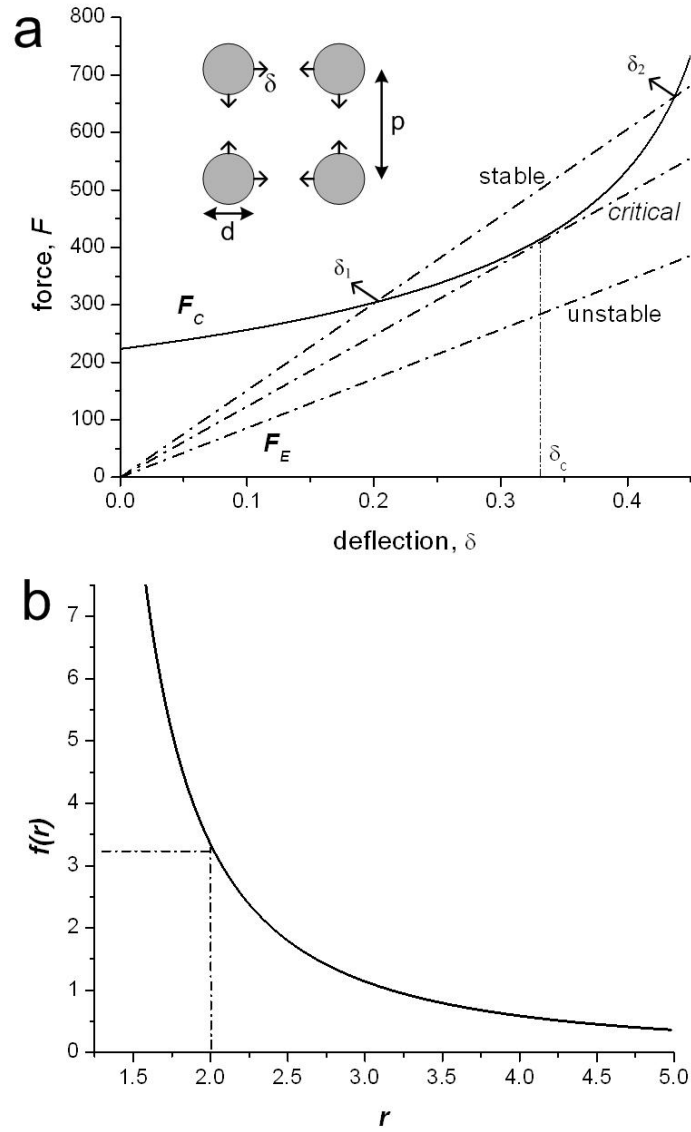


Figure 5.4 (a) A typical plot of capillary interaction force, F_C , (solid line) and elastic restoring force acting on the deflected pillar, F_E , (dashed lines). δ_1 and δ_2 represent stable equilibrium and unstable equilibrium, respectively. Inset: schematic illustration of interaction between a group of four pillars. Increasing slope of F_E corresponds to increasing elastic modulus E . (b) Function $f(r)$ as a function of $r = p/d$. The dashed line indicates the value of the function at $r = 2$.

As an example, in case of circular micropillar arrays of Chapter 4 (height $9\mu\text{m}$, diameter $0.75\mu\text{m}$, pitch $1.5\mu\text{m}$), and assuming a contact angle $\theta = 60^\circ$, From Eq. 5.9, the E_{crit} is calculated as 2 GPa. In comparison, for the same geometry, the critical elastic modulus, E'_{crit} , in case of Laplace pressure difference due to isolated capillary bridge between the four pillars is given by^{8,15},

$$E'_{crit} = \frac{128\gamma h^3 \left(3h \cos \theta + w \sin \theta + \sqrt{9h^2 \cos^2 \theta + 3hw \sin(2\theta)} \right)}{3\pi d^3 w^2} \quad (5.11)$$

Here, $w = \sqrt{2}p - d$ is the spacing between the diagonally opposite micropillars. From Eq. 5.11, E'_{crit} is calculated as 27 GPa, which is much greater than that obtained by Eq. 5.9. As we will show in the next Chapter, critical modulus values estimated from Eq. 5.9 based on capillary meniscus interaction force are close to the experimentally suggested values whereas, Eq. 5.11 based on isolated capillary bridge grossly underestimates the stability of the micropillars.

It must be pointed out though, that in later stages of liquid evaporation, there may no longer be a continuous liquid body surrounding the micropillars and isolated capillary bridges may likely form. However, such isolated capillary bridges will be near the base of the micropillars and thus will exert much less torque as compared to a capillary bridge spanning the whole micropillar length.

5.4 Conclusions

In conclusion, we have investigated the capillary force responsible for the collapsing of 2D arrays of tall microstructures upon liquid evaporation. Experimental

evidence suggests that the capillary meniscus interaction force is mainly responsible to the pillar collapse rather than the often cited Laplace pressure difference due to isolated capillary bridges. Our quantitative analysis shows that for a given geometry, the capillary meniscus interaction force exerted on micropillar array is much smaller than the force due to isolated capillary bridge; therefore, a much smaller critical elastic modulus is required for the stability of the microstructures. The analysis presented here will be important for rational design of stable arrays of tall microstructures or for harnessing their instability for various applications^{11,28}.

5.5 References

- (1) du Roure, O.; Saez, A.; Buguin, A.; Austin, R. H.; Chavrier, P.; Siberzan, P.; Ladoux, B. *Proc. Natl. Acad. Sci. U. S. A.* **2005**, *102*, 2390-2395.
- (2) Evans, B. A.; Shields, A. R.; Carroll, R. L.; Washburn, S.; Falvo, M. R.; Superfine, R. *Nano Lett.* **2007**, *7*, 1428-1434.
- (3) Geim, A. K.; Dubonos, S. V.; Grigorieva, I. V.; Novoselov, K. S.; Zhukov, A. A.; Shapoval, S. Y. *Nat. Mater.* **2003**, *2*, 461-463.
- (4) Sethi, S.; Ge, L.; Ci, L.; Ajayan, P. M.; Dhinojwala, A. *Nano Lett.* **2008**, *8*, 822-825.
- (5) Krupenkin, T. N.; Taylor, J. A.; Schneider, T. M.; Yang, S. *Langmuir* **2004**, *20*, 3824-3827.
- (6) Hui, C. Y.; Jagota, A.; Lin, Y. Y.; Kramer, E. J. *Langmuir* **2002**, *18*, 1394-1407.
- (7) Zhang, Y.; Lo, C. W.; Taylor, J. A.; Yang, S. *Langmuir* **2006**, *22*, 8595-8601.
- (8) Chandra, D.; Taylor, J. A.; Yang, S. *Soft Matter* **2008**, *4*, 979.

- (9) del Campo, A.; Greiner, C. *Journal of Micromechanics and Microengineering* **2007**, *17*, R81-R95.
- (10) Kotera, M.; Ochiai, N. *Microelectron. Eng.* **2005**, *78-79*, 515-520.
- (11) Pokroy, B.; Kang, S. H.; Mahadevan, L.; Aizenberg, J. *Science* **2009**, *323*, 237-240.
- (12) Segawa, H.; Yamaguchi, S.; Yamazaki, Y.; Yano, T.; Shibata, S.; Misawa, H. *Appl. Phys. A* **2006**, *83*, 447.
- (13) Denkov, N. D.; Veleev, O. D.; Kralchevsky, P. A.; Ivanov, I. B.; Yoshimura, H.; Nagayama, K. *Langmuir* **1992**, *8*, 3183-3190.
- (14) Stoykovich, M. P.; Cao, H. B.; Yoshimoto, K.; Ocola, L. E.; Nealey, P. F. *Adv. Mater.* **2003**, *15*, 1180-1184.
- (15) Tanaka, T.; Morigami, M.; Atoda, N. *Jpn. J. Appl. Phys.* **1993**, *32*, 6059-6064.
- (16) Cohen, A. E.; Mahadevan, L. *Proc. Natl. Acad. Sci. U. S. A.* **2003**, *100*, 12141.
- (17) Bico, J.; Roman, B.; Moulin, L.; Boudaoud, A. *Nature* **2004**, *432*, 690.
- (18) Py, C.; Bastien, R.; Bico, J.; Roman, B.; Boudaoud, A. *Europhys. Lett.* **2007**, *77*, 44005.
- (19) Chakrapani, N.; Wei, B.; Carrillo, A.; Ajayan, P. M.; Kane, R. S. *Proc. Natl. Acad. Sci. U. S. A.* **2004**, *101*, 4009.
- (20) Lee, T. W.; Mitrofanov, O.; Hsu, J. W. R. *Advanced Functional Materials* **2005**, *15*, 1683-1688.
- (21) Zhao, Y. P.; Fan, J. G. *Appl. Phys. Lett.* **2006**, *88*, 103123.
- (22) Fan, J. G.; Dyer, D.; Zhang, G.; Zhao, Y. P. *Nano Lett.* **2004**, *4*, 2133.

- (23) Seemann, R.; Brinkmann, M.; Kramer, E. J.; Lange, F. F.; Lipowsky, R. *Proc. Natl. Acad. Sci. U. S. A.* **2005**, *102*, 1848.
- (24) Seemann, R.; Herminghaus, S.; Jacobs, K. *Phys. Rev. Lett.* **2001**, *87*, 196101.
- (25) de Gennes, P. G.; Brochard-Wayrt, F.; Quere, D. *Capillarity and Wetting Phenomena*; Springer 2004.
- (26) Kralchevsky, P. A.; Nagayama, K. *Particles at fluid interfaces and membranes*; Elsevier Science, 2001.
- (27) Kralchevsky, P. A.; Paunov, V. N.; Ivanov, I. B.; Nagayama, K. *J. Colloid Interface Sci.* **1992**, *151*, 79.
- (28) Chandra, D.; Yang, S.; Soshinsky, A.; Gambogi, R. *submitted* **2009**.
- (29) Beer, F. B.; Johnston, E. R. *Mechanics of Materials*; Mc Graw-Hill, 1992.

5.6 Appendix: Derivation of Equation 5.2

According to Kralchevsky²⁷ et al., the capillary meniscus interaction energy, W_c of two cylinders of radius R and separated by center-to-center distance x , partially immersed in a liquid of surface tension γ and making a contact angle θ (Fig. 5.3a) is given as,

$$W_c = -2\pi\gamma R \cos\theta (h_c - h_\infty) \quad (\text{A1})$$

where,

$$h_c = R \cos\theta \left[\tau + 2 \ln \left(\frac{1 - e^{-2\tau}}{\gamma_e q a} \right) \right] \quad (\text{A2})$$

and,

$$h_{\infty} = R \cos \theta \ln \left(\frac{4}{\gamma_e q R (1 + \sin \theta)} \right) \quad (\text{A3})$$

In the above equations,

$$\tau = \ln \left(\frac{a}{R} + \sqrt{1 + \frac{a^2}{R^2}} \right) \quad (\text{A4})$$

where,

$$a = \sqrt{s^2 - R^2} \quad (\text{A5})$$

where,

$$s = \frac{x}{2} \quad (\text{A6}),$$

γ_e is the Euler-Macaroni number ($\gamma_e = 1.78107$) and $1/q$ is the capillary length given as,

$$\frac{1}{q} = l_c = \left(\frac{\gamma}{\rho g} \right)^{1/2} \quad (\text{A7})$$

where,

ρ is the density of the liquid and g is the gravitational acceleration.

Substituting the value of a^2 from Eq. A5 into Eq. A4, we get,

$$\tau = \ln \left(\frac{a+s}{R} \right) \quad (\text{A8})$$

Thus, from Eq. A8,

$$1 - e^{-2\tau} = 1 - \frac{R^2}{(a+s)^2} = \frac{a^2 + s^2 - R^2 + 2as}{(a+s)^2} \quad (\text{A9})$$

Substituting $s^2 - R^2 = a^2$ from Eq. A5 into Eq. A9,

$$1 - e^{-2\tau} = \frac{2a^2 + 2as}{(a+s)^2} = \frac{2a}{a+s} \quad (\text{A10})$$

Using Eqs. A8 and A10 in Eq. A2, we get,

$$h_c = R \cos \theta \left[\ln \left(\frac{a+s}{R} \right) + 2 \ln \left(\frac{2}{\gamma_e q (a+s)} \right) \right] = R \cos \theta \ln \left(\frac{4}{\gamma_e^2 q^2 R (a+s)} \right) \quad (\text{A11})$$

Substituting the values of h_∞ and h_c from Eqs. A3 and A11 into Eq. A1,

$$W_c = -2\pi\gamma R^2 \cos^2 \theta \left[\ln \left(\frac{4}{\gamma_e^2 q^2 R (a+s)} \right) - \ln \left(\frac{4}{\gamma_e q R (1+\sin \theta)} \right) \right] \quad (\text{A12})$$

Rearranging Eq. A12 and substituting the value of q from Eq. A7,

$$W_c = -2\pi\gamma R^2 \cos^2 \theta \ln \left(\frac{l_c (1+\sin \theta)}{\gamma_e (a+s)} \right) \quad (\text{A13})$$

Using Eqs. A5 and A6,

$$a+s = \frac{x + \sqrt{x^2 - 4R^2}}{2} \quad (\text{A14})$$

Substituting the value of $a+s$ from Eq. A14 into Eq. A13, we get,

$$W_c = -2\pi\gamma R^2 \cos^2 \theta \ln \left(\frac{l_c}{x + \sqrt{x^2 - 4R^2}} \right) + 2\pi\gamma R^2 \cos^2 \theta \ln \left(\frac{\gamma_e}{2(1+\sin \theta)} \right) \quad (\text{A15})$$

In the above Eq. A15, the second term in the right hand side is a constant (does not depend on distance x) for a given system. Since the interaction potential energies can be defined only up to a constant, the constant term in Eq. A15 can be dropped to get,

$$W_c = -2\pi\gamma R^2 \cos^2 \theta \ln \left(\frac{l_c}{x + \sqrt{x^2 - 4R^2}} \right) \quad (\text{A16})$$

The above Eq. A16 for the capillary meniscus interaction energy is same as Eq. 5.2.

Chapter 6

Capillary Force Induced Clustering Behavior of HAR Micropillar Arrays

In the previous Chapter we established the nature of capillary force in 2-dimensional arrays of HAR micropillar arrays and derived an expression to estimate the critical elastic modulus required for stability against the capillary force. In this Chapter, we study the clustering behavior of micropillar arrays as a function of their elastic moduli and compare the critical elastic modulus as estimated from Chapter 5 to the experimentally suggested values. We then present the utility of randomly collapsed micropillar arrays for ultrathin whiteness.

6.1 Introduction

Many of the applications of high aspect-ratio micropillar arrays, such as tunable wetting¹, living cell studies^{2,3} and filtration and separation⁴, require them to be used in a liquid environment. However, in liquid environment, due to their large mechanical compliance, the micropillars are susceptible to deformation by capillary force exerted during liquid evaporation and cluster together⁵⁻⁷. On the other hand, the capillary force has been utilized to for example, form carbon nanotube foams⁸ and self-assemble superstructures.^{5,9,10} One important question is whether we can predict the clustering behavior of high-aspect-ratio pillars due to capillary force, which will be important to the utilization of capillary driven self-assembly process.

In this Chapter, we present theoretical and experimental study of the clustering behavior of hydrogel micropillar arrays with well-defined geometries induced by capillary force, and their utility as biomimetic ultrathin whitening layers. The hydrogel micropillar arrays were fabricated by the two-step replica molding method described in Chapter 4 from a series of monomer mixtures. By varying the composition of the water swellable 2-hydroxyethylmethacrylate (HEMA) component versus the glassy, non-swallowable methyl methacrylate (PMMA) as the micropillar material, we systematically modulated the effective elastic modulus of the micropillars from poly(2-hydroxymethacrylate-*co*-methyl methacrylate) (HEMA-*co*-PMMA) in the wet state over three orders of magnitude. The ability to tune the elastic modulus of the micropillars over a wide range allowed us to experimentally study the effect of elastic modulus on clustering. Clustering of macroscopic fibers when withdrawn from a liquid bath has been studied previously in terms of balance between elastic bending energy and capillary energy.^{11,12} It is important to point out that in these studies the capillary energy due to clustering originated from reduction in liquid-vapor surface area along a part of fiber length withdrawn from the liquid. However, as discussed in Chapter 5, in the case of micropillar clustering during liquid evaporation, the relevant capillary energy is the interaction energy of the liquid menisci¹³ surrounding the micropillars which are still immersed in the liquid except at the tip (Fig. 3a-ii), and few have systematically investigated micropillar clustering by considering meniscus interaction energy. Here, by minimizing the sum of capillary meniscus interaction energy and the elastic bending energy of the micropillars, we quantitatively predicted the average cluster size as a function of elastic modulus of the pillar materials, which agreed well with the

experimental observation. Further, we demonstrated that such random clustering of micropillar arrays could be utilized to design ultrathin whitening layers, mimicking the whiteness in ultrathin white beetle scales.¹⁴

6.2 Experimental methods

6.2.1 Materials

HEMA (98%) and MMA (99%) monomers were obtained from Aldrich and Acros Organics, respectively. Crosslinker, ethylene glycol dimethacrylate (EGDMA) (98%) was obtained from Alfa Aesar. Photoinitiator, Darocur 1173, was obtained from Ciba Specialty Chemicals Inc. PDMS precursor and curing agent (Sylgard 184) was obtained from Dow Corning. All the chemicals were used without further purification.

6.2.2 Fabrication of micropillar arrays

The micropillar arrays were fabricated by two-step replica molding process as described in Chapter 4. Two types of micropillar arrays were investigated, including geometry A (pillar diameter of 0.75 μm and pitch of 1.5 μm), and geometry B (pillar diameter of 1 μm and pitch of 2 μm), both of which were 9 μm tall. In a typical procedure, 2.5 mL monomer mixture of HEMA and MMA was mixed with 75 μL Darocur 1173 and exposed to UV light (UVP Blak-Ray, $\sim 8 \text{ mW/cm}^2$) for 2 minutes (5 minutes for MMA $\geq 60 \text{ wt } \%$) to obtain a viscous partially polymerized precursor solution. Before molding, additional 50 μL Darocur 1173 and 25 μL EGDMA were added to this solution to prepare the molding precursor. PDMS molds were prepared by mixing PDMS precursor and curing agent in a 10:1 ratio by weight and pouring it on silicon micropillar arrays master followed by curing at 65 $^{\circ}\text{C}$ for 4 hours. The cured molds were then carefully

peeled off the silicon master. To fabricate the hydrogel micropillar arrays the molding solution was cast on a silicon wafer and the PDMS mold was pressed over it, followed by UV exposure by a 97435 Oriel Flood Exposure Source (Newport Corporation) at a dose of 7200 mJ/cm². To collapse the micropillars to form clusters, the micropillar arrays were soaked in water for 10 minutes followed by drying in air stream.

6.2.3 Average cluster size determination

Clustered micropillar arrays were imaged by scanning electron microscope (SEM) (FEI Strata DB235 Focused Ion Beam) at acceleration voltage of 5kV and spot size 3. The samples were sputter coated with platinum before imaging. The cluster size was determined by manually counting the number of pillars in individual clusters and reported as average and standard deviation for all clusters in an area of 0.02 mm² from SEM images.

6.2.4 Water contact angle measurement

Static contact angles on flat PHEMA-*co*-PMMA films were measured using Ramé-Hart goniometer with DROPImage Advanced software. Reported values were averaged over at least 5 different spots. Water drops used were ~1.5 μ L in volume.

6.2.5 Elastic modulus measurement

Elastic moduli of wet PHEMA-*co*-PMMA films were measured by atomic force microscope (AFM) nanoindentation¹⁵⁻¹⁷ under water in a fluid cell using Digital Instruments Multimode AFM. The indentation force curves (cantilever deflection d vs. piezo displacement z , see a typical curve in Fig. 6.1a) were analyzed by a method outlined by Domke and Radmacher.¹⁶ Zero deflection point d_0 of the cantilever was

determined from the non-contact part of the force curve (Fig. 6.1a). The force applied by the cantilever tip on the film is

$$F = k(d - d_0) \quad (6.1)$$

where k is the spring constant of the cantilever which was determined by the resonant frequency method as described by Sader et al.¹⁸ Two types of cantilevers were used: soft cantilevers ($k \approx 0.1$ N/m) for soft samples with MMA content ≤ 25 wt% and stiffer cantilevers ($k \approx 20$ N/m) for samples with higher MMA content. Indentation depth is defined by $\delta = (z - z_0) - (d - d_0)$, where z_0 is the contact point (Fig. 6.1a). According to

conical tip approximation, the relation between indentation δ and force F is given as,^{16,19}

$$F = (2/\pi) \left[E / (1 - \nu^2) \right] \delta^2 \tan \alpha \quad (6.2)$$

where E is the elastic modulus, ν is the Poisson's ratio (here assumed to be 0.5^{16,17}), and α is the half opening angle of the cantilever tip, which was determined as 18° from SEM imaging. From Eq. 6.1 and 6.2,

$$(z - d) = (z_0 - d_0) + (d - d_0)^{1/2} \sqrt{\frac{\pi k (1 - \nu^2)}{2E \tan \alpha}} \quad (6.3)$$

Eq. 6.3 suggests a linear relation between $(z - d)$ and $(d - d_0)^{1/2}$. Therefore, the elastic modulus E was determined from the slope of $(z - d)$ vs. $(d - d_0)^{1/2}$ (Fig. 6.1b). The reported elastic moduli represent average over indentations at 3 to 7 different spots for each sample.

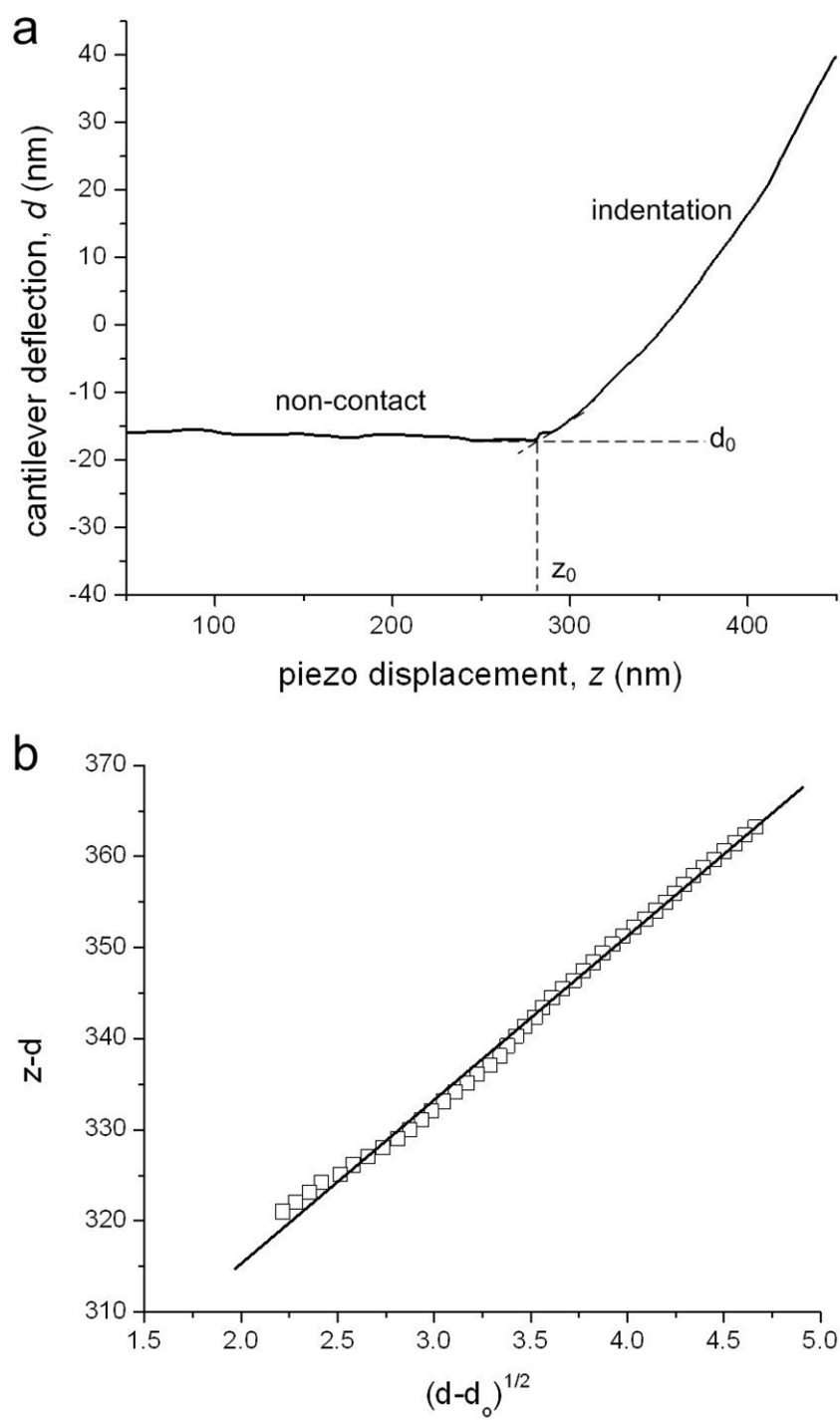


Figure 6.1 (a) An indentation force curve for 60 wt% MMA sample and (b) the corresponding $(z-d)$ vs. $(d-d_0)^{1/2}$ plot.

6.2.6 Whiteness characterization

Whiteness of the clustered micropillar arrays were characterized by measuring their CIE lightness index, L ,²⁰ using a photospectrometer (MHT Spectro Shade Micro). L represents diffuse reflectance of a surface on a scale from 0 to 100 where 0 is black and 100 is perfect white. The reported data represent average lightness index for 3 different samples with a small (less than 1) standard deviation.

6.3 Results and discussion

6.3.1 Micropillar clustering by capillary force

Two types of hydrogel micropillar arrays were fabricated by replica molding of partially polymerized copolymer precursors from HEMA and MMA, followed by photocrosslinking (see details in Experimental methods). The micropillar arrays were then soaked in water and dried in stream of air to collapse the pillars to include clustering (Fig. 6.2). Since poly(methyl methacrylate) (PMMA) is a glassy polymer ($T_g \sim 100^\circ\text{C}$) and does not absorb water, whereas poly(2-hydroxyethylmethacrylate) (PHEMA) does, we can systematically vary the composition of HEMA and MMA in the molding precursor, thus, controlling the degree of hydration and the effective elastic modulus of the micropillars in the wet state (Fig. 6.3a). As shown in Fig. 6.2 the micropillar cluster size decreases with increasing PMMA content and thus increasing elastic modulus (Fig. 6.3a). For a given PMMA content, the cluster size from type A micropillar array was typically larger than that from type B since A has smaller pillar diameter ($0.75\mu\text{m}$) and

higher aspect ratio (12) vs. those of B (pillar diameter of $1\mu\text{m}$ and aspect ratio of 9, respectively).

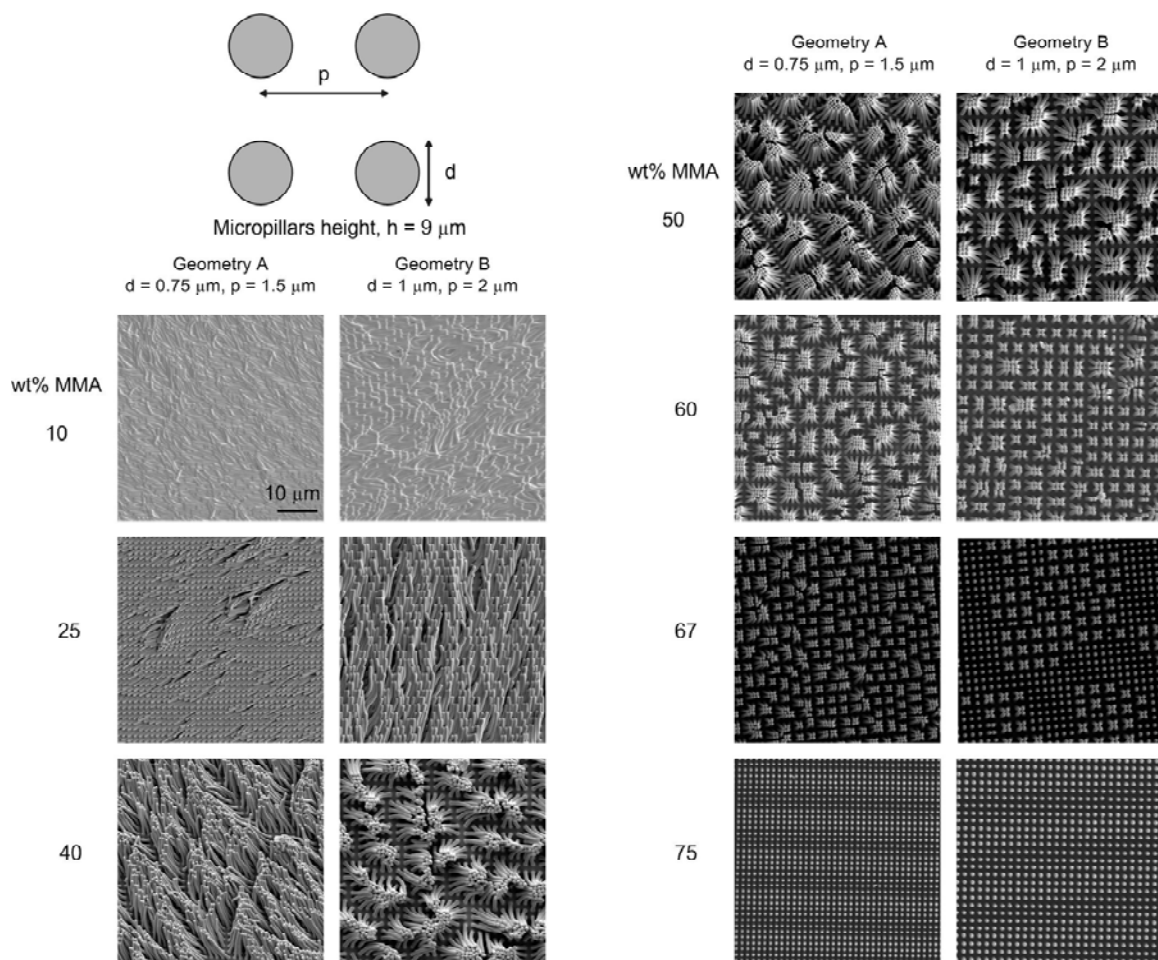


Figure 6.2 SEM images of $9\mu\text{m}$ tall PHEMA-*co*-PMMA micropillar arrays clustered by water capillary force.

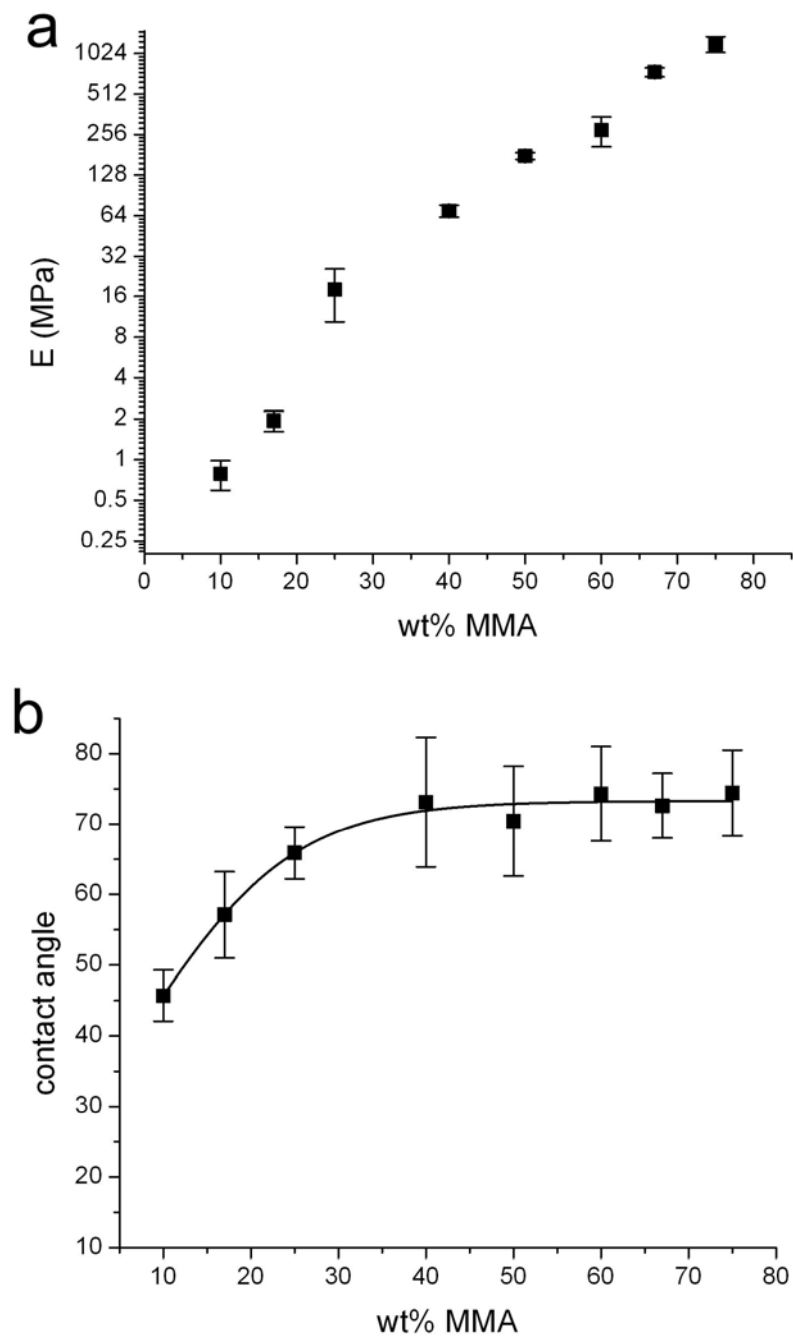


Figure 6.3 Elastic modulus in wet state (a) and the water contact angle (b) of flat PHEMA-*co*-PMMA films as a function of MMA content.

When the micropillar arrays are soaked in water, the pillars soften due to water absorbed by PHEMA resulting in a smaller effective elastic modulus in wet state which is dependent on relative composition of PHEMA and PMMA. Soaking bulk samples of same compositions in water reveal that there is no observable volume change in the samples. While drying the micropillar arrays soaked in water (Fig. 6.4a-i) in air flow, liquid menisci are formed around the individual pillars (Fig. 6.4a-ii). The interaction between these liquid menisci exerts an attractive force¹³ between the micropillars causing them to cluster together while still surrounded by water (Fig. 6.4a-iii). Due to elastoplastic nature of the crosslinked polymers, the deformation becomes permanent even after the water is completely dried (Fig. 6.4a-iv). For very low PMMA content (< 25 wt%), the micropillars are very soft (Fig. 6.3a) resulting in ground-collapse²¹ of micropillars due to gravity as the main reason for collapse (Fig. 6.2).

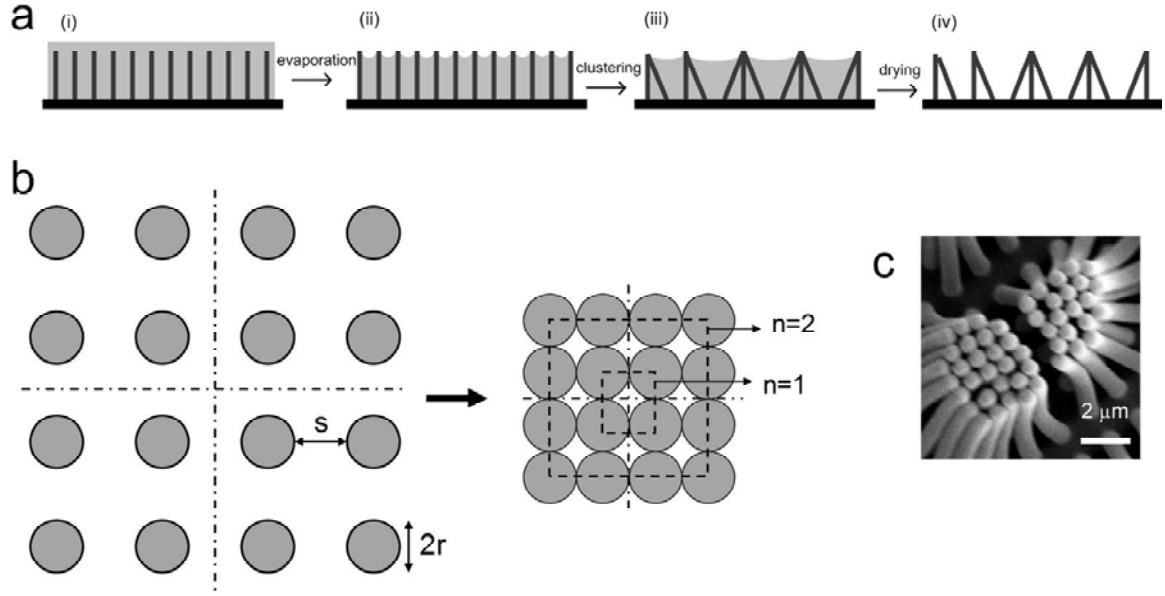


Figure 6.4 (a) Schematic illustration of micropillar clustering process due to capillary meniscus interaction force. (b) Schematic illustration of micropillar array clustering in a square lattice. (c) SEM image of micropillars clustered in a square lattice.

6.3.2 Calculation of cluster size

The effect of elastic modulus on the cluster size can be understood in terms of balance between capillary energy and elastic bending energy of a cluster. When the micropillar array is exposed to a wetting liquid, followed by liquid evaporation, the capillary meniscus interaction force of the liquid menisci surrounding the micropillars will pull the micropillars to collapse into clusters. Because the bases of the pillars are attached to the substrate, the pillars have to bend, which increases the elastic bending energy of the cluster. As the pillars come closer together the capillary meniscus interaction energy of the cluster decreases. The maximum number of pillars in a cluster is the result from the competition between the total bending energy and the total capillary

energy of the cluster. Qualitatively, in a cluster, the outer pillars have to bend more than the inner pillars. As shown later, this causes the positive bending energy to scale roughly as N^2 , where N is the number of pillars in a cluster. However, the decrease in capillary energy per pillar in a cluster is the same for all pillars. Thus, the negative capillary energy scales as N . The difference in scaling of the positive bending energy and negative capillary energy results in minimum energy for a critical cluster size, N_c . The bending energy of a rod, which is fixed at one end, of radius r , length h and elastic modulus E , is given as,²²

$$\Delta E_b = \frac{3\pi E r^4 \delta^2}{8h^3} \quad (6.4)$$

where δ is the displacement of the free end of the rod. Because of the symmetry of the underlying square lattice, the micropillars in a cluster also pack in a square lattice in general (Fig. 6.4c). The total bending of a cluster packed in a square lattice (Fig. 6.4b) can be viewed as sum of bending of perimeters $n = 1, 2, 3, 4, \dots$ i.e. $\delta^2 = \sum \delta_n^2$.

Cumulative bending in perimeter n can be obtained as

$$\delta_n^2 = 4\left(\frac{s}{2}\right)^2 \left[(2n-1)^2 + (2n-1)^2 \right] + 8\left(\frac{s}{2}\right)^2 \sum_{i=1}^{n-1} \left[(2n-1)^2 + (2i-1)^2 \right] \quad (6.5)$$

where the first term represents the bending of 4 corner pillars, and the second term represents the bending of the remaining $8(n-1)$ pillars in perimeter n . Here, s is the separation of the pillars (Fig. 6.4b). Thus, the total bending of a cluster having n perimeters is given as

$$\delta^2 = \sum \delta_n^2 = \frac{s^2}{3} (8n^4 - 2n^2 + 6n - 6) \quad (6.6)$$

Thus, by Eq. 6.4 and 6.6, the total elastic bending energy is given as

$$U_e = \frac{\pi E r^4 s^2 (8n^4 - 2n^2 + 6n - 6)}{8h^3} \quad (6.7)$$

Here the total number of pillars in a cluster, N , is given by $N = 4n^2$. Since in Eq. 6.7, U_e roughly scales as $\sim n^4$, thus, $U_e \sim N^2$ as mentioned earlier.

The capillary energy of two vertical cylindrical rods of radius r and separated by center-to-center distance $2l$, partially submerged in a liquid is given as¹³

$$W = 2\pi\gamma r^2 \cos^2 \theta \left(\ln \frac{(a+l)\gamma_e q}{1 + \sin \theta} \right) \quad (6.8)$$

where, γ is surface tension of the liquid, θ is the liquid contact angle on rod material. Here, $a = \sqrt{l^2 - r^2}$, γ_e is Euler-Macaroni number ($\gamma_e = 1.78107$) and $q^{-1} = \sqrt{\frac{\gamma}{\rho g}}$ is the capillary length, where ρ is density of liquid and g is gravitational acceleration. Each pillar is surrounded by 8 pillars, including 4 corner pillars (center to center distance $\sqrt{2}(2r+s)$ when not collapsed and $2\sqrt{2}(r)$ when collapsed) and 4 adjacent pillars (center to center distance $(2r+s)$ when not collapsed and $2r$ when collapsed) (see Fig. 6.4b). For both geometries A and B, $s = 2r$. Thus, by Eq. 6.8, the total change in capillary meniscus interaction energy from the non-collapsed to collapsed state (Fig. 6.4b) of a cluster with n perimeters is calculated as,

$$U_c = -4\pi\gamma r^2 \cos^2 \theta \left((4n^2 - 2n) \ln(\sqrt{3} + 2) + (4n^2 - 4n + 1) \ln\left(\frac{\sqrt{7} + 2\sqrt{2}}{\sqrt{2} + 1}\right) \right) \quad (6.9)$$

In Eq. 6.9 the first logarithmic term represents the capillary energy due to adjacent pillars whereas the second term represents that due to the corner pillars. The negative terms account for the fact that the outermost pillars in a cluster are surrounded

by less than 8 pillars. Further, the change in capillary meniscus interaction energy as obtained in Eq. 6.9 is independent of the capillary number q .

Thus, the total energy of forming a cluster is $U_t = U_c + U_e$. Minimization of the total energy by $\frac{\partial U_t}{\partial n} = 0$ gives

$$E = \frac{32\gamma \cos^2 \theta h^3}{r^2 s^2} \left(\frac{(8n_c - 2) \ln(\sqrt{3} + 2) + (8n_c - 4) \ln\left(\frac{\sqrt{7} + 2\sqrt{2}}{\sqrt{2} + 1}\right)}{32n_c^3 - 4n_c + 6} \right) \quad (6.10)$$

where, the number of pillars in a cluster, $N_c = 4n_c^2$. Numerically solving Eq. 6.10 in terms of N_c reveals a linear relation (Eq. 6.11) between N_c and $1/E$ (see Fig. 6.5). In Fig. 6.5, when extrapolated to $1/E = 0$, the linear fit to the numerical solution to Eq. 6.10 yields a negative N_c (Eq. 6.11). This negative value has no physical meaning but indicates that the linear relation does not hold for N_c less than 4. The linear relation can also be inferred by neglecting the numerical constants in the polynomials containing n_c in Eq. 6.10 and then solving analytically for N_c .

$$N_c \approx \frac{64.51 \cos^2 \theta \gamma h^3}{Er^2 s^2} - 2.11 \quad (6.11)$$

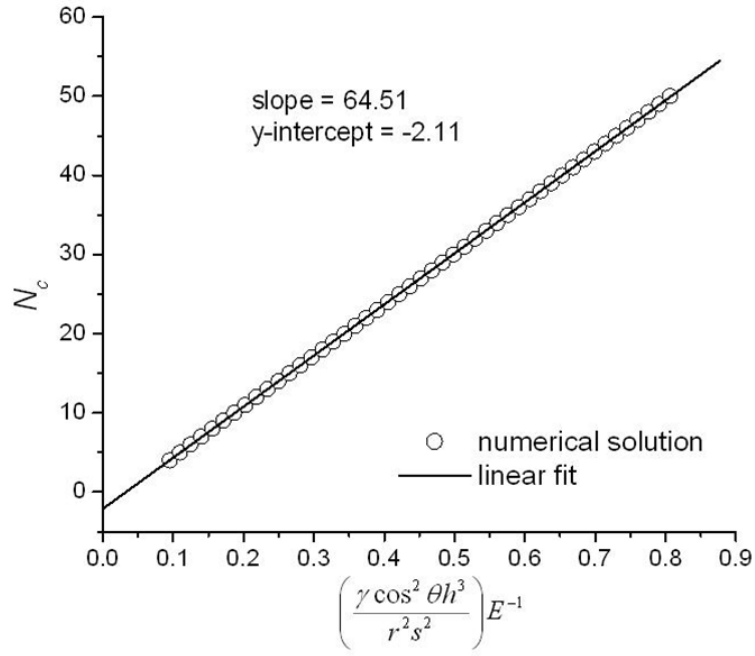


Figure 6.5 Numerical solution to equation 6.10 and linear fit to the solution points.

Previously, Zhao et al²³ predicted that cluster size was dependent on gravity through the capillary length q^{-1} . However, Eq. 6.10 and 6.11 suggests that gravity should not be relevant to the change in capillary interaction energy where the cluster size is independent of q . From Eq. 6.11, the cluster size is inversely proportional to the elastic modulus of the micropillars with a slope of $(64.51\gamma \cos^2 \theta h^3) / r^2 s^2$. To validate the above relation, we compared the experimentally observed cluster size to the prediction according to Eq. 6.11.

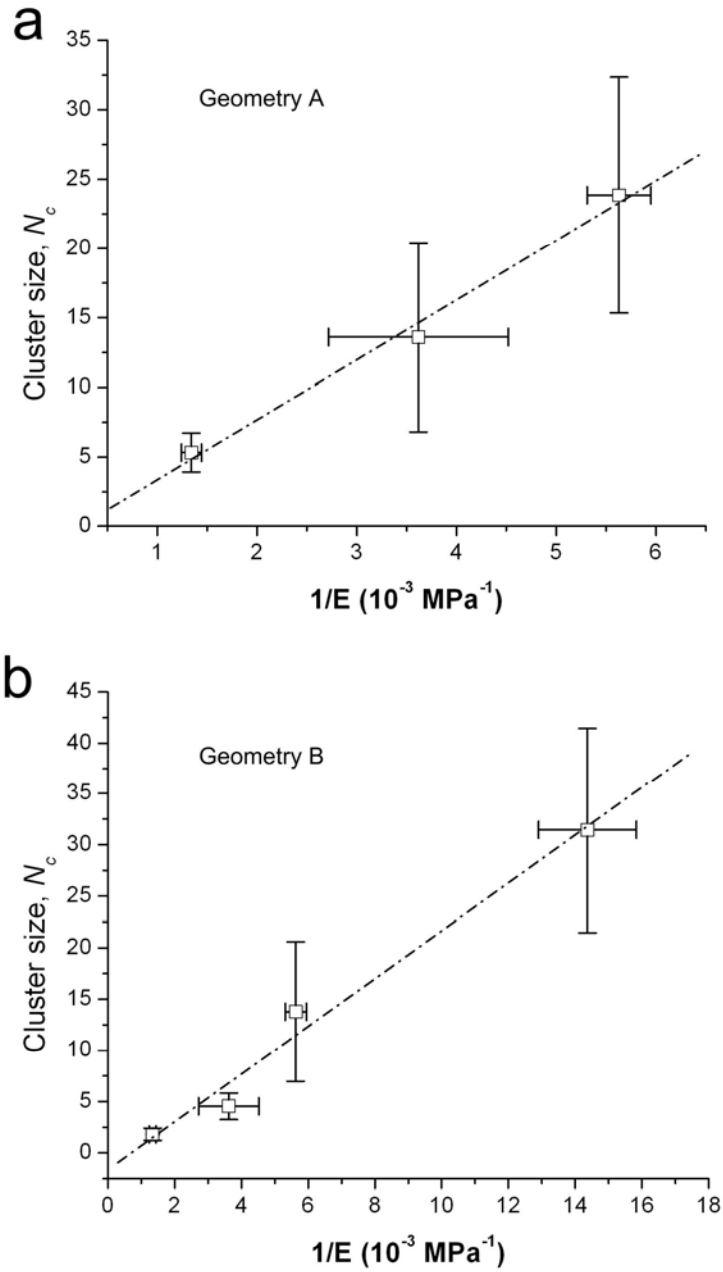


Figure 6.6 Micropillar cluster size as a function of the elastic modulus of micropillars in wet state for (a) geometry A and (b) geometry B. Dashed lines are linear fit ($r^2 = 0.99$ and 0.98 in (a) and (b) respectively) to experimental data.

The elastic modulus E was experimentally determined by AFM nanoindentation of PHEMA-*co*-PMMA samples immersed in water (Fig. 6.3a). The measured water contact angle θ in Eq. 6.11 was found to increase with increasing MMA wt% initially but leveled off at $\sim 73^\circ$ when MMA content ≥ 40 wt% (Fig. 6.3b).

In Fig. 6.6 we plot experimentally observed values of N_c versus $1/E$ for both pillar array geometries. The vertical error bars represent the standard deviation of the cluster sizes in a sample and horizontal error bars represent the error in elastic modulus measurement. The dashed lines in Fig. 6.6 are linear fit to the experimental data confirming the linear relation between cluster size and $1/E$. The slopes of the linear fit yield contact angle (θ) values of 72° for geometry A and 66° for geometry B which are close to measured value of 73° (Fig. 6.3b) within experimental error. We note that for geometry A however, we could have only three cluster size data because for PMMA content ≤ 40 wt% the cluster size was too large to have distinguishable clusters (Fig. 6.2).

6.3.3 Critical elastic modulus for stability

From Fig. 6.2 and 6.3a, the micropillar arrays in both the geometries A and B are stable at elastic modulus of 1.2 GPa (75% MMA) and unstable for elastic modulus of 745 MPa (67% MMA), although many of the micropillars in geometry B do not collapse for 67% MMA sample (Fig. 6.2). The critical elastic moduli for the two geometries ($\theta = 73^\circ$) as estimated by Eq. 5.9 (based on capillary meniscus interaction force) derived in Chapter 5, are 714 MPa and 226 MPa for geometry A and B respectively, which are close to the experimentally suggested range. In comparison, by Eq. 5.11 (based on Laplace pressure due to isolated capillary bridge) in Chapter 5, the critical elastic moduli are estimated as

16.7 GPa (geometry A) and 4.1 GPa (geometry B) which are much larger than 1.2 GPa for which the micropillars in both the geometries were found stable experimentally.

The above comparison of critical elastic moduli values and the theoretical and experimental investigation of cluster sizes in the preceding section, convincingly confirm that in 2D arrays of tall microstructures, capillary meniscus interaction, rather than the Laplace pressure difference due to isolated capillary bridges, is the main reason for mechanical instability upon liquid drying.

6.3.4 Whiteness of clustered micropillars

Finally, we investigated the optical effect of the capillary force induced clustering of micropillar array as ultrathin whitening layers. Whiteness is important for many technologies such as paper industry, coatings, textiles and electronic displays. In these systems, film thickness exceeds 100 microns, and whiteness is often enhanced by pigmentation or by fluorescent dyes. Nature, on the other hand, provides elegant examples of brilliant structural colors such as shown in the scales of white beetles, where their white color results from light scattering from random network of microfilaments that is only a few microns thick.¹⁴ Before collapsing the micropillar arrays had angle-dependent colorful reflection due to Bragg diffraction of light from the highly ordered pattern (Fig. 6.7a). After soaking in water and drying in air, however, the pillar array became randomly clustered and appeared white, which was attributed to random scattering of light (Fig. 6.7a), similar to the phenomenon observed in the white beetle scales. We characterized the whiteness of the randomly clustered micropillar arrays in Fig. 6.2 by measuring their CIE lightness index,²⁰ L , using a photospectrometer (Fig. 6.7b). For a low PMMA content, the micropillars ground collapsed completely due to the

low elastic modulus, resulting in low L . With the increase in PMMA content, the pillars laterally collapsed into random clusters, and L gradually increased. In general, the lightness index for geometry A was slightly higher than that for geometry B at the same composition since A had larger cluster sizes than B. When PMMA content was greater than 60 wt%, the micropillar arrays began to reappear colorful due to less collapsing of pillars. We observed a maximum lightness index L_{\max} of ~ 45 for our structures, which were less than 9 μm thick (the micropillar height). In comparison, conventional uncoated paper has lightness index of ~ 70 over 120 μm thickness. Although our clustered micropillar arrays are 33% less white than the uncoated paper, the film thickness is 15 times thinner, which is important as a proof of concept for ultrathin structural whiteness.

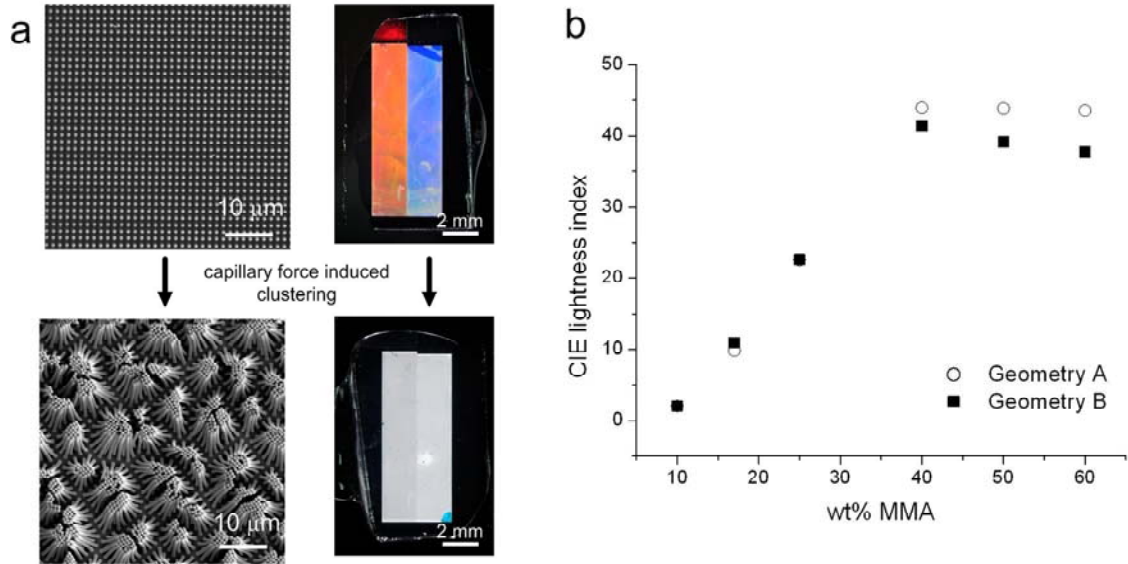


Figure 6.7 Whiteness caused by random clustering of micropillar arrays and the corresponding CIE lightness index. (a) SEM (left) and optical images (right) of micropillar arrays before and after clustering. Two different colors in (a) (top right) result from Bragg diffraction of micropillar arrays with different periodicity. (b) CIE lightness index of clustered micropillar arrays as a function of MMA content.

6.4 Conclusions

We studied the capillary force induced clustering of highly ordered polymeric micropillar arrays of well defined geometries. By changing the composition of the water swellable PHEMA versus glassy, non-swelling PMMA, we experimentally observed the effect of elastic modulus on micropillar cluster size. By minimizing the sum of capillary meniscus interaction energy and elastic bending energy, we estimated the average cluster size as a function of pillar elastic modulus and geometry, which agreed well with the experimental values in general. The cluster size analysis together with the investigation of critical elastic modulus for stability, convincingly demonstrate that in 2D arrays of tall microstructures, capillary meniscus interaction, rather than the Laplace pressure difference due to isolated capillary bridges, is the main reason for mechanical instability upon liquid drying. Finally we demonstrated the application of random clustering of micropillars for ultrathin (9 μm) whitening layers, mimicking the brilliant whiteness effect observed in ultrathin beetle scales, which contains randomly packed filaments.¹⁴

6.5 References

- (1) Krupenkin, T. N.; Taylor, J. A.; Schneider, T. M.; Yang, S. *Langmuir* **2004**, *20*, 3824.
- (2) du Roure, O.; Saez, A.; Buguin, A.; Austin, R. H.; Chavrier, P.; Siberzan, P.; Ladoux, B. *Proc. Natl. Acad. Sci. U. S. A.* **2005**, *102*, 2390.
- (3) Tan, J. L.; Tien, J.; Pirone, D. M.; Gray, D. S.; Bhadriraju, K.; Chen, C. S. *Proc. Natl. Acad. Sci. U. S. A.* **2003**, *100*, 1484.

- (4) Kaji, N.; Tezuka, Y.; Takamura, Y.; Ueda, M.; Nishimoto, T.; Nakanishi, H.; Horiike, Y.; Baba, Y. *Anal. Chem.* **2004**, *76*, 15.
- (5) Chandra, D.; Taylor, J. A.; Yang, S. *Soft Matter* **2008**, *4*, 979.
- (6) Fan, J. G.; Dyer, D.; Zhang, G.; Zhao, Y. P. *Nano Lett.* **2004**, *4*, 2133.
- (7) Tanaka, T.; Morigami, M.; Atoda, N. *Jpn. J. Appl. Phys.* **1993**, *32*, 6059.
- (8) Chakrapani, N.; Wei, B.; Carrillo, A.; Ajayan, P. M.; Kane, R. S. *Proc. Natl. Acad. Sci. U. S. A.* **2004**, *101*, 4009.
- (9) Pokroy, B.; Kang, S. H.; Mahadevan, L.; Aizenberg, J. *Science* **2009**, *323*, 237.
- (10) Segawa, H.; Yamaguchi, S.; Yamazaki, Y.; Yano, T.; Shibata, S.; Misawa, H. *Appl. Phys. A* **2006**, *83*, 447.
- (11) Bico, J.; Roman, B.; Moulin, L.; Boudaoud, A. *Nature* **2004**, *432*, 690.
- (12) Py, C.; Bastien, R.; Bico, J.; Roman, B.; Boudaoud, A. *Europhys. Lett.* **2007**, *77*, 44005.
- (13) Kralchevsky, P. A.; Paunov, V. N.; Ivanov, I. B.; Nagayama, K. *J. Colloid Interface Sci.* **1992**, *151*, 79.
- (14) Vukusic, P.; Hallam, B.; Noyes, J. *Science* **2007**, *315*, 348.
- (15) Cappella, B.; Kaliappan, S. K.; Sturm, H. *Macromolecules* **2005**, *38*, 1874.
- (16) Domke, J.; Radmacher, M. *Langmuir* **1998**, *14*, 3320.
- (17) Dong, R.; Jensen, T. W.; Engberg, K.; Nuzzo, R. G.; Leckband, D. E. *Langmuir* **2007**, *23*, 1483.
- (18) Sader, J. E.; Chon, J. W. M.; Mulvaney, M. *Rev. Sci. Instrum.* **1999**, *70*, 3967.
- (19) Sneddon, I. N. *Int. J. Eng. Sci.* **1965**, *3*, 47.

- (20) Wyszecki, G.; Stiles, W. S. *Color Science Concepts and Methods, Quantitative Data and Formulae*; Second ed.; John Wiley and Sons, Inc., 2000.
- (21) Zhang, Y.; Lo, C. W.; Taylor, J. A.; Yang, S. *Langmuir* **2006**, 22, 8595.
- (22) Beer, F. B.; Johnston, E. R. *Mechanics of Materials*; Mc Graw-Hill, Inc., 1992.
- (23) Zhao, Y. P.; Fan, J. G. *Appl. Phys. Lett.* **2006**, 88, 103123.

Chapter 7

Dynamics of Droplet Imbibition on a Rough Surface

In Chapters 5 and 6 we discussed the effect of capillary force on the stability of the micropillars. However, surface roughness such as that provided by the micropillar arrays also causes the capillary driven wetting dynamics on the topographic surface. In this Chapter, we theoretically study the dynamics of imbibition of a droplet on a rough surface and show that the droplet imbibition dynamics deviates from the classical $\sim t^{0.5}$ Washburn law¹.

7.1 Introduction

On a flat, smooth surface, the liquid contact angle θ_0 is determined by minimization of the surface energies involved – liquid-vapor (γ), solid-vapor (γ_{sv}) and solid-liquid (γ_{sl}) according to the Young's equation: $\cos \theta_0 = (\gamma_{sv} - \gamma_{sl}) / \gamma$. Surface roughness, however, modifies the wetting property of the surfaces,^{2,3} and is responsible for interesting natural phenomenon, such as superhydrophobicity of lotus leaves⁴ and collection of drinking water from fog by a Namibian desert beetle⁵. In addition, surface topography is also known to affect the dynamics of wetting^{6,7}. A liquid droplet placed on a rough hydrophilic surface ($\theta_0 < 90^\circ$), spreads towards its equilibrium contact angle faster than a droplet placed on a chemically identical, smooth surface⁷.

The roughness of a surface can be characterized by two geometrical parameters:

(a) the roughness factor r , which is the ratio of the actual surface area to its horizontal

projection, and (b) the solid fraction ϕ at the top of the roughness (for example, in case of micropillar arrays, ϕ is the fraction of the horizontally projected area covered by the micropillar tips). A critical contact angle θ_c is defined in terms of r and ϕ and is given by⁸,

$$\cos \theta_c = \frac{1-\phi}{r-\phi} \quad (7.1)$$

For a rough hydrophilic ($\theta_0 < 90^\circ$) surface, when $\theta_0 > \theta_c$ a liquid droplet placed on the surface penetrates the grooves (Fig. 7.1a), resulting in an equilibrium contact angle θ_w given by the Wenzel equation³,

$$\cos \theta_w = r \cos \theta_0 \quad (7.2)$$

When $\theta_0 < \theta_c$ it is energetically favorable for the liquid to imbibe into the grooves of the rough surface, so called hemi-wicking wetting⁸ (Fig. 7.1b). In this case, a liquid droplet sits on a solid-liquid composite surface and slowly imbibes into the surface roughness while maintaining a constant contact angle θ_i given as⁸,

$$\cos \theta_i = 1 - \phi(1 - \cos \theta_0) \quad (7.3)$$

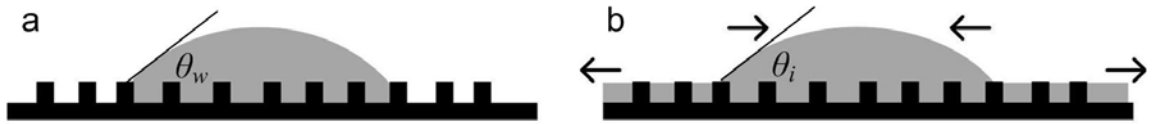


Figure 7.1 A droplet sitting in Wenzel state (a) and imbibing into the grooves in hemi-wicking state (b).

When a rough surface is placed in contact with a reservoir of a liquid satisfying the condition $\theta_0 < \theta_c$, the liquid spontaneously imbibes into the surface roughness driven

by capillary force (see Section 2.5). The dynamics of imbibition is important for areas such as water transport and retention in soil and plants and in technologies such as inking, coloring, textiles and microfluidics. Capillary induced imbibition of liquids, both in channels⁹ and on rough surfaces⁸ when in contact with a liquid reservoir, has been known to follow the classical Washburn dynamics: $l \sim t^{0.5}$ where l is the distance traveled by imbibing front and t is time. The $\sim t^{0.5}$ dynamics in these one-dimensional, non-diverging flows occurs because of a constant capillary energy change balancing the viscous dissipation in ever increasing length of liquid flow. Deviation from the above relation, resulting in a slower dynamics but still following a power law, has also been reported in cases, such as non-uniform channel cross-section¹⁰ and a finite liquid volume imbibing in a network of channels¹¹.

In this Chapter, we consider a micropillar array as a model rough surface and theoretically calculate the dynamics of a liquid droplet imbibing on such rough surfaces. The imbibition of a droplet differs from one-dimensional imbibition from a reservoir in two respects: (a) because of finite small droplet volume the imbibition source depletes with time and (b) the flow geometry is radial. Because of shrinking droplet and radial flow geometry, the dynamics does not follow a simple power law. The liquid flow starts with $\sim t^{0.5}$ dynamics but the dynamics continues to decrease to become slower than $\sim t^{0.5}$ at longer times.

7.2 Model description

We consider a micropillar array as a model rough surface. For a micropillar array, the roughness parameters r and ϕ defined above can be independently

controlled to satisfy the imbibition condition, $\theta_0 < \theta_c$ described above. For example, r can be increased independently of ϕ by increasing the micropillar aspect-ratio. We define two geometrical parameters, $\alpha = 1 - \phi$ and $\beta = r - \phi$. Let the micropillar height be δ . Consider a droplet imbibing on the micropillar array surface as shown in Fig. 7.2. The droplet contact angle with the solid-liquid composite surface is θ_i and is given by Eq. 7.3. The initial radius of the droplet at $t = 0$ is r_0 . V_0 is the total liquid volume

$$V_0 = gr_0^3 + \pi r_0^2 \delta \alpha \quad (7.4)$$

where gr_0^3 is the volume of the droplet spherical cap; g is a geometrical constant which depends on the droplet contact angle θ_i . At time t , let the liquid imbibes to radius r and the droplet shrinks to radius r_d . Then, by conservation of liquid volume, the droplet radius r_d becomes

$$r_d = r_0 \left(1 - \frac{\pi(r^2 - r_0^2)\delta\alpha}{gr_0^3} \right) \quad (7.5)$$

$v = dr/dt$ is the velocity of the liquid front. We are interested in the evolution of the imbibition length $l = r - r_0$ with time t .

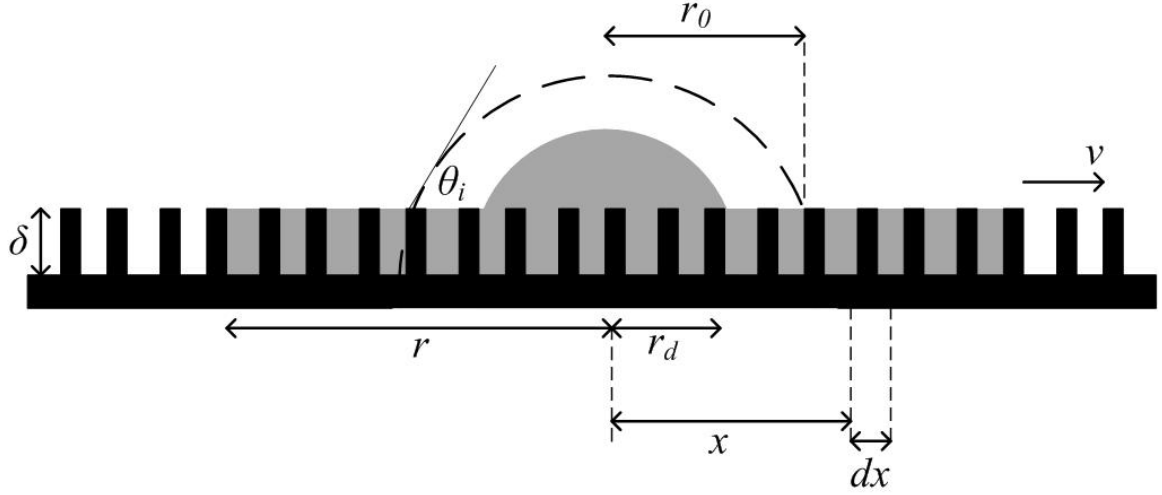


Figure 7.2 Schematic showing parameters for a droplet imbibing in a rough surface.

7.3 Results and discussion

Unlike 1D non-diverging flow, in the radial flow geometry in Fig. 7.2, the fluid velocity is not constant over the whole imbibed liquid volume. By conservation of volume flux, the velocity at radius x is $v_x = vr/x$. Thus, the viscous dissipation rate is,

$$U_v = 2\pi\eta\delta\varepsilon \int_{r_d}^r \left(\frac{v_x}{\delta} \right)^2 x dx \quad (7.6)$$

where η is the liquid viscosity and ε is a constant dimensionless pre-factor.

Putting $v_x = vr/x$ in Eq. 7.6 and integrating, the expression for viscous dissipation becomes,

$$U_v = \frac{2\pi\eta\varepsilon v^2 r^2}{\delta} \ln \left(\frac{r}{r_d} \right) \quad (7.7)$$

The rate of change of capillary energy is given as,

$$U_c = 2\pi\gamma(\beta \cos \theta_{eq} - \alpha)rv \quad (7.8)$$

Equating the viscous dissipation rate (Eq. 7.7) and the rate of change of capillary energy (Eq. 7.8) and integrating yields,

$$\int_{r_0}^r r \ln\left(\frac{r}{r_d}\right) dr = \frac{\delta\gamma}{\eta\epsilon} (\beta \cos \theta_{eq} - \alpha) \int_0^t dt \quad (7.9)$$

Using r_d from Eq. 7.5 and integrating Eq. 7.9 gives the imbibition dynamics as,

$$er_0^2 \left[m^2 \ln(m) - \frac{m^2}{3} \ln\left(\frac{1-fm^2}{e/b}\right) + \frac{1}{3f} \ln\left(\frac{1-fm^2}{1-f/e}\right) + a \right] = 2ct \quad (7.10)$$

where m is the dimensionless imbibition length as $m = \frac{l+r_0}{r_0 e^{1/2}}$, e is the Euler's number, a

is a constant to satisfy the limits of integral in Eq. 7.9 and b , c , and f are constants for the

system as, $c = \frac{\delta\gamma}{\eta\epsilon} (\beta \cos \theta_0 - \alpha)$, $f = \frac{\pi e \alpha \delta}{gr_0 + \pi \delta \alpha}$ and $b = 1 + \frac{\pi \delta \alpha}{gr_0}$.

From Eq. 7.10, it is clear that the droplet imbibition dynamics does not follow a simple power law. In comparison, dynamics of 1D non-diverging imbibition from a reservoir (see Section 2.5) is,

$$l^2 = 2ct \quad (7.11)$$

We plot l vs. t and $\ln(l)$ vs. $\ln(t)$ for a typical case of $r_0 = 1$ mm, $\delta = 10$ μ m, $\theta_i = 45^\circ$ and $\phi = 0.25$ in Fig. 3 according to Eq. 7.10 and Eq. 7.11, respectively. From Fig. 7.3a, it is clear that the droplet imbibition is slower than the imbibition from a reservoir. The log-log plot in Fig. 3b shows that the droplet imbibition starts with $\sim t^{0.5}$ dynamics but slows down with time. Further, we calculate the slope, $d(\ln l)/d(\ln t)$ of Fig. 7.3b from Eq. 7.10 and plot it vs. time, t in Fig. 7.4. Again, it shows that at the very beginning of

imbibition, the slope is close to 0.5 (at time $t = 0$ the slope is calculated as 0.5) but continues to decrease with time.

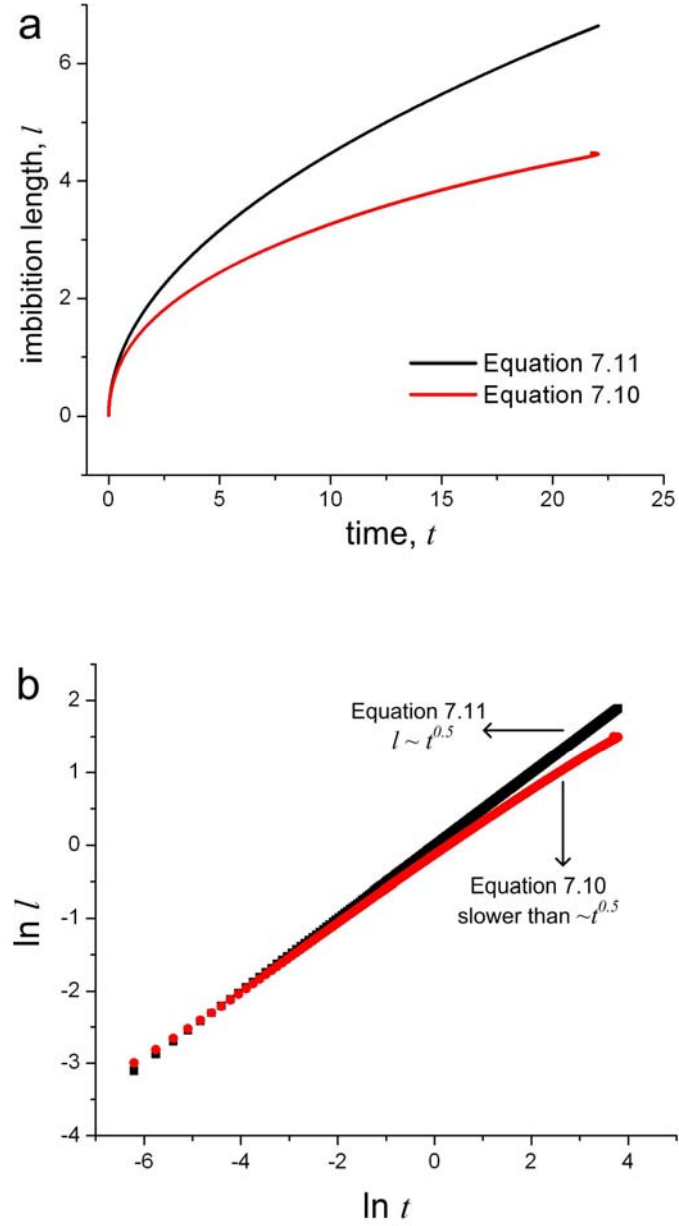


Figure 7.3 Calculated dynamics of droplet imbibition (Eq. 7.10) and 1D imbibition from a reservoir (Eq. 7.11).

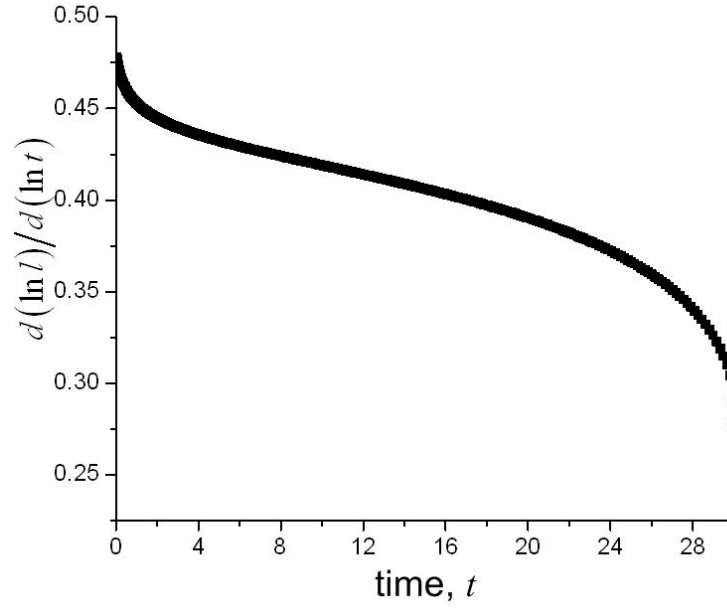


Figure 7.4 Slope of a typical $\ln(l)$ vs. $\ln(t)$ plot of a droplet imbibing in a rough surface as a function of time.

To better understand the origin of the slower imbibition dynamics, we decouple the effects of shrinking droplet and radial flow by considering a non-shrinking droplet of radius r_0 . Practically, the liquid droplet size can be maintained by continuously pumping the liquid from a reservoir (for example from a needle syringe). In this case, r_d is replaced by r_0 in Eq. 7.9 and the imbibition dynamics becomes,

$$er_0^2 \left[m^2 \ln(m) + 1/2e \right] = 2ct \quad (7.12)$$

The slope $d(\ln l)/d(\ln t)$ is

$$\frac{d(\ln l)}{d(\ln t)} = \frac{m^2 \ln m + 1/2e}{(m + 2m \ln(m))(m - e^{-1/2})} \quad (7.13)$$

A plot of the slope (Eq. 7.13) vs. time t shows that the slope decreases only slightly from 0.5 with time (Fig. 7.5). Thus, the slower imbibition dynamics shown in Fig. 7.3 and 7.4 should be largely due to the shrinking of the imbibing droplet with time. As the droplet shrinks and imbibes in the roughness, the length $(r - r_d)$ over which the viscous dissipation occurs increases due to both increasing r and decreasing r_d with time. In contrast, in case of imbibition from a non-shrinking reservoir, the length over which the viscous dissipation occurs is $(r - r_0)$, which increases only due to increasing r with time. Thus, a larger viscous dissipation in case of a shrinking droplet leads to a slower imbibition dynamics.

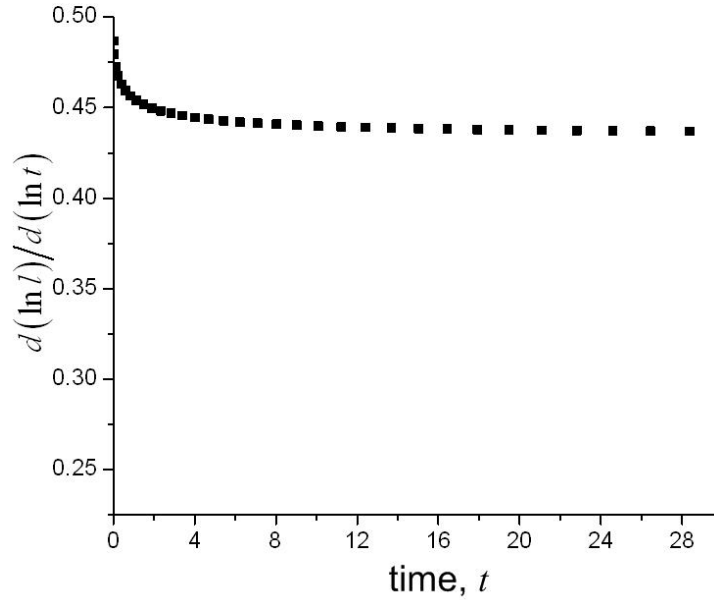


Figure 7.5 Slope of a typical $\ln(l)$ vs. $\ln(t)$ plot of a non-shrinking droplet imbibing in a rough surface as a function of time.

7.4 Conclusions

In conclusion, we have shown theoretically that the dynamics of the imbibition of a droplet on rough surface deviates from the classical Washburn dynamics. The droplet imbibition dynamics does not follow a simple power law. The imbibition starts with $\sim t^{0.5}$ dynamics but continues to slow down with time. The slower dynamics is attributed to an increased viscous dissipation due to shrinking droplet as compared to dissipation in imbibition from a non-shrinking liquid source. The present analysis of droplet imbibition would be significant for applications such as inking and microfluidic analysis where spreading behavior of droplets is important.

7.5 References

- (1) Washburn, E. W. *Phys. Rev.* **1921**, *17*, 273.
- (2) Cassie, A. B. D.; Baxter, S. *Trans. Far. Soc.* **1944**, *40*, 546.
- (3) Wenzel, R. N. *Ind. Eng. Chem.* **1936**, *28*, 988.
- (4) Barthlott, W.; Neinhuis, C. *Planta* **1997**, *202*, 1.
- (5) Parker, A. R.; Lawrence, C. R. *Nature* **2001**, *414*, 33.
- (6) Cazabat, A. M.; Stuart, M. A. C. *J. Phys. Chem.* **1986**, *90*, 5845.
- (7) McHale, G.; Shirtcliffe, N. J.; Aquil, S.; Perry, C. C.; Newton, M. I. *Phys. Rev. Lett.* **2004**, *93*, 036102.
- (8) Bico, J.; Tordeux, C.; Quere, D. *Europhys. Lett.* **2001**, *55*, 214.
- (9) Mann Jr., J. A.; Romero, R.; Rye, R. R.; Yost, F. G. *Phys. Rev. E* **1995**, *52*, 3967.
- (10) Reyssat, M.; Courbin, L.; Reyssat, E.; Stone, H. A. *J. Fluid Mech.* **2008**, *615*, 335.
- (11) Warren, P. B. *Phys. Rev. E* **2004**, *69*, 041601.

Chapter 8

Summary and Future Outlook

8.1 Summary

In this thesis we explored the capillary force driven mechanical instability of high aspect-ratio (HAR) micropillar arrays. We showed that when a liquid is evaporated off the micropillar arrays, the pillars bend and cluster together due to capillary meniscus interaction force rather than due to often reported Laplace pressure difference because of isolated capillary bridges. We studied both theoretically and experimentally, the capillary force induced clustering behavior of micropillar arrays as a function of their elastic modulus. To this end, we developed a modified replica molding process to mold hydrogel micropillar arrays whose elastic modulus in the wet state could be tuned by simply varying the hydrogel monomer composition. We explored the utility of the clustered micropillar arrays as ultrathin whitening layers mimicking the structural whitening mechanism found in some insects in nature. Finally, we studied theoretically the capillary force induced imbibition of a liquid droplet in a model rough surface consisting of micropillar arrays and showed that due to shrinking droplet, the imbibition dynamics did not follow the Washburn dynamics but became progressively slower with time.

We started with an introduction to HAR micropillar arrays, their applications, fabrication methods and their common mechanical failure modes in Chapter 1. In Chapter 2 we discussed capillary force relevant to clustering of micropillar arrays and capillary

force induced wetting dynamics in micropillar arrays. In Chapter 3 we discussed the experimental methods used in this thesis.

In Chapter 4 we described a novel two-step process to fabricate HAR hydrogel micropillar arrays by replica molding. Direct molding of hydrogel monomers by using a soft elastomeric (poly(dimethyl siloxane), PDMS) mold followed by UV initiated free-radical polymerization was found not possible because the monomers would diffuse into the mold and distort it. Further, the oxygen dissolved in the mold could diffuse out and inhibit the free radical polymerization. In a modified process, we first partially polymerized the hydrogel monomers, which were then used as molding precursor for subsequent UV curing. The increased viscosity of the prepolymers played a critical role in preventing both the monomer diffusion into the PDMS mold and oxygen diffusion out of the mold. We successfully demonstrated fabrication of high density ($>10^7$ pillars/cm²), high aspect-ratio (up to 12) micropillar arrays in three different geometries and three different compositions. Because of their high Young's modulus in the dry state, all hydrogel pillar arrays were stable in air against adhesive forces. However, when exposed to a wetting liquid, the micropillar arrays collapsed either due to drastically reduced elastic modulus upon hydration by water (e.g. poly(2-hydroxyethylmethacrylate-*co*-N-isopropyl acrylamide) (PHEMA-*co*-PNIPA) and PHEMA micropillar arrays) or due to large capillary force exerted to the pillar array during liquid evaporation (e.g. poly(ethylene glycol dimethacrylate) (PEGDMA) micropillar arrays wetted by low surface energy ethanol). The capillary force induced collapsing behavior of PEGDMA micropillar arrays was found dependent on the pillar array geometry, and in some cases, hierarchical assembly of the micropillars were observed.

In order to understand their capillary force induced clustering behavior, in Chapter 5, we investigated the nature of capillary force acting on 2D micropillar arrays during liquid evaporation off their surface. Using low molecular weight polystyrene as the wetting liquid on epoxy micropillar arrays, we discovered that the micropillars collapse during liquid evaporation while they were still surrounded by a continuous liquid body and that there were no isolated capillary bridges present. Thus, we experimentally showed for the first time that the capillary force induced clustering of 2D arrays of micropillars should be attributed to lateral forces resulting from the interaction between capillary menisci around individual pillars rather than to often reported Laplace pressure difference due to isolated capillary bridges. Supporting this, we theoretically estimated the Laplace pressure force, which was found more than an order of magnitude larger than that the capillary meniscus interaction force. This difference was reflected in large difference in the elastic modulus for stability calculated from the two approaches.

In Chapter 6, we studied the capillary force induced clustering of poly(2-hydroxyethylmethacrylate-*co*-methyl methacrylate) (PHEMA-*co*-PMMA) micropillar arrays fabricated by the process described in Chapter 4. By varying the composition of water swellable PHEMA versus the glassy, non-swellable PMMA in the molding materials, we modulated the elastic modulus of the micropillars in the wet state over three orders of magnitude. By minimizing the sum of elastic bending energy and the capillary meniscus interaction energy of the pillars in a cluster, we derived an expression for the micropillar cluster size, which was inversely proportional to the elastic modulus of the pillars. The derived relationship agreed well with the experimental observation. The critical elastic modulus for stability as calculated from the expression derived in Chapter

5 was also in agreement with the experimental observation whereas the critical modulus calculated by the Laplace pressure approach was found to be much larger than the values suggested by experiment. By comparing the experimental and theoretical studies we further demonstrated that in case of 2D micropillar arrays, capillary meniscus interaction rather than the Laplace pressure difference was the relevant capillary force that induced pattern collapse in micropillar arrays. Further, we demonstrated the utility of the randomly clustered micropillar arrays as biomimetic ultrathin whitening layers.

Finally, in Chapter 7 we theoretically studied the capillary driven imbibition of a liquid droplet in a model rough surface, micropillar arrays. We showed that because of the shrinking droplet and radial flow geometry, the droplet imbibition dynamics does not follow the simple Washburn power law dynamics. Instead, the imbibition dynamics started as $\sim t^{0.5}$ but progressively slowed down with time. This slower dynamics was attributed primarily to shrinking droplet which resulted in a greater viscous dissipation as compared to that in case of imbibition from a non-shrinking reservoir.

8.2 Future work

The work presented in this thesis provides important insights into capillary force induced mechanical instability of high aspect ratio micro- and nanostructures. It paves way for future research in both the fundamental aspects and their applications to advanced materials.

For example, in both Chapters 4 and 6 we observed micropillars clustered in groups of four, forming regular hierarchical structures. In Chapter 6 we observed that the micropillar clustering starts with group of four pillars clustering together, whereas in

Chapter 4 we observed that while less dense pillar arrays collapsed randomly, denser ones formed regular hierarchical structures. These observations suggest that the formation of regular clusters is dependent on the inter-pillar spacing. We speculate that less dense pillars, when they start to cluster, have higher degree of freedom and thus collapse randomly as compared to denser pillar arrays. To confirm this, the clustering behavior as a function of pillar array geometry, in particular inter-pillar spacing, should be explored. In addition, clustering behavior of micropillar arrays in other lattices, such as hexagonal arrays, could result in completely different but unique hierarchical structures.

To calculate the capillary meniscus interaction energy of the micropillar clusters in Chapter 6, we summed the interaction energies of all pairs of nearest neighbor micropillars. This superposition principle has been used to describe the capillary force induced assembly of colloidal particles¹. However, since the interaction energy is due to deformation of the liquid surface in the presence of the solid bodies, the interaction energy of a pair of micropillars in an array may be somewhat different from that of an isolated pair of micropillars. It would be interesting to calculate the interaction energy of a pair of micropillars in an array and compare it to the interaction energy of an isolated pair of micropillars. In this thesis we have addressed the clustering of the micropillars to obtain the cluster size in equilibrium. As a future direction, it would be interesting to study the kinetics of the clustering process. The kinetics should be governed by the net force on the micropillars due to capillary force and elastic restoration force, and by the viscous drag on the pillars due to the surrounding liquid as they bend towards each other. An understanding of the clustering kinetics would be useful to control the clustering

process, for example by using a high viscosity liquid, which may pave way for controlled assembly of the micropillars in desired periodic geometries. We note, however, that in case of high viscosity liquids, there would be significant energy dissipation due to viscous drag during clustering which will also affect the equilibrium cluster size.

In Chapter 7, we predicted a slower droplet imbibition dynamics in a model micropillar array surface, which is yet to be validated experimentally. As shown in Fig. 7.3b, the $\ln(l)$ vs. $\ln(t)$ plot of droplet imbibition deviates from that of imbibition from non-shrinking reservoir. However, in the log-log plot the deviation is rather small, making it difficult to observe experimentally. This may be the reason of reported $\sim t^{0.5}$ dynamics in the literature^{2,3}. Thus, to experimentally observe the slower dynamics, l vs. t plot (see Fig. 7.3a), rather than the log-log plot, of droplet imbibition should be compared to that of imbibition from non-shrinking reservoir for the same micropillar array.

From the application point of view, the analysis of critical modulus for stability in Chapter 5 can serve as a starting point to design micro- and nanoactuators. For example, the critical modulus depends on the liquid contact angle. Thus, by dynamically changing the contact angle (e.g. by means of electrowetting), and using elastic micropillar arrays (e.g. silicon), the micropillars can be alternated between clustered and non-clustered state. Such actuation can serve as micro-mixers in microfluidics channels. In addition, micropillars can be coated with responsive materials to achieve actuation in response to external stimuli. For example, by coating the micropillars with thermoresponsive polymer brush layer, thermal actuation of micropillars can be achieved by changing the contact angle with temperature. We demonstrated the application of randomly clustered micropillar arrays as ultrathin whitening layers. The degree of whiteness depends on the

structure of the scattering materials,⁴ which has not been fully explored in this thesis. As a future direction, the effect of factors, such as micropillar array geometry, porosity of the micropillars, and nanocomposites as pillar materials, on the resulting whiteness could be investigated.

8.3 References

- (1) Nishikawa, H.; Maenosono, S.; Yamaguchi, Y.; Okubo, T. *J. Nanopart. Res.* **2003**, *5*, 103.
- (2) Courbin, L.; Denieul, E.; Dressaire, E.; Roper, M.; Ajdari, A.; Stone, H. A. *Nat. Mater.* **2007**, *6*, 661.
- (3) Gerdes, S.; Cazabat, A. M.; Strom, G.; Tiberg, F. *Langmuir* **1998**, *14*, 7052.
- (4) McNeil, L. E.; French, R. H. *Acta Mater.* **2000**, *48*, 4571.

Appendix A

Strain Responsive Concave and Convex Microlens Arrays

During the course of the present thesis research, we also investigated a different kind of instability in an elastomeric material (PDMS) – buckling instability in response to a compressive load applied to a bi-layer structure consisting of a thick, soft elastomeric layer with a thin hard layer on top. By introducing buckling instability in a confined geometry, we fabricated concave microlens arrays whose focal length can be tuned in real time by applying external strain. Further, we replicated the concave microlens arrays in PDMS to obtain convex microlens arrays whose focal length is also tunable in response to external strain, albeit over a much shorter range as compared to the concave microlens arrays.

A.1 Introduction

With advances in miniaturization, microlens arrays play an important role in optical communication, biomedical imaging, photolithography, and biochemical sensing.^{1,2} Variable-focus microlens arrays are of particular interest for micro electromechanical systems (MEMS) and sensors. A wide variety of tuning mechanisms have been reported to tune lens shape, refractive index, and the surrounding medium by means of responsive hydrogels³, electrowetting⁴, liquid pressure to deform an elastomeric membrane⁵, liquid crystal microlens arrays⁶ and integrated microfluidic channels.⁷ Nevertheless, most of these microlens arrays are multi-component systems, and require complex fabrication and assembly processes. Often times, the lens focal length cannot be tuned continuously in real-time.

Here, we report the fabrication of a single-component, strain responsive, variable-focus microlens array (both concave and convex) with real-time tunability. The concave lens array is created by confined buckling of a soft elastomer, poly(dimethylsiloxane) (PDMS), which is mechanically stretched in plane bi-directionally⁸ and patterned with a thin layer of hard oxide on top. Due to extreme moduli mismatch between the hard silicate layer and the soft PDMS ($E \sim 2$ MPa) underneath, buckling occurs upon release of pre-strained bilayer film, forming wrinkled patterns spontaneously.^{8,9} If the oxidation and, thus, buckling is confined to an area smaller than the wavelength of the unconfined wrinkles, microlens structure will be obtained.¹⁰ Previously, similar strategy has been used to create microlens array by swelling a patterned oxide/PDMS bilayer structure with acrylate monomers, followed by polymerization.¹⁰ However, such formed lenses are rigid and not tunable. Because the microlens array in our system is created by mechanical stretching induced buckling, it offers several advantages over other tuning mechanisms, including reversible tuning of lens shape in real time by simply applying mechanical strain.

A.2 Experimental methods

Briefly, the microlens array was fabricated as the following. A flat PDMS sheet of thickness 0.5 mm was prepared by mixing PDMS precursor (RTV 615, GE Silicone) and curing agent (10:1 wt/wt) between two glass slides separated by spacers, followed by thermal curing at 65 °C for 4 hours. The PDMS strip was clamped on four edges (Fig. A.1a), leaving a center space of 25 mm x 25 mm and then stretched to 20% strain in both planar directions simultaneously (Fig. A.1b). One side of the stretched PDMS surface

was covered by scotch tape, while the other side was masked with a TEM copper grid (Fig. A.1c) with hexagonally packed hole array (diameter of 37 μm and hole to hole distance of 62 μm). The area surrounding the TEM grid was also covered with scotch tape. The stretched film with TEM grid on top was treated with ultraviolet ozone (UVO) (UVO-Cleaner Model 42, Jelight Company Inc.) for 30 minutes (Fig. A.1d) to generate a thin silicate layer on the exposed regions. After UVO treatment, the TEM grid and scotch tape were removed (Fig. A.1e) and the PDMS strip was strain released in both planar directions simultaneously, resulting in a concave microlens array (Fig. A.1f). To obtain the convex microlens array, we replica molded the concave microlens array in PDMS. The topography of the microlens arrays was characterized by atomic force microscope (AFM) (Digital Instruments, Dimension 3000).

The focal length of the microlens array at various mechanical strains was measured by optical microscope (Olympus BX-61) equipped with internal Z-motor (resolution of 1 μm). Alphabet 'N' was printed on a transparency and placed several centimeters below the microlens array (Fig. A.2e). First, the microlens array was brought into focus of the microscope objective (Fig. A.2b,d), and then the image of 'N' through the microlens array was brought into focus (Fig. A.2b,d, insets). The difference between the sample-stage positions of the two foci gave the focal length of the microlens array.

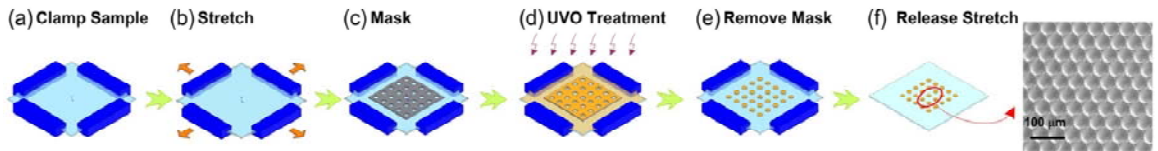


Figure A.1 Schematic illustration of the fabrication procedure of concave microlens array (a-f). (f) Inset: SEM image of a concave microlens array.

A.3 Results and discussion

In the range of pre-strain levels (10-30 %) and UVO treatment time (15-60 minutes), concave lenses were always observed. One possible explanation could be that during the strain release process, the pure PDMS surrounding the much stiffer oxidized PDMS is pushed out due to compressive forces, which favors buckling of the oxidized PDMS inwards rather than outwards. Once the oxidized layer is slightly buckled inwards, it continues to buckle in the same direction, resulting in formation of concave microlens array.

The fabricated microlenses appeared to have very uniform lens diameter D and lens thickness h over the whole array as measured by AFM (Fig. A.2a,c). D and h for the concave microlens array were 45.9 μm and 1.53 μm , respectively, whereas the corresponding values for the convex microlens array were a bit larger, 46.3 μm and 2 μm , respectively. The lens diameter D is significantly larger than the diameter of the holes in the copper grid, 37 μm . We suspect this is because (1) the contact between the TEM grid and PDMS sheet may not be completely flat, especially around the grid edge, and (2) the ozone could diffuse through the copper grid to some extent resulting in larger lenses.

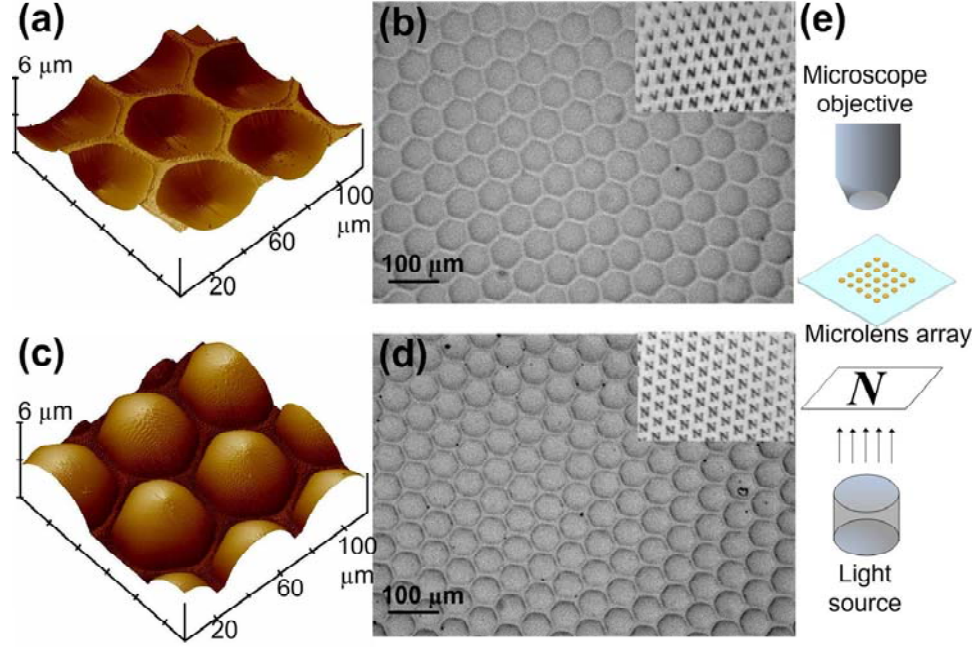


Figure A.2 AFM images of (a) concave and (c) convex microlens array. Optical images of (b) concave and (d) convex microlens arrays, corresponding to those from (a) and (c). Insets: the optical images of letter ‘N’ imaged through the respective microlens arrays. (e) Optical setup for measuring the microlens focal length.

Since the lens profile (D and h) is uniform over the microlens array, uniform focus is obtained over the entire array (Fig. A.2b,d, insets). Real focus is obtained for convex lens array and virtual focus is obtained for concave lens array.

While the non-confined ripples have sinusoidal profile, here, for the simplicity of estimation of the lens focal length, we assume the lenses are spherical with a single focal length. We find that it offers reasonable approximation of our shallow lens structure, and as shown later the calculated results agree well with the experiments within errors. For a thin spherical lens with diameter D and thickness h , the radius of curvature R is given by

$$R = D^2/8h + h/2 \quad (\text{A.1})$$

The lens volume (see Fig. A.3d) is

$$V_0 = \pi R^3 (\cos^3 \theta - 3 \cos \theta + 2) / 3 \quad (\text{A.2})$$

and the curved-surface area of the lens, A (see Fig. A.3c), is

$$A = 2\pi R^2 (1 - \cos \theta), \text{ where } \theta = \sin^{-1}(D/2R) \quad (\text{A.3})$$

Therefore, the focal length f in terms of A and D can be derived as

$$f = \frac{R}{n-1} = \frac{A}{2\pi(n-1)\sqrt{\frac{A}{\pi} - \frac{D^2}{4}}} \quad (\text{A.4})$$

where n is the refractive index of the lens material, here, PDMS bilayer. Under stretching with a strain ε , the lens diameter changes from D to $D(1+\varepsilon)$, and the focal length f of a stretched lens becomes

$$f = \frac{A}{2\pi(n-1)\sqrt{\frac{A}{\pi} - \frac{D^2(1+\varepsilon)^2}{4}}} \quad (\text{A.5})$$

The curved-surface area of the concave lens can be written in terms of the base area as $\pi D^2(1 + \varepsilon_0)^2/4$, where the value of ε_0 is obtained from initial lens profile by comparison of the base area and the curved-surface area (Fig. A.3c). When the lens is stretched in both planar directions simultaneously, both the base area and the curved surface area increase. When the strain ε approaches to the pre-strain ε_p , the lens becomes completely flat, that is, the base area and the curved surface area should become equal. Although there is a hard thin coating of oxide on PDMS in the buckled structure, we believe that the oxide deforms together with the underlying PDMS film when stretched. In the lens structure reported here, the fact that a very thin lens ($h = 1.53 \mu\text{m}$ and $D = 45.9 \mu\text{m}$) was formed after releasing a pre-strain of 20% suggests that the area of the oxide layer should

not remain fixed during the stretching/release. Thus, the curved surface area A increases until it becomes equal to the base area at pre-strain. This condition is satisfied when the curved surface area A , at strain ε , is approximated by,

$$A = \frac{\pi D^2}{4} \left(1 + \frac{\varepsilon_p - \varepsilon_0}{\varepsilon_p} \varepsilon + \varepsilon_0 \right)^2 \quad (\text{A.6})$$

Based on Eq. A.5 and Eq. A.6, we can calculate the focal length of concave microlens as a function of the applied strain, ε .

In the case of stretching the convex microlens, the lens diameter D increases and lens height h decreases to maintain constant lens volume V_0 (Fig. A.3d). Therefore, the convex lens can never become completely flat, and the focal length f as a function of strain ε is given by the solution of the following equation,

$$f^3 - \left(\frac{\pi D^4 (1 + \varepsilon)^4}{64(n-1)V_0} \right) f^2 - \left(\frac{\pi D^6 (1 + \varepsilon)^6}{768(n-1)^3 V_0} + \frac{3V_0}{4\pi(n-1)^3} \right) = 0 \quad (\text{A.7})$$

Fig. A.3a shows the experimental and theoretical focal length of concave microlens array as a function of applied strain. When the strain ε approaches the pre-strain ε_p (20%), the focal length increases rapidly. An 83% increase of focal length is observed experimentally at 12% applied strain and 158% increase of focal length as the applied strain reaches 17%. In contrast, in the case of convex microlens array, only 42% increase of focal length is observed up to 12% applied strain (Fig. A.3b).

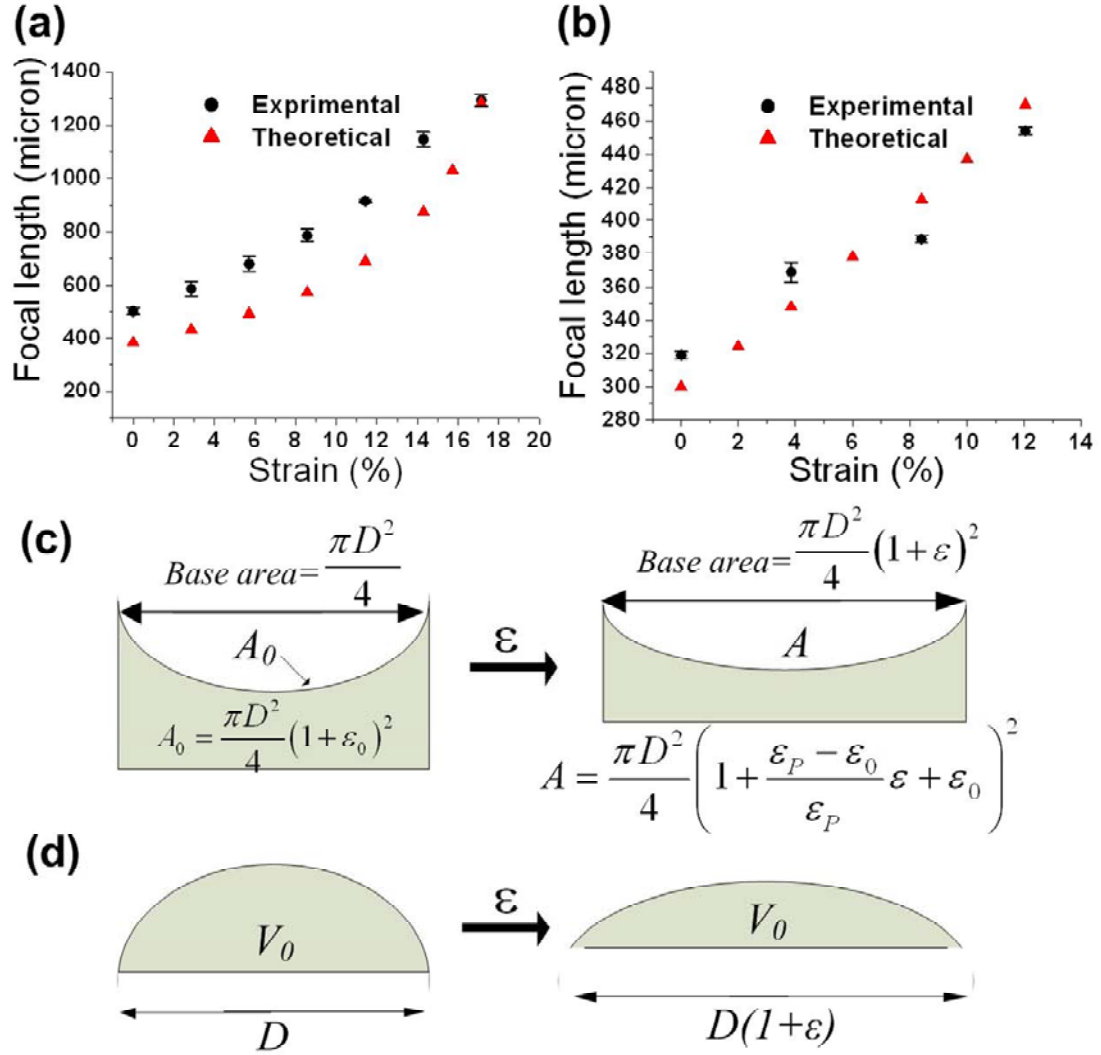


Figure A.3 Focal length variation and corresponding stretching mechanism of the concave (a,c) and convex (b,d) microlens array, respectively.

The significant difference in the tunability of the concave and the convex microlens array may be explained by the fundamental difference in the origin of lens formation. The curved structure of the concave microlenses is formed under the buckling force when the pre-strain ε_p is released after formation of oxide layer. Thus, by design,

the concave microlens should be completely flattened, i.e. the lens volume V decreases to zero when the applied strain becomes equal to the pre-strain, ε_p . This constraint of $V = 0$ at $\varepsilon = \varepsilon_p$ in the concave lens provides large tunability of the focal length by applying mechanical strain. In contrast, the curved structure of the convex microlens is replicated from the concave microlens and there is no buckling involved in lens formation. When a convex microlens is stretched, since PDMS is an elastomer (Poisson's ratio $\nu \approx 0.5$), the lens volume V_0 remains constant such that the lens can never become completely flat. This constraint results in considerably smaller focal length tunability.

To estimate the focal length, we assumed the lenses were spherical with either completely flat lens at pre-strain (concave lens) or constant lens volume (convex lens) constraints. In comparison of the experimental and calculated focal length vs. applied strain, we observed similar trend but systematic difference in the concave microlenses (Fig. A.3a), whereas those agree reasonably well in the convex microlenses (Fig. A.3b). It suggests that the approximation of spherical lens and constraints of flat lens at pre-strain (concave lens) or constant volume (convex lens) is sound. The systematic difference between the experimental and theoretical data in concave lenses may be partially attributed to the difference in refractive indices in the bilayer structure, which is not taken into account in calculation due to the uncertainty in thickness of the oxide layer. In addition, Eq. A.6 for curved surface area as a function of strain may not be accurate enough to approximate the actual change in lens surface area with increase of strain.

A.4 Conclusions

In conclusion, using mechanical strain induced buckling on patterned PDMS bilayers and replica molding, we fabricated concave and convex microlens arrays, respectively. We demonstrated the real-time focal length tunability of both types of microlens array by applying mechanical strain both experimentally and theoretically. Due to the difference in the mechanism of lens formation, the concave and convex microlens array showed fundamentally different strain response behaviors. Large range of focal length tunability was obtained for concave lens array whereas convex lens array had smaller tunability. We believe that the fabrication of single-component, strain-responsive microlens arrays and study of their tunability would offer important insights to design tunable optical microdevices for many optics, MEMS, and sensing application

A.5 References

- (1) Kim, J.; Nayak, S.; Lyon, L. A. *J. Am. Chem. Soc.* **2005**, *127*, 9588.
- (2) Yang, S.; Ullal, C. K.; Thomas, E. L.; Chen, G.; Aizenberg, J. *Appl. Phys. Lett.* **2005**, *86*, 201121.
- (3) Dong, L. A.; Agarwal, A. K.; Beebe, D. J.; Jiang, H. R. *Adv. Mater.* **2007**, *19*, 401.
- (4) Yang, S.; Krupenkin, T. N.; Mach, P.; Chandross, E. A. *Adv. Mater.* **2003**, *15*, 940.
- (5) Chronis, N.; Liu, G. L.; Jeong, K. H.; Lee, L. P. *Opt. Express* **2003**, *11*, 2370.
- (6) Ren, H. W.; Fan, Y. H.; Wu, S. T. *Opt. Lett.* **2004**, *29*, 1608.

- (7) Hong, K. S.; Wang, J.; Sharonov, A.; Chandra, D.; Aizenberg, J.; Yang, S. *J. Micromech. Microeng.* **2006**, *16*, 1660.
- (8) Lin, P.; Yang, S. *Appl. Phys. Lett.* **2007**, *90*, 241903.
- (9) Bowden, N.; Huck, W. T. S.; Paul, K. E.; Whitesides, G. M. *Appl. Phys. Lett.* **1999**, *75*, 2557.
- (10) Chan, E. P.; Crosby, A. J. *Adv. Mater.* **2006**, *18*, 3238.

Appendix B

List of Publications

- (1) Chandra, D.; Taylor, J. A.; Yang, S. "Replica molding of high-aspect-ratio sub-micron hydrogel pillar arrays and their stability in air and solvents," *Soft Matter* **2008**, *4*, 979. [based on Chapter 4]
- (2) Chandra, D.; Yang, S. "Capillary force induced clustering of micropillar arrays: is it caused by isolated capillary bridges or by lateral capillary meniscus interaction force?," *Langmuir* **2009**, accepted. [based on Chapter 5]
- (3) Chandra, D.; Yang, S.; Soshinsky, A.; Gambogi, R. "Biomimetic ultrathin whitening by capillary-force-induced random clustering of hydrogel micropillar arrays," *ACS Appl. Mater. Interf.* **2009**, *1*, doi: 10.1021/am900253z. [based on Chapter 6]
- (4) Chandra, D.; Yang, S. "Dynamics of droplet imbibition on a rough surface," **2009**, in preparation. [based on Chapter 7]
- (5) Chandra, D.; Yang, S.; Lin, P. C. "Strain responsive concave and convex microlens arrays," *Appl. Phys. Lett.* **2007**, *91*, 251912. [based on Appendix A]
- (6) Zhu, X.; Zhang, Y.; Chandra, D.; Cheng, S. H.; Kikkawa, J. M.; Yang, S. "Two-dimensional photonic crystals with anisotropic unit cells imprinted from poly(dimethylsiloxane) membranes under elastic deformation," *Appl. Phys. Lett.* **2008**, *93*, 161911.
- (7) Hong, K. S.; Wang, J.; Sharonov, A.; Chandra, D.; Aizenberg, J.; Yang, S. "Tunable microfluidic optical devices with an integrated microlens array," *J. Micromech. Microeng.* **2006**, *16*, 1660.